ENGINEERING FLUORESCENT NANODIAMONDS

A Dissertation

by

TODD AUSTIN ZAPATA

Submitted to the Office of Graduate and Professional Studies of
Texas A&M University
in partial fulfillment of the requirements for the degree of

DOCTOR OF PHILOSOPHY

Chair of Committee,	Philip Hemmer
Committee Members,	Stephen Wright
	Hong Liang
	Jun Zou
Head of Department,	Miroslav Begovic

December 2016

Major Subject: Electrical Engineering

ABSTRACT

We have developed a technique to grow fluorescent nanodiamonds under high-pressure and high-temperature conditions by using diamondoid seed molecules and decomposing hydrocarbons into reactive carbon species, such as radicals, to grow nanodiamonds onto these seeds. Furthermore, by using specially designed derivatives of diamondoids as seeds, the process should allow the near-deterministic creation of fluorescent color centers inside the grown nanodiamond. In addition, due to the relatively low growth temperatures, we can grow the diamonds slowly so as to produce nanodiamonds of exceptionally high quality. Such a technology impacts fields such as single spin imaging, bio-labeling and quantum computing. In the future, this technology could be used to engineer single quantum systems, opening the door to a new era of sensing technology on scales smaller than ever before.

DEDICATION

This is dedicated to Ruben and Minerva Zapata: Their intellect, wisdom and love will forever guide me. And to my father Vito, the wisest and kindest man I will ever know. He never gave up in teaching me the legacy of our family, and I will always look up to and love him.

ACKNOWLEDGEMENTS

I must first acknowledge Philip Hemmer for his brilliance in first inventing this project and patience in instructing me to become a great scientist.

Secondly I acknowledge the kindness and selflessness of the faculty and staff at the Carnegie Institution of Washington for allowing me to conduct all my HPHT experiments on their campus and with their help. Of all the amazing scientists at Carnegie Viktor Struzhkin has had the greatest impact on my scientific life for inviting me to campus and teaching me the intricacies of the diamond anvil cell. I must also acknowledge: Andrew Steele, Alexander Goncharov, George Cody, Yingwei Fei and Maddury Somayazulu for their support and friendship.

I also acknowledge Fedor Jelezko and the brilliant graduate students and postdoctoral scientists at The Institute for Quantum Optics at The University of Ulm. They have created a world-class laboratory and allowed me to use it for analysis.

Finally I acknowledge my friends whom have helped in every conceivable way: Neil Bennett, Corliss Kin I Sio, Jared Marske, Michelle Scholtes, Marion Garçon, Lucie Sauzéat, Zack Geballe, Nick Holtgrewe, Ileana Perez-Rodriguez, Colin Jackson, Emma Bullock, Hiroyuki Takenaka, Carolyn Quirarte, Marta Lewandoska, Grant Sarvis and Sherry Stafford-Grimes.

NOMENCLATURE

DAC	Diamond Anvil Cell
HPHT	High-Pressure and High-Temperature
NV	Negatively Charged Nitrogen Vacancy
SC	Center Sample Chamber

TABLE OF CONTENTS

LIST OF FIGURES

LIST OF TABLES

CHAPTER I

INTRODUCTION AND LITERATURE REVIEW

Nanodiamonds (ND) with fluorescent color centers have numerous applications such as biological markers for drug delivery [1] and nanoscale sensors of local magnetic fields[2]. For example NDs containing the negatively charged nitrogen-vacancy center (NV) have been proposed as sensors for a variety of magnetic species in cells, like radicals[3], protons and phosphorous nuclei[4], and also as sensors of local electric fields [5] and temperature[6]. However, in order for many of the biological applications to succeed ultra-small NDs (< ~10 nm) having at least one stable fluorescent color center per crystal are needed so that they can easily enter cellular compartments or membranes [7] and that they can be eventually cleared by the kidneys of mammals[8]. Thus far the smallest NDs (~1.6 nm) with stable fluorescent emitters (silicon-vacancies (SiV)) are harvested from meteors. However NVs are not typically seen in nanocrystals under ~7 nm [9] although there have been isolated reports down to 5 nm, [10], but these do not show good ODMR contrast and exhibit “blinking” in the PL spectrum.

In order to fabricate USNDs that are suitable for high-performance sensing applications new fabrication techniques are required. Currently, the two most common techniques for nanodiamond fabrication involve grinding down larger crystals or by growth via mechanical shock like detonation of explosives, laser ablation or ultrasound[11]. USNDs manufactured by such techniques (especially detonation) have a high density of sp2 surface defects that quench color-center fluorescence and reduce magnetic sensitivity in the case of NV sensing[12]. Finally these growth techniques only allow for probabilistic placement of color centers so that high doping concentrations are needed to insure at least one color center per USND which often leads to degraded performance of sensors, for example those based on NVs.

Among the various techniques to grow USND the best so far involve high-pressure high-temperature (HPHT) growth starting from organic precursors. This has shown excellent promise in terms of crystal purity and quality. Beginning with the seminal paper by Wentorf [13] NDs have been grown starting from a variety of organic compounds. Notably, the NDs harvested can be white in color, compared to black or grey for NDs produced by grinding or detonation, suggesting a low concentration of impurities and defects, especially the undesirable sp2 [14] bonded carbon. If these USNDs can be grown by nucleating around a molecule containing the elements needed for specific color centers, then high-quality, deterministic growth might become possible.

For such nucleation to be possible the HPHT growth must be at low enough temperature that the seed molecule does not decompose. Thus far Davydov [15] has shown that HPHT growth of nanometer and micron-sized diamonds, starting from organic precursors like polycyclic aromatic hydrocarbons (PAH), proceeds in three steps. The first is amorphization of the organic compound (~600 ºC), second is carbon polymerization and hydrogen transfer (600-1000 ºC). The third stage from 1000-1200 ºC is associated with the formation of micro-crystalline graphite. The fourth state is the formation of micro-crystalline diamond which occurs above ~ 1280 ºC. It should be noted that the graphite and diamond formation stages are not very sensitive to the initial PAH. Clearly the diamond formation temperature here is too high for any molecular seeding approach.

In addition to micro-sized nanocrystals, Davydov also observed nano-sized carbon phases in the same samples[16]. They noted that the temperature for the USND formation was considerably lower, 1150 ºC, than for the micro-crystalline diamond. Here they proposed that the nano-graphite stage is bypassed and the NDs grow from the carbonization material associated with the decomposition of the initial PAH. However, as long as the PAH is decomposed before USND growth initiates there is still no benefit to the use of a custom seed molecule, and therefore the growth temperature must be further decreased.

Recently Davydov has shown that seeding with fluorocarbon can drop diamond growth temperature to 900 C [1].However this is still well above the decomposition temperature of any known diamond-like organic seed molecules.

This dissertation reports a new method to greatly reduce growth temperature to well below that needed for diamond-like seed stability. Specifically we use a source of carbon that cracks at a very low temperature and dissolve the diamondoid seeds in this hydrocarbon precursor. Upon cracking, the precursor generates reactive carbon species like radicals that begin to bond to the seed molecule to form ND. By “doping” the seed molecule with certain atoms as illustrated in Figure 1(a) it is possible to create color-centers or quantum registers deterministically. Furthermore, by using a stable seed molecule we can grow at a very low temperature where the reactive carbon concentrations are small, see Figure 1(b, bottom row). This should allow slow growth of FND which should result in high crystal quality and few surface defects. In contrast, past HPHT hydrocarbon experiments, illustrated in Figure 1(b, top row), rely on "self-nucleation" which in turn relies on a high concentration of reactive carbon that leads to rapid subsequent growth and can produce lower quality crystals and sometimes agglomeration.

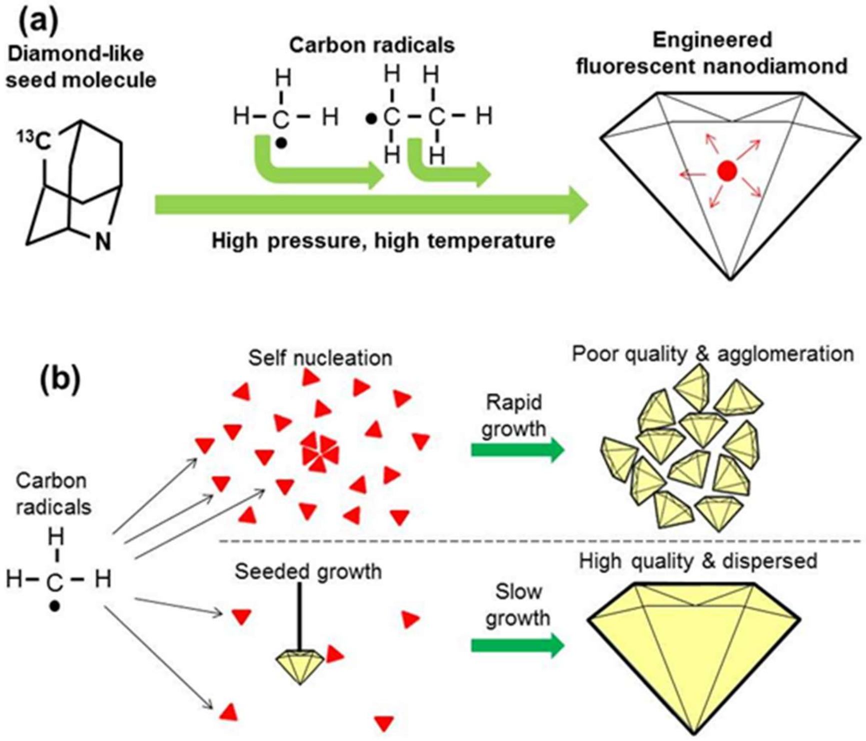

Figure 1 Schematic diagram of the proposed seeding process to create FNDs. (a) The diamondoid derivative is diluted inside a hydrocarbon environment (such as paraffin wax), and placed under HPHT conditions. In this example the seed molecule contains a nitrogen atom as a precursor for a NV center plus a 13C atom at a well-defined distance as needed for a room temperature quantum storage register. (b) (top row) Most prior HPHT growth requires a high concentration of reactive carbon species in order to give self-nucleation. However, this high concentration gives rapid subsequent growth that can lead to poor crystal quality and agglomeration. (bottom row) Using stable diamond-like seed molecules the reactive carbon concentration can be kept low so that the growth is slow and controlled, producing high quality nanodiamonds.

CHAPTER II

THE DIAMOND ANVIL CELL

The main apparatus used to create the high-pressure required for the seeding technique is the diamond anvil cell (DAC), Figure 2a. The main advantage of DACs is the ability to monitor growth in real time. This is to be contrasted with prior work using multi-anvil and belt presses that requires numerous growth runs to be made, where each is quenched after different growth times and temperatures in order to produce a series of snapshots needed to reconstruct growth dynamics. Hence the DAC allows radical new growth concepts to be tested in a fraction of the time. There are several types of DACs and various methods of heating and preparation[17]. The basic components of the DAC consist of the diamond anvils, seats to hold the anvils (Figure 2e), screws to apply the necessary force to generate the high-pressure (Figure 2a), and a “gasket” used to hold the sample and distribute the applied pressure (Figure 2c and d). The high-temperature for the seeding experiments is produced by using either laser heating or resistance heating methods, both methods will be discussed in later sections.

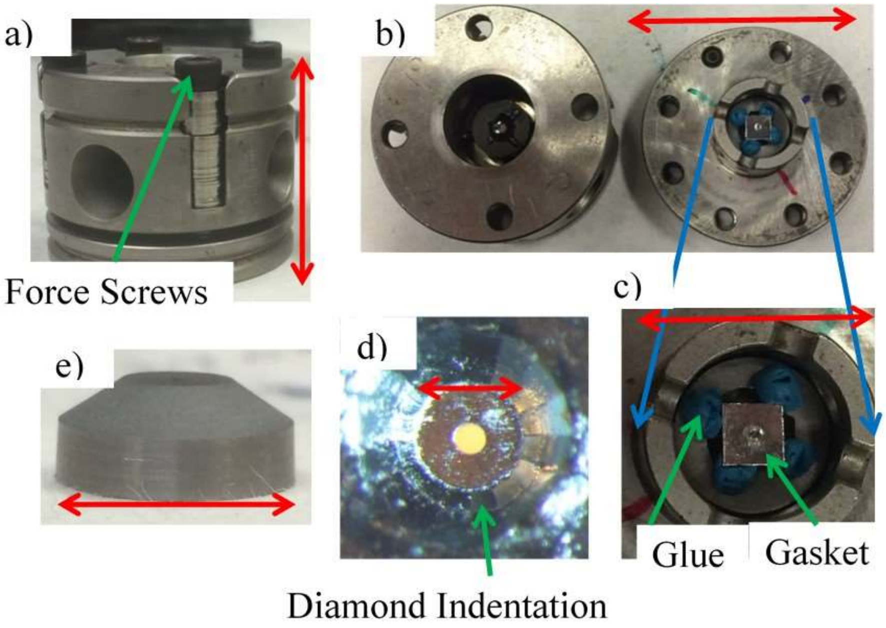

Figure 2 Pictures of the symmetric DAC design used for the laser heated HPHT experiments. a) The closed DAC with screws inserted. The scale is 35 mm. b) The DAC opened with the gasket, glue and seat visible. The scale bar is 47.5 mm. c) Magnification of the gasket placed on the anvil. The scale bar is 18.3 mm. d) Magnification of the gasket hole (the "sample chamber") after pre-indentation, the indentation of the diamond anvils is visible. The scale bar is 300 µm. e) Picture of the Boron Nitride seat used to hold the diamond anvils. The scale bar is 13.3 mm.

The key element of DAC growth is the sample chamber (SC) fabrication. This is done by first pre-indenting the gasket by applying ~ 20 GPa using the DAC, and then laser cutting a hole in the center (~ 100 µm diameter for these experiments).

Every sample chamber uses ruby to monitor the pressure inside during growth[18]. Temperature is measured by using either a Planck fit to the thermal radiation (assuming black body radiation) for the laser heating experiments, or using a thermal couple for resistance and oven heating experiments.

For the HPHT experiments conducted in this dissertation there were two main DAC preparation challenges: The first was how to optimally load the sample into the gasket, and the second is how best to uniformly heat the sample. In what follows the detailed process of pressurization of the sample and gasket is first discussed followed by the temperature profiles encountered for the two basic heating designs, namely laser and resistance heating.

2.1 Pre-indentation of The Gasket

An important step in DAC experimental preparation is the pre-indentation of the gasket and subsequent creation of the SC. The typical procedure for the pre-indentation is to pressurize the gasket using the anvils. The indentation pressure is different for different gasket materials, i.e. for steel the pre-indentation pressure is about 10 GPa and for Re (which was primarily used for the seeding experiments) the pre-indentation pressure is 20 GPa. The indentation pressure is also determined by the thickness, t, desired for the SC and the desired final pressure for the experiment. This section will review the main physics associated with the pre-indentation and pressurization of the gasket and SC.

The basic theory for the physical mechanisms associated with the pre-indentation and pressurization process are given in[19]. In what follows the gasket is assumed to be under a uniaxial normal load. Figure 3 illustrates the basic stress components during the gasket pre-indentation.

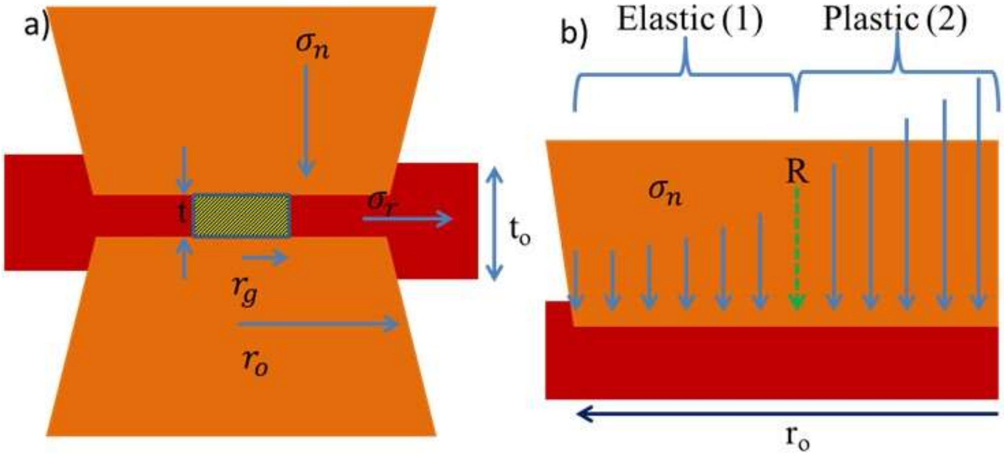

Figure 3 a) Cross-sectional illustration of the pre-indentation of the gasket (red block) by applying pressure from the diamond anvils (orange rhombohedrum). The directions of the normal stress, σ_n, and the radial stress, σ_r, are depicted, as well as the initial and final gasket thickness, t_o and t respectively, and the radius of the SC, r_g, and the location at which the edge of the anvils make contact with the gasket, r_o. b) Cross-sectional illustration of the normal stress distribution as a function of position (blue arrows) inside the DAC during pre-indentation before the SC is created. In region (1) the gasket material is flowing elastically (because the frictional force between the gasket material and the anvils is not greater than the yielding stress, k). Here the normal stress has an exponential profile, starting from the edge and rising toward the middle until a certain radius R at which the gasket material flow becomes plastic. In plastic region (2) the deformation of the gasket is plastic and the stress vs position profile is linear. At the edge of the anvil, r_o, the normal stress is (n+1) k (see text). The transition region between elastic and plastic flow is presented by the green dotted arrow labeled R.

The four main components of stress acting on the gasket are the normal stress (σ_n), radial stress (σ_r), circumferential stress (σ_c), and the hydrostatic component of the stress (σ_h). The relationships between the components under ideal conditions are

$$\sigma_r = \sigma_c = \sigma_h \tag{1}$$

$$\sigma_n = \sigma_h + k, \tag{2}$$

where k is the stress for yielding of the gasket under uniaxial load (i.e. the stress when the material begins to deform plastically). The equation governing the radial component of the stress is

$$\frac{\partial \sigma_r}{\partial r} = \frac{-2f}{t}. \tag{3}$$

Where f is the frictional force per unit area, and t is the gasket thickness. For a coefficient of friction between the gasket material and the anvils, μ, the frictional stress is either given by$f = \mu\sigma_n$, for elastic deformation of the gasket (ie when $\mu\sigma_n < k$), or $f = \frac{k}{\sqrt{3}}$ in the plastic deformation regime (ie when $\mu\sigma_n > k$). In the elastic regime the frictional force causes the gasket to extrude, or flow, around the anvils (see picture in Figure 2d). In the plastic deformation regime there is a “no slip” boundary condition between the gasket and the anvils. At the contact point between the edge of the anvil and gasket, r_o, the typical boundary condition is $\sigma_r(r_o) = (n+1)k$, which is dictated from “Bridgman’s principle of Massive Support”[20], and n is an integer, $n \geq 0$.

The normal force as a function of radial position on the gasket is therefore

$$\sigma_n^{(1)}(r) = (n+1)k e^{\frac{2\mu}{t}(r_o - r)}; \; r \in (r_o, R) \tag{4}$$

$$\sigma_n^{(2)}(r) = \frac{k}{\mu\sqrt{3}} + \frac{2k}{t\sqrt{3}}(R - r); \; r < R, \tag{5}$$

where R is the location at which the deformation changes from elastic, the exponential profile, to plastic, the linear profile (Figure 3b)

$$R = r_o - \frac{t}{2\mu} \ln\left(\frac{1}{(n+1)\mu\sqrt{3}}\right), \tag{6}$$

and is determined by the condition $\sigma_n^{(1)}(R) = \sigma_n^{(2)}(R)$. Note also that a second boundary condition is placed on the normal component in the second region, $\mu\sigma_n^{(2)}(R) = \frac{k}{\sqrt{3}}$. From the definition of R, if the coefficient of friction $\mu \geq \frac{1}{(n+1)\sqrt{3}}$ then the gasket deformation is essentially plastic and the normal stress is given by

$$\sigma_n^{(2)}(r) = (n+1)k + \frac{2k}{t\sqrt{3}}(r_o - r). \tag{7}$$

By setting r=0 in equation (7) and solving for t, the pre-indentation thickness may be approximated from the measured hydrostatic pressure at the center of the gasket, $P = \sigma_n^{(2)}(0) - k$, Figure 4.

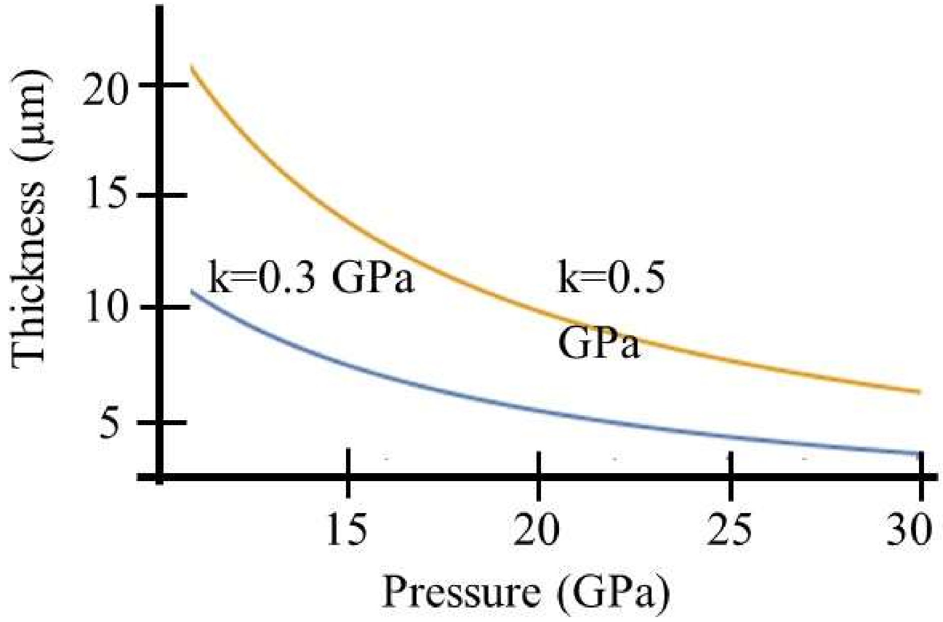

Figure 4 Pre-indentation thickness as a function of the measured hydrostatic pressure at the center of the gasket for different values of the yield strength k. The plot is given by equation (7) and setting r=0, n=1 and r_o=150 µm. Re, the typical gasket material used in the experiments, has a typical yield strength of 0.3 GPa.

Integrating this solution for $\sigma_n^{(2)}$ over a circular region with radius r_o yields the force applied to the gasket during pre-indentation

$$F(r) = \int_0^{r_o} 2\pi r\, \sigma_n^{(2)}(r) dr \tag{8}$$

$$= \pi r_o^2 (n+1)k + \frac{2\pi k}{t3\sqrt{3}} r_o^3. \tag{9}$$

Substituting equation (7) into $P = \sigma_n^{(2)}(0) - k$, the hydrostatic pressure at the center of the gasket becomes $P = \sigma_n^{(2)}(0) - k = nk + \frac{2kr_o}{t\sqrt{3}}$. Hence substituting equation (9) the relationship between the hydrostatic pressure and the force may be modeled as

$$P = \frac{3F}{A} - k(2n + 3), \quad (10)$$

where $A = \pi r_o^2$. The main point of this equation is that an initial force is required to reach a deformation condition, $F_o = \frac{kA}{3}(2n + 3)$, before the hydrostatic pressure begins to increase because a negative hydrostatic pressure is unphysical. This is always seen with the pre-indentation of the Re gasket. An initial applied load always increases the pressure until around 5 GPa during which the deformation is elastic and the coefficient of friction is not high enough to cause plastic deformation. When the force is high enough equation (10) begins to apply but P starts out being negative meaning that plastic deformation[1] occurs and a load increase does not correspond to a pressure increase (or decrease). Once the pressure P becomes positive a further increase in force once again causes an increase in pressure approximately given by equation (10).

After the gasket has been pre-indented a hole is cut either by laser (pulsed 1.06 μm) for SC diameters less than 100μm, or using an electrode drilling machine (EDM) if the required SC diameter is larger 100 μm. The hole is then filled with the sample, typically using the pressure of the anvils to "pack" the sample inside.

The equations governing the pressurization of the SC are similar to the pre-indentation equations. Figure 5 illustrates the basic components of the SC during pressurization.

---

[1] Note that the yield strength for Re is 290 MPa, hence for n~10 (which is a typical value) the pressure required may be estimated as $P_o \approx 290MPa \times \frac{23}{3} = 2.2\ GPa$, which is close to the observed onset of plastic deformation for Re around 5 GPa.

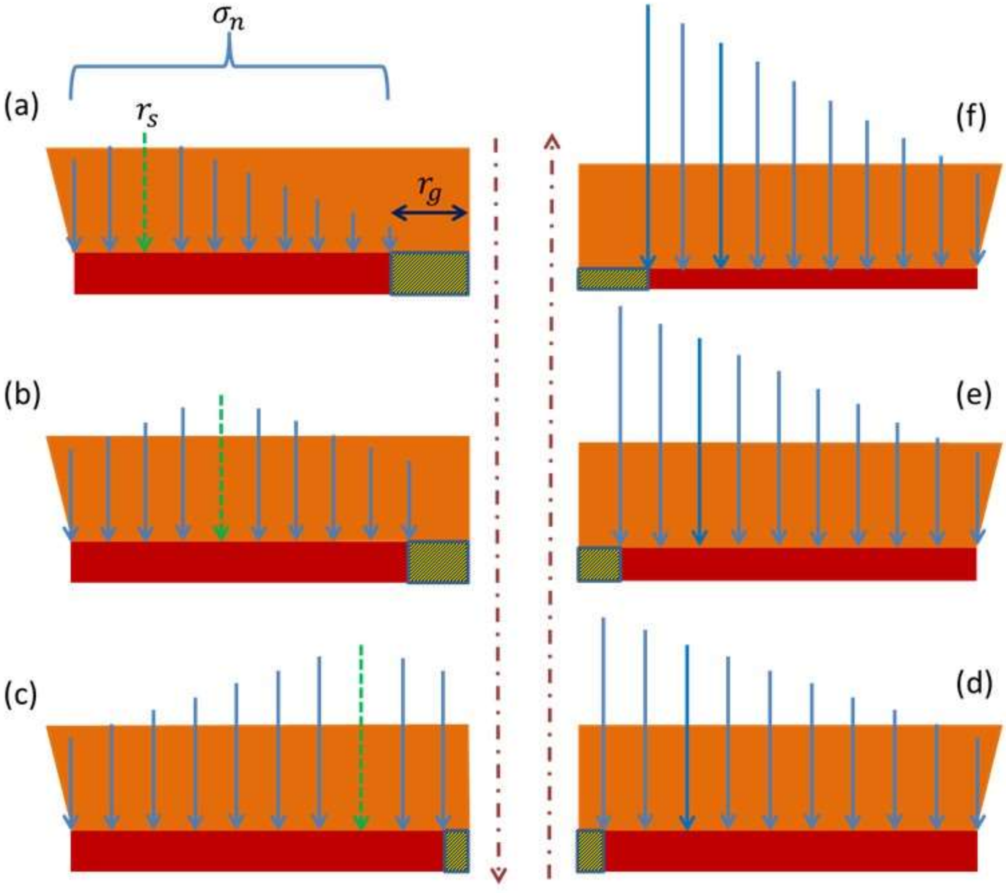

Figure 5 Cross-sectional illustration of the gasket deformation for a sample chamber with radius r_g and gasket thickness t. For figures (a)-(c) the pressure inside the chamber is increasing due to a contraction of the inner chamber radius, r_g. The radius corresponding to the region where the plastic deformation changes from inward to outward extrusion (flow of gasket material), r_s, is labeled by the green dashed arrow. The blue arrows depict the magnitude and direction of the normal stress distribution along the radial direction of the gasket. As the normal stress increases r_s will decrease until it is equal to r_g. For figures (d)-(f) a further increase in the normal stress corresponds to an increase in the sample chamber (gasket inner) radius and a decrease in the gasket thickness. For all regions the boundary condition at the edge of the anvil is given by $\boldsymbol{\sigma_n(r_o) = k(n+1)}$ and the hydrostatic pressure inside the growth chamber is less than the normal stress by k.

For a SC radius of initial r_g the new boundary condition to impose on the stress is that the radial stress must be continuous across the SC/gasket boundary, $\sigma_r^{(2)}(r_g) =$

$\sigma_r^{(3)}(r_g)$, and the assumption is made that the shear strength of the material inside the SC is zero (i.e. f=0),

$$\sigma_r^{(3)} = nk + \frac{2k}{t\sqrt{3}}(r_o - r_g) = \sigma_n^{(3)}. \tag{11}$$

However equation (11) is for an incompressible sample, for compressible samples the hole will contract or expand upon loading.

The method of pressurization of a (compressible) sample depends on the thickness of the gasket and the compressibility of the material. The boundary conditions imposed on the stress is again the "Massive Support" (where normal force and (n+1)k are equal) at the edge of the anvil, and also that the hydrostatic pressure, P, is continuous across the SC boundary.

The solution for this problem requires creating two regions inside the gasket with the boundary between the two regions at the location r_s. The first region, "a", (gasket material flowing out or left of r_g in Figure 5a-c) has the massive support boundary condition

$$\frac{\partial \sigma_r^{(a)}}{\partial r} = \frac{-2k}{t\sqrt{3}}; \;\; [r \in (r_s, r_o)], \tag{12}$$

and the second region, "b", (gasket material flowing in out or right of r_g in Figure 5 a-c) has the continuity condition associated with the P across the SC/gasket boundary

$$\frac{\partial \sigma_r^{(b)}}{\partial r} = \frac{2k}{t\sqrt{3}}; \;\; \left[r \in \left(r_g, r_s\right)\right]. \tag{13}$$

Note that the slopes have opposing signs. Requiring r_s to satisfy $\sigma_r^{(a)}(r_s) = \sigma_r^{(b)}(r_s)$, yields the solutions

$$\sigma_r^{(a)} = nk + \frac{2k}{t\sqrt{3}}(r_o - r) \tag{14}$$

$$\sigma_r^{(b)} = P + \frac{2k}{t\sqrt{3}}(r - r_s) \tag{15}$$

$$r_s = \frac{r_o + r_g}{2} - \frac{(P - nk)\sqrt{3}t}{k} \tag{16}$$

The important difference between regions a and b is that the gradient of σ_r is negative and positive, respectively.

The equations reveal that the pressure inside the SC may increase by either by decreasing the thickness of the gasket or decreasing the radius of the SC . For a gasket which has been pre-indented to a sufficient pressure such that the advancement of the anvils does not change the thickness, the only mechanism for the pressurization of the SC is for the radius to decrease, as long as the sample is compressible. In fact, the extrusion of the gasket depends on the thickness and pressure, and there are actually two regions of extrusion for the gasket, as discussed above. The first is where the gasket extrudes inward closing the SC hole, $r \in (r_g, r_s)$, and a region where the gasket extrudes outward, $r \in (r_s, r_o)$. The boundary for the change in extrusion direction, r_s, decreases towards r_g as the applied load is increased, and once $r_s=r_g$ the gasket hole begins to expand. In this load regime the pressure inside the SC is increased by a decrease in the gasket thickness, however increasing the load may have no effect on the pressure (or even decrease the pressure) due to the expansion of the gasket hole[2].

Finally it should be noted that if the anvils are not perfectly aligned then the thickness of the gasket will not be uniform, consequently resulting in an asymmetrical expansion of the gasket hole, Figure 6. Such expansion may cause the anvils to become damaged.

---

[2] In the experiments conducted with a 100 μm chamber hole and 20 GPa per-indentation pressure of a Re gasket with Adamantane as the sample, the hole expansion typically occurs around 30 GPa. However, with better alignment of the anvils the expansion has been delayed to up to 40 GPa.

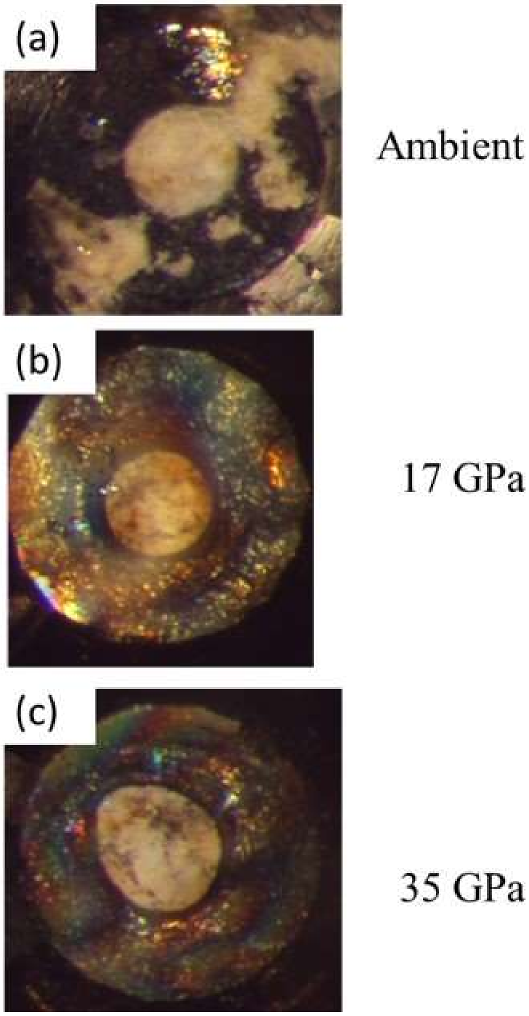

Figure 6 Pictures of the gasket with Adamantane inside at various pressures to show the effect of the SC (preindented to 20 GPa) under high pressure when the diamond anvils are slightly misaligned. In (a) and (b) the SC remains symmetrical and the radius decreases slightly. But as the pressure is increased beyond 30 GPa the hole begins to oblong, (c), due to a small misalignment of the diamond anvils causing a pressure gradient inside the growth chamber.

2.2 DAC Heating Techniques

High-temperatures inside the DAC are created by either laser or resistance heating. Each technique requires a different DAC architecture and temperature measurement techniques. As will be described below the main differences between the two heating types is the peak temperature and temperature gradients inside the SC. In both heating techniques the diamond anvils play an important role in that they act as infinite heat sinks due to the high thermal conductivity of diamond, $\approx$ 500 W/m/K, and their larger size compared to the SC.

For the laser heating experiments a 1.06 μm continuous wave (CW) laser is used to heat the sample inside the SC. However, for samples which will not absorb the 1.06 μm (such as Adamantane) a Ti washer is placed inside the SC to act as a coupler to absorb the laser Figure 10. The temperature is estimated by assuming Black Body thermal radiation from the "hot spot" (i.e. the location where the laser is focused) inside the SC. The temperatures produced within the hot spot can reach up to ~6000K, with temperature gradients being as large as 10^9 K/m[21]. The typical maximum power of the CW laser is ~ 20W. Both numerical and analytic solutions have been calculated to model the temperature distribution inside the laser heated DAC. The solutions predict that the radial temperature distribution is controlled by the laser beam waist (both the TEM_{00} and the TEM^*_{01} modes were considered in[22]), and the axial temperature distribution is dictated by the height of the SC (bounded by the diamond anvils).

The main assumptions made in modeling the laser heated DAC with sample chamber of thickness l and radius R are that there is no laser absorption except within the SC, the laser power is uniformly absorbed by the sample and the depth of focus of the heating laser is approximately equal to the depth of the sample chamber $l \approx 10\ \mu m$. Although the uniform absorption assumption this is not true for adamantane with a Ti absorber (coupler) the equations will give an order of magnitude estimate. Under these assumptions the heat source in W m^{-3} is

$$A(r) = \frac{(1 - e^{-\alpha l})p(r)}{l}, z \in \left(-\frac{l}{2}, \frac{l}{2}\right), \tag{17}$$

where l is the SC height, and α is the absorption coefficient of the SC material. The power flux for heating laser, $p(r)$, was calculated for the TEM$_{00}$ mode to have the profile

$$p(r) = p_o e^{-\frac{r^2}{R^2}}, \tag{18}$$

where $2R$ is the beam waist and p_o is the peak power flux.

Using these equations and assumptions, along with the boundary conditions that the temperature and the normal fluxes of the temperatures be continuous across the SC/diamond anvil and the SC/gasket boundary the temperature profiles have been modeled both analytically and numerically. One of the main results from the simulations is that the temperature profile inside the laser heated DAC may be approximated by

$$T(r, z) \sim T_o e^{-\frac{r^2}{\rho^2}} e^{-\frac{z^2}{\xi^2}}, \tag{19}$$

where $\xi \sim \frac{l}{2}$ and $\rho \sim R$. In fact when the authors in [21] changed the SC height by a factor of 4 the value of ρ remained essentially the same whereas ξ changed by a factor of 4, agreeing with the statements that the axial temperature distribution inside the DAC is dictated by the vicinity of the diamond anvils, and the radial distribution is only dependent on the laser beam geometry.

Since the temperature of the SC is essentially limited by the temperature of the diamond anvils the majority of the SC is at ambient temperatures for laser heating. And there is only a small region which is able to overcome the extreme heat loss inside the DAC due to the diamond anvils. This small region creates high temperature gradients making accurate temperature measurements difficult. If it is required to have relatively small temperature gradients inside the SC then it is the diamond anvils which must be heated to a uniform temperature[23]. To satisfy these requirements resistance heating architectures are employed.

There are two types of resistance heating furnaces used in the experiments. The first type (i.e. the "heater" method) uses an adhesive to combine the gasket to a home-built heater Figure 11a and b). The second type (i.e. the "oven" method) immerses the entire DAC inside an oven (Figure 12a). For both types of heating methods the main mode of heat transportation is convection.

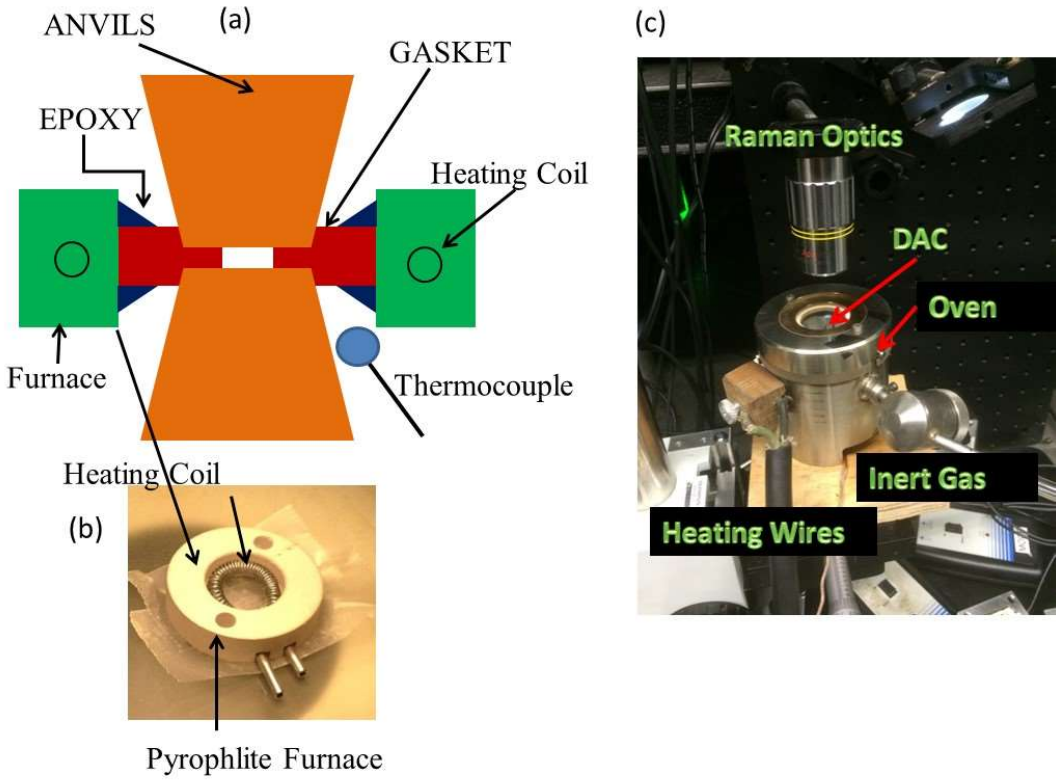

Figure 7 Pictures from the furnace heating experiment. (a) Cross-sectional drawing of the DAC for furnace heating. (b) Pictures of the furnace heater (furnace) before application of a high-temperature epoxy to hold the Molybdenum heating coils in place. (c) Picture of the oven heating experiment. Throughout the heating process a 98 % Ar and 2% H_2 gas mixture flows through the oven to protect the diamond anvils from oxidizing. The window at the top of the oven allows *in situ* Raman spectroscopy during HPHT.

The advantages of the heater method are that it is readily inexpensive and easy to make inside the laboratory. However the heaters typically do not last for more than two or three experiments due to the oxidation and melting of the heating coils (Figure 11a), and the temperature of the SC is typically less than the temperature of the heating coils due to conduction by the diamond anvils, yielding inaccurate SC temperature measurements. Whereas the oven heating method is more expensive, the temperatures inside the DAC are larger than the heater method due to the higher temperature of the diamond anvils. The heating wires inside the oven are still under the risk of oxidation and melting, and if they break then it is a much more complicated task to re-wire the entire oven than to create a new miniature heater.

CHAPTER III

ADAMANTANE

Due to its simple molecular structure and natural abundance adamantane has been studied more than all other diamondoids. Furthermore it is the prototypical seed used in our ND growth experiments because of its near perfect match to the cubic diamond unit cell Figure 8(c), with all other seeds used being adamantane derivatives with dopants added such as the Nitroxyl group for AZADO. Although when used in the seeding method adamantane is diluted into a matrix of hydrocarbons, and hence is no longer subjected to crystalline effects, an understanding of crystalline adamantane is still imperative. This is because the decomposition properties of adamantane can be better studied in a crystalline matrix where it is not too dilute to see the Raman bands. Hence this section will review the basic physical and thermodynamic properties of adamantane molecular crystals at ambient and HPHT conditions.

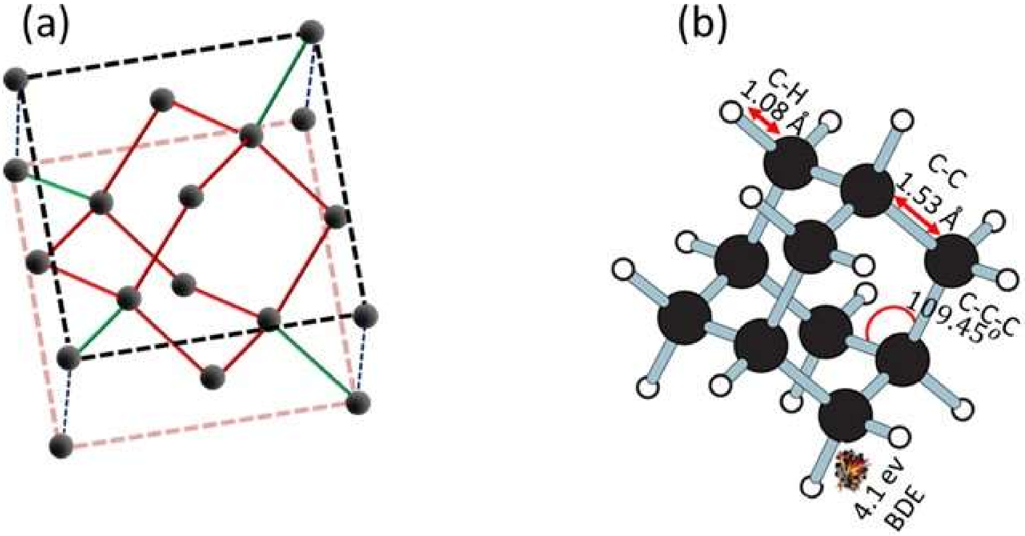

Figure 8 (a) Illustration of the diamondoid adamantane embedded into the cubic diamond unit cell. (b) Illustration of the adamantane molecule at ambient conditions. Black circles are C and white circles are H atoms.

Adamantane Figure 8(b), $C_{10}H_{16}$, has been studied extensively over the last 50 years. The experimental and numerical measurements of the molecule include: High-pressure Raman scattering and AXRD[24],[25] and[26], high-pressure numerical simulations[27], phase diagrams and solubility measurements [28] and [29] and adiabatic calorimetry to measure the heat of formation and other thermodynamic quantities[30].

The carbon skeleton at ambient conditions is composed of three zero-strain fused six-membered carbon rings in the “arm chair” configuration. At ambient conditions the C-C distance is 1.53 Å, compared to 1.52 Å for diamond, and the C-C-C bond angle is 109.45°, compare to 109.5° for diamond. The molecule contains 4 methine (CH) bonds and 6 methylene (CH_2) bonds, and the 4.1 ev CH bond dissociation energies are similar to methane. The ambient molecular point group symmetry is T_d.

At ambient conditions (α-phase) adamantane is a disordered plastic crystal with cubic space group symmetry Fm3m (Z=4), a=0.945 Å, and the distance between H atoms (H…H) on neighboring molecules is 2.23 Å. Below 208 K at ambient pressure or above 0.48 GPa at ambient temperatures adamantane transforms into an ordered tetragonal phase (β-phase) with space group $P42_1c$ (Z=2). The transition to the ordered phase is associated with a volume contraction of ~ 3.5 %, and the H…H distance increases to 2.37 Å, twice the Van der Waals radius for molecular hydrogen. The ordered-phase space group, $P42_1c$, implies that the two adamantane molecules per unit cell have a relative angle of rotation between them. At 0.7 GPa this angle has been measured to be 8.5°, which increases to 10.5° at 12.5 GPa[25]. The orientational change is due to the adamantane relieving the H…H repulsion. This rotation starts at around 9 GPa where the H…H distance begins to saturate to 1.87 Å (which is close to the estimated minimum value of 1.9 Å).

Around 12.5 GPa the molecules begin to deform. The c/a ratio for the tetragonal cell begins to decrease rapidly and AXRD data begins to show new peaks associated with a monoclinic (γ-phase) cell (Z=1). In all high-pressure experiments studied (up to ~45 GPa) the crystal transforms back to the ambient phase upon release of pressure, implying the crystal does not undergo polymerization or decomposition in these high-pressure ambient-temperature regions.

The main cause for high-pressure phase transitions, molecular distortion and changes in position is the repulsion between H atoms on neighboring adamantane molecules [31] and[25]. As stated above, the empirical limiting value on the H…H distance, 1.9 Å[32], should be compared to the H_2 bond length of 0.74 Å and Van der Waals radius of 1.1 Å. Steric hindrance keeps the molecules from approaching this distance[25], and dehydrogenation and/or amorphization of the crystal may be consequences if the molecules approach or pass these distances [33] and[31].

Since adamantane is an organic crystal the main method of attraction between molecules is small Van der Waals forces (as compared to the strong covalent bonds of diamond and Si crystals). The most commonly used model of the attractive and repulsive intermolecular forces between different atoms for adamantane within the crystal lattice is given by the Buckingham potential [34]

$$U(r) = \frac{A}{r^6} + Be^{-\frac{r}{\rho}}. \tag{20}$$

Where the constants A and B represent the attractive and repulsive terms of the interaction, respectively, and are determined for the different atomistic interactions, e.g. for the Hydrogen-Carbon, Hydrogen-Hydrogen and the Carbon-Carbon interactions between atoms on different molecules. The attractive portion corresponds to dipole-dipole interactions, and the exponential repulsive contribution is an approximation to non-bonded repulsions[35].The AXRD experiments of [25] at high-pressures have led to a Vinet equation of state (EOS). The standard Enthalpy of transition from the ordered phase to the disordered phase has been experimentally measured to be 3.276 kJ/mol, and the standard heat of formation of the molecular crystal has been measured as -188 kJ/mol[36]. Other standard thermodynamic quantities have also been measured[30]. Throughout the remainder of this dissertation, the phases of adamantane will be referenced as in Table 1.

Table 1 Space group and pressure ranges for adamantane at ambient temperatures

Phase	Z	Label	Pressure Range (GPa)
Cubic (Fm3m)	4	α	0-0.7
Tetragonal ($P42_1c$)	2	β	0.7-20 (24)
Monoclinic	1	Γ	>24

High-pressure Raman scattering studies on adamantane up to 26 GPa have been carried out in[24]. The study found linear relationships between pressure and the red-shifting in various Raman modes. Only a few of the allowed 72[3] internal modes at ambient conditions are experimentally measured, a property which is common for Van der Waals (i.e. plastic) crystals, and is typically a consequence of anisotropy in the crystal field[24]. This behavior is also observed in the tetragonal phase, where group theory predicts 90 active internal modes. Basically, primarily the stretch modes survive.

To study adamantane stability/decomposition we choose to monitor the Carbon-Carbon symmetric stretch Raman mode (CC) and the 4 dominant Carbon-Hydrogen

---

[3] The internal modes of adamantine transform as $\Gamma_{int}=5A_1+A_2+6E+7F_1+11F_2$. The A_1, E and F_2 modes are Raman active.

(CH) symmetric stretch modes. As stated above, these peaks are choosen because other types of motion, i.e. “rock” and “scissor” motions, are difficult to measure in the higher pressure regimes. Also, changes in the CC symmetric mode relay information about the deformation of the C skeleton, and the CH symmetric modes gives insight to the onset of intermolecular interaction and dehydrogenation.

Experimentally observed and theoretically calculated CH stretch Raman modes and the associated group assignments are given in [37] and [38] for the α-phase, as well as the experimentally observed CH modes in the γ-phase at 30 GPa. As pressure is increased molecular distortion and rotation drastically change the active Raman modes, making it difficult to determine the CH group to which the observed modes in the γ and β-phases belong.

Table 2 Theoretical and experimentally observed CH Raman modes for adamantane at ambient conditions in the α-phase (rows 1 and 2) and experimentally observed in the γ-phase (third row). The exact assignment of the Raman modes in the high-pressure phases of adamantine are not known.

Phase	Mode (Symmetry)	CH Group[a]	Frequency (cm^{-1})[b]
α (Theo.)	ν_1 (A_1)	CH_2	2951
	ν_2 (A_1)	CH	2913
	ν_7(E)	CH_2	2913
	ν_{20} (F_2)	CH_2	2951
	ν_{21} (F_2)	CH	2936
	ν_{22} (F_2)	CH_2	2913
α (Exp.)	ν_2(A_1)	CH	2913
	ν_7(E)	CH_2	2893
	ν_{22}(F_2)	CH_2	2845
	ν_1+ ν_{20} (A_1+F_2)	CH_2	2943
γ (Exp.)			3063
			3116
			3200
			3263

(a) Modes with F and E symmetry are purely CH_2, whereas A_1 has both CH and CH_2 components. The group listed in the table is for the largest contribution from Potential Energy Distribution calculations from[38].

(b) The calculated frequencies depend on the computational program, the values given here are from [37] for the Hatree-Fock level of theory using the standard 6-13 G* basis set.

Figure 9 depicts the measured Raman spectra from the CC and CH regions for adamantane at different pressures. In the α-phase, Figure 9a and the second column in Table 2, there are typically 4 measured Raman peaks associated with CH stretching, three are associated with the Methylene groups and one with the Methine group. The strongest mode (i.e. the highest intensity) in the α-phase is measured to be the C-C symmetric stretch mode with A_1 symmetry and a position at 759 rel. cm^{-1}.

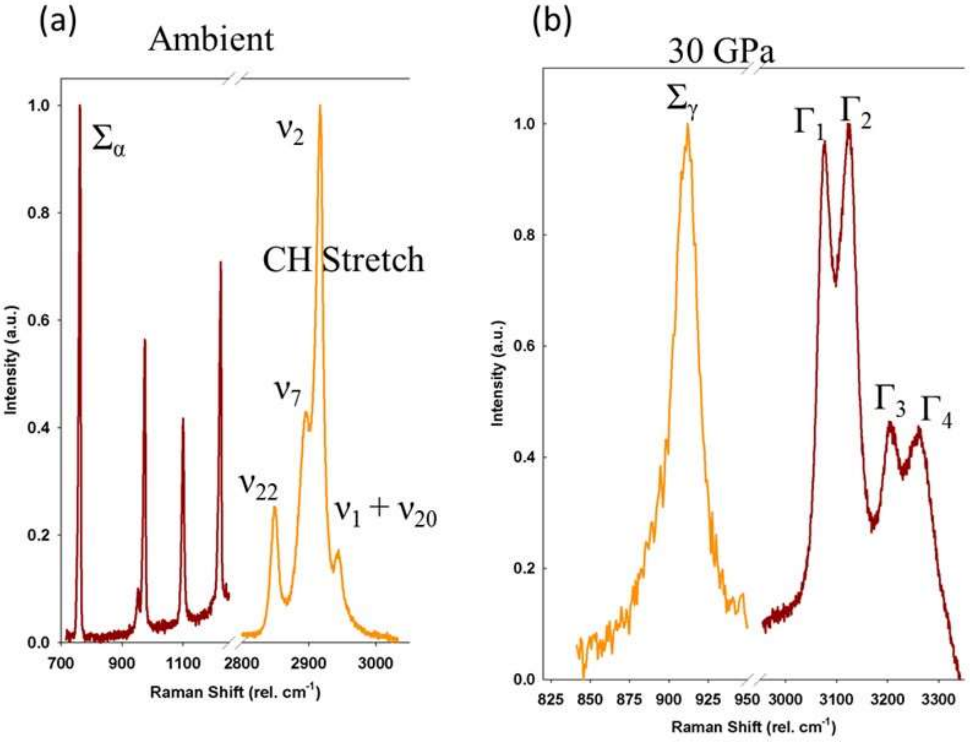

Figure 9 Raman spectra of adamantane in different phases at different pressures. (a) The ambient condition Raman spectra of adamantane in the CC and CH regions. The CC stretch mode, Σ_α, is labeled as is the four CH stretch modes as given in Error! Reference source not found.. **(b) High-pressure ambient-temperature Raman spectra of adamantane in the in the γ-phase at 30 GPa. The CC mode, Σ_γ, and the 4 CH stretching modes, Γ, are labeled.**

CHAPTER IV

EXPERIMENTAL PROCEEDURES

The diamondoids used for the experiments were adamantane (Alfa-Asear, 99.99% grade) or AZADO (Sigma-Aldrich, 96% grade). And the pressure was monitored using the ruby fluorescence method. The placement of all samples into the SC as well as the ruby was conducted using a W needle with a 2µm tip (American Probe Technologies, Inc.). The extraction of the samples after HPHT was carried out using W needles onto quartz cover glass, a Si wafer or TEM grids for further analysis. The following sections give information regarding the exact experimental preparation techniques for the three main DAC architectures: Laser heating, furnace heating and oven heating.

4.1 Laser Heating

Figure 10 depicts an illustration of the laser heating experiment as well as pictures of the Ti coupler. As already mentioned the coupler was necessary because the Adamantane and other hydrocarbon material inside the SC is non-absorbing of the heating laser light. The Ti coupler is a washer with inner diameter of ~30 µm, outer diameter of ~50 µm and a thickness of 6 µm. A laser lathe using a 1.06 µm pulsed laser was used to cut the washers from Ti foil (Alfa Aesar, 99.6%).

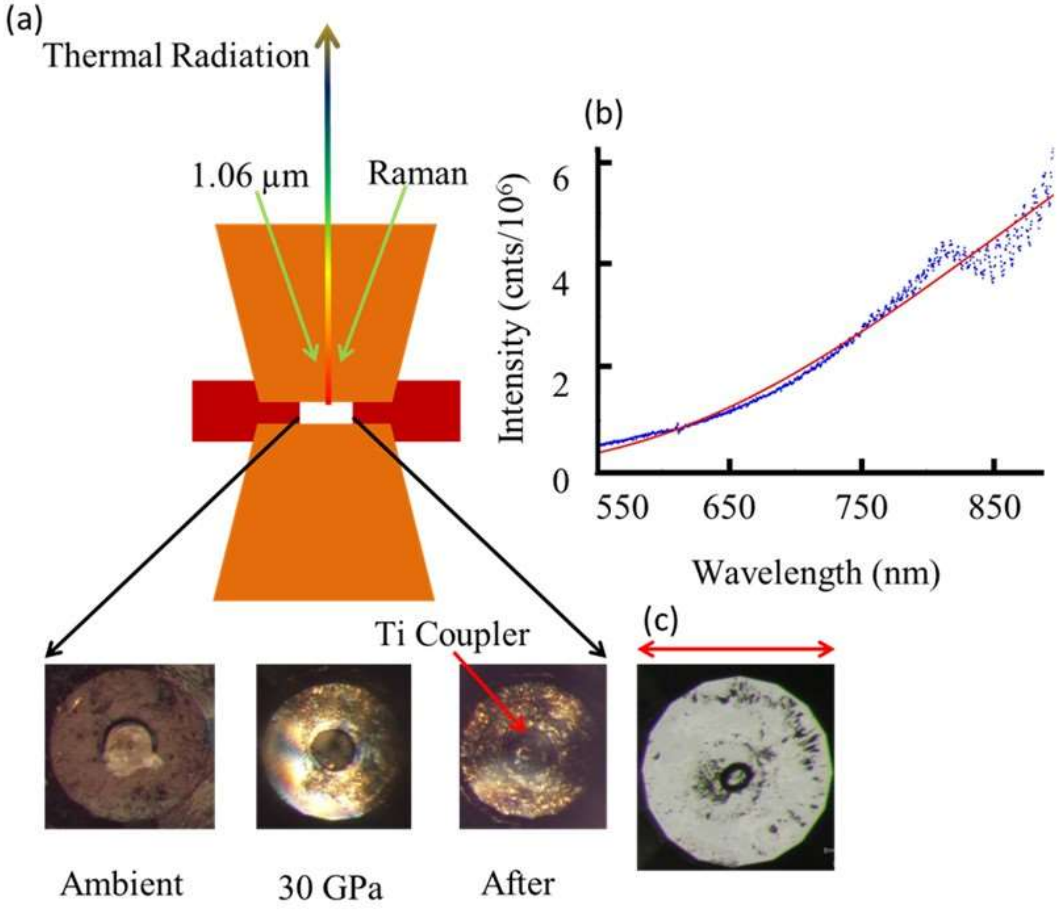

Figure 10. Laser heating illustration and pictures. (a) Illustration of the DAC for laser heating. The 1.06 μm CW laser and the Raman excitation laser both enter the same window, and the thermal radiation from the SC exits the same window and is accumulated and fit to a BB radiation curve, (b). The pictures at the bottom depict the evolution of the SC at ambient conditions, at 30 GPa before HT, and after the laser heating HPHT. (c) Picture of the Ti coupler on one of the diamond anvils, the scale bar is 300 μm.

The main risk with the laser heating method is the diamonds can become damaged or oxidized from the high temperatures of the metal coupler. To circumvent this problem a thin layer of adamantane was coated onto the side of the coupler washer closest to the anvil. Another problem is the excess H_2 which is a by-product from hydrocarbon dehydrogenation (part of cracking). The H_2 will move into the diamond anvils and possibly damage them.

The temperature was monitored by recording the thermal radiation from the SC and fitting the spectrum to black body radiation, Figure 10c. Temperatures were able to be measured between 500-1800 ^{o}C. The seats for the laser heating experiment are Boron Nitride, and the gasket material is Re.

4.2 Resistance Heating

The home-built resistance heaters used for experimentation are presented in Figure 11 and Figure 12c. The heater furnace is made of Pyrophyllite (Aluminum Silicate Hydroxide, $Al_2Si_4O_{10}(OH)_2$), and the heating coils are made of a Molybdenum alloy because this material has a high melting and oxidation temperature. Alumina (Aluminum Oxide, Al_2O_3) adhesive (thermal conductivity ~ 30 W/m/K) is used to hold the gasket inside the heater, Figure 11e. The seats which hold the anvils are Zirconium toughened Aluminum. The temperature is controlled by passing current through the coils using a high voltage-controlled power supply, Figure 11c gives a plot of the temperature profile versus time for a given applied voltage. As can be seen the temperature inside the SC increases exponentially with a time constant when a current step is applied to the heating coils, the profile was measured by placing a thermocouple at the center of the gasket of an unloaded DAC. The heating time rate is in general on the order of .02-.04 s^{-1}. During growth experiments the temperature inside the SC was monitored using a thermocouple glued to one of the diamond anvils, Figure 11f. There is a question of temperature uniformity and accuracy in the SC due to the diamond anvils being cold. To estimate the error we conducted two similar experiments using the furnace and an oven heating procedure (diamond anvils also hot) and compared Raman spectra for both. From this it was estimated that the SC temperature is at most 200 ºC lower than the thermocouple temperature. Figure 12c is a picture of the resistance heating set up during an experiment. The cooling system is required to protect the DAC and optics from mechanical failure.

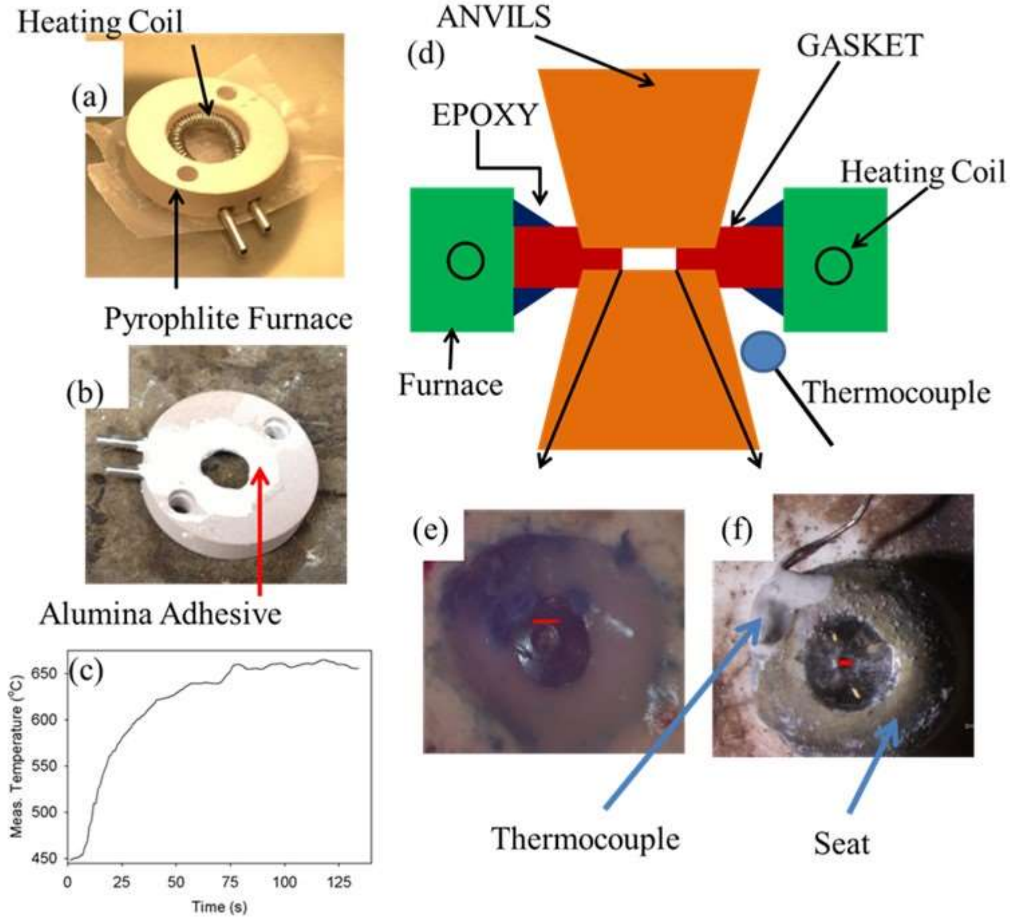

Figure 11 Pictures from the furnace heating experiment. (a) and (b) are pictures of the furnace heater (furnace) before, (a), and after,(b), application of a high-temperature epoxy to hold the Molybdenum heating coils in place. (c) The temporal temperature response to a step current increase inside for a thermocouple placed the center of the furnace without a gasket in place. The time constants to reach equilibrium inside the heater varied depending on the current through the Molybdenum wire, typically inverse time constants were between .02-.04 s^{-1}. (d) Cross-sectional drawing of the DAC for furnace heating. (e) and (f) are pictures of the gasket glued inside the furnace, where (f) also shows the location of a thermocouple glued near the anvil. The scale bars in both pictures are ~300 µm.

4.3 Oven Heating

Figure 12 gives the basic components for the oven heating experiments. For comparison Figure 12a (left) is a picture of the symmetric DAC used in the laser and furnace heating experiments and Figure 12a (right) is the piston-cylinder DAC used for oven heating. The oven heating DAC and gasket are made of Inconel and purchased from D'Anvils. Figure 12b is a picture of the Variac used supply the appropriate power for oven heating, the PID controller which controls the current through the heating wires (made of nichrome) and monitors the temperature, and the oven. A small hole in the bottom of the oven is used to place the thermocouple into contact with the DAC. Figure 12d is a picture of the oven heating setup during an experiment. To prevent oxidation a 98 % Ar and 2% H_2 gas mixture flows through the oven during high-temperature application, labeled as "reducing gas". The window in the oven allows *in situ* Raman spectroscopy, and the heating wires are also labeled. As mentioned in the previous chapter, the temperature difference between the thermocouple and the SC in the oven design is on the order of 10 ^{o}C.

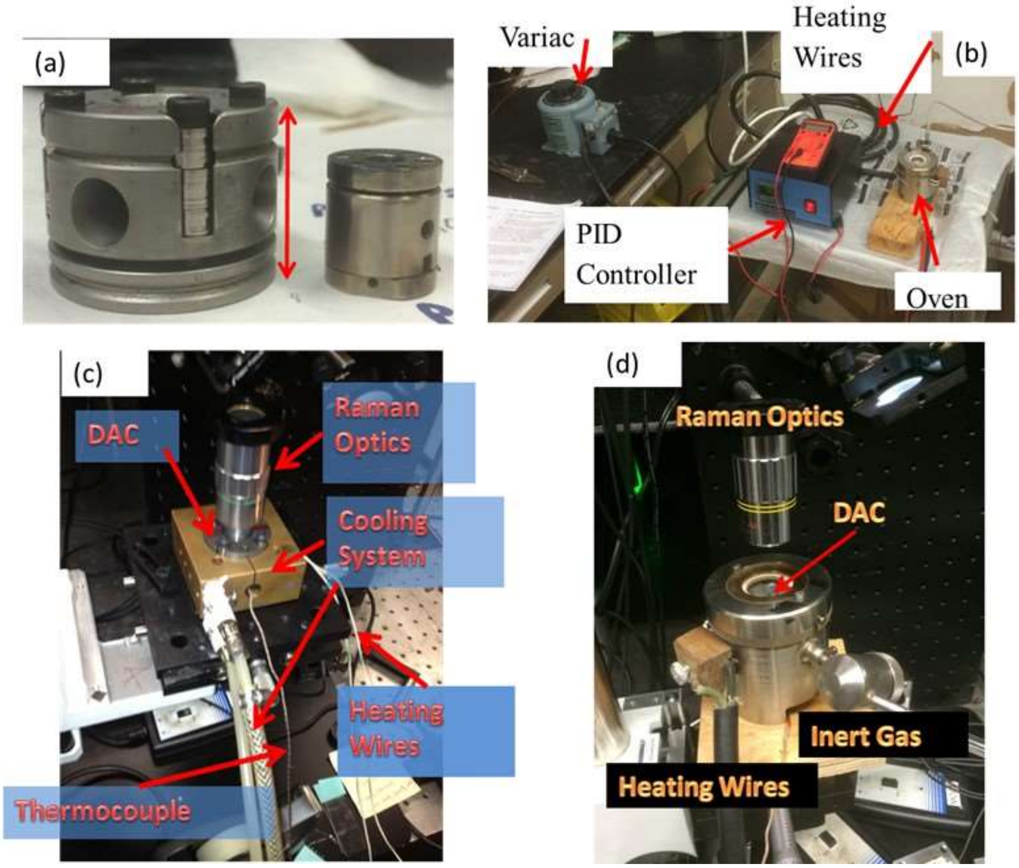

Figure 12 (a)Two types of DAC used in the HPHT experiments, the symmetric cell (left) and the piston cylinder (right). The symmetric cell is used for the laser and furnace heating. The piston cylinder is used in the oven heating experiments. (b) The main components of the oven heating system. The Variac supplies the necessary power to the PID controller monitors the temperature inside the oven using a thermocouple and controls the current through the Nichrome heating wires. (c) The furnace heating experiment. The DAC is encased inside a cooling system to protect it and the Raman optics from mechanical failure. (d) Picture of the oven heating experiment. Throughout the heating process a 98 % Ar and 2% H_2 gas mixture flows through the oven to protect the diamond anvils from oxidizing. The window at the top of the oven allows *in situ* Raman spectroscopy during HPHT.

4.4 Post Analysis

PL and Raman spectra were measured using home-built confocal microscopes, and the resulting nanocrystals were imaged using scanning electron microscopy (SEM) and high resolution transmission electron microscopy (HRTEM). For most experiments the product was transferred onto a Si substrate using a W needle after removing the Re gasket from the DAC. The Si substrate was used to reduce charging effects for SEM imaging. For the HRTEM analysis the product was removed from the Si substrate and dropped onto a TEM grid (carbon film on a copper mesh, 10nm thickness) using the needle.

Aside from Raman and PL spectra, optically detected magnetic resonance, and anti-bunching were measured on the samples which grew NV^- centers.

CHAPTER V

EXPERIMENTAL RESULTS

There were three main types of HPHT experiments conducted with the DAC. The first studied the HPHT behavior of adamantane using laser heating to high temperatures to verify that ND would form from organic precursors as in prior work []. The second set of experiments used the furnace heating method, Figure 11, in order to make the temperature of the SC more uniform and to better understand the growth mechanism of ND from adamantane. And the third procedure used oven heating with the piston-cylinder DAC, Figure 12, to facilitate even better uniformity and accurate measurement of the SC temperature and to test the seeding technique. The details of the experimental procedures are given in Chapter IV.

5.1 Laser Heating Experiments

Laser heating experiments were conducted on pure adamantane and adamantane mixed with other organic compounds at high-pressure to determine how the Raman spectra of decomposed organics appears during growth. After growth SEM and TEM were used to identify the different types nano-carbon allotropes created by the decomposition of adamantane. Later, fluorescence spectroscopy was performed to determine whether color-center defects were formed.

We learned from the laser heating experiments that under a wide range of HPHT conditions NDs do grow, and that for sufficiently high temperatures the NV^- and SiV defect centers will be created either by simply mixing pure diamondoid molecules with nitrogen or silicon dopants. However, it was difficult to determine whether the NDs were created by the adamantane molecules dehydrogenating and then "bonding" together, or if the adamantane completely decomposed under the HPHT conditions and consequently formed the ND by "self-nucleation".

Due to the small spot size of the heating laser it was also impossible to create a uniform temperature inside the SC, and therefore the exact growth conditions were never accurately determined. But despite these draw-backs the information obtained from the experiments was valuable in conducting further HPHT experiments using furnace and oven heating.

5.1.1Materials and Methods

The exact details of the three most important laser heating experiments are given in Table 3. For experiment LN the initial pressure was 24 GPa. Argon was used as a pressure transmitting medium and heat insulator allowing temperatures up to 1800 ºC.[4] The mixture of adamantane and AZADO was loaded into the hole of the Ti washer (6 μm thick, 10 μm inner diameter), which was placed inside the SC. For the entire experiment the temperature inside the laser heated portion of the SC was measured by monitoring the thermal radiation and fitting the spectra to a Planck curve, Figure 10(b).

---

[4] Using a pressure transmitting medium is not required to conduct laser heating HPHT experiments inside a DAC. The reason is to allow higher temperatures inside the SC. Using a pressure transmitting medium was eventually abandoned because it was determined that the high temperatures it allows are not necessary to create the NDs.

Table 3 Details about the various HPHT growth experiments used to produce the USNDs with laser heating. The experiments LN, LA, LS correspond to nitrogen doping (with AZADO), pure adamantane, and silicon doping, respectively. The highest temperature laser heating experiment LN used Ar as a pressure transmitting medium and heat insulator.

Exp	Pressure (GPa)	Max. Temperature (°C)	Growth time (s)	Mixture	ND Size (nm)	Defects
LN	24	~1700	~10	AZADO	<100	NV
LA	30-45	<1200	~10	Adamantane	2-10	NV (?)
LS	30	<1200	~10	Si Powder/ Adamantane	?	SiV

For experiments LA and LS the SC was completely filled with either adamantane or adamantane/Si powder mixture, respectively. The growth pressures ranged from 30-45 GPa. Because argon was not used the maximum temperature inside the SC was lower than experiment LN.

As mentioned previously PL and Raman spectra were measured both during and after growth using home-built confocal microscopes, and the NDs were imaged using scanning electron microscopy (SEM) and high resolution transmission electron microscopy (HRTEM). For SEM imaging the product was transferred onto a Si substrate using a W needle after removing the Re gasket from the DAC. The Si substrate was used to reduce charging effects for SEM imaging. For the HRTEM analysis the product was then removed from the Si substrate using the W needle and dropped onto a TEM grid (10nm thick carbon film on a copper mesh).

It should be noted that during the laser heating experiments flashes were observed when the laser was focused onto the Ti coupler. These flashes are assumed to correspond to either the decomposition of the organic molecules or the creation of nano-carbon allotropes. The “life time” of the flashes was typically ~10s, and it is this observation which is used to estimate the “Growth Time” column in Table 3 Details about the various HPHT growth experiments used to produce the USNDs with laser heating. The experiments LN, LA, LS correspond to nitrogen doping (with AZADO), pure adamantane, and silicon doping, respectively. The highest temperature laser heating experiment LN used Ar as a pressure transmitting medium and heat insulator. .

5.1.2 Results

Figure 13gives data from the pure adamantane experiment LA. HRTEM analysis revealed USND with sizes between 2–10 nm Figure 13(a-b) and also large numbers of two-core OLC with sizes ranging between 10–50 nm Figure 13(d). No other forms of carbon nanoparticles were imaged, and the yield of the NDs was much lower than the two-core OLC particles. Figure 13(a) is an HRTEM micrograph of several NDs of about 5 nm in size and Figure 13(b) is a magnification of one of the NDs. Figure 13(d) shows a representative two-core OLC nanoparticle, most of which have a size of ~30-40 nm. It should be noted that OLC can be grown using e^--beam irradiation inside a TEM[39], however this is unlikely here because the electron irradiation energy (80 keV) was too low.

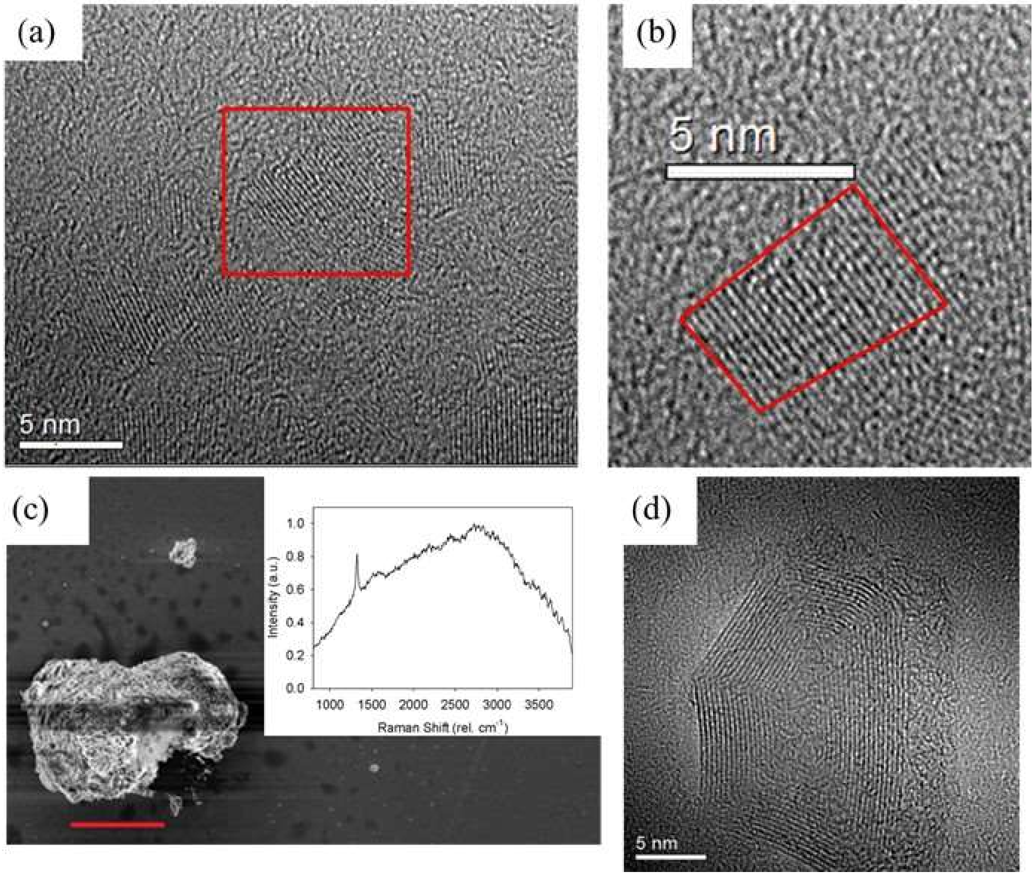

Figure 13. HRTEM and SEM micrographs from experiment LA. (a) Weakly agglomerated NDs. (b) Magnification of the ND outlined in red in (a). (c) SEM image of adamantane-like residue with a hole caused by the 532 nm Raman laser when extracted from the SC, the scale bar is 10 µm. The inset shows the Raman ND peak and NV^{-} like emission spectra taken when the laser was first focused on the residue, before the hole was burned. (d) HRTEM micrograph of two-core OLC particle created during the experiment.

The majority of the HRTEM images have a poor contrast which is most likely due to electron-beam induced deposition (EBID) of adamantane residue[40]. The low ND yield may be an artifact of the difficulty in finding the NDs due to the poor contrast, or possibly inhomogeneous material loss during transfer to the TEM grid from the silicon substrate used for the SEM characterization.

The agglomeration seen in Figure 13a probably did not occur during growth[41], but is most likely due to columbic forces since we also found many isolated NDs in the HRTEM analysis.

Figure 13(c) and inset show an SEM image of adamantane extracted from the SC after laser heating. Here the NDs were found to be embedded in a matrix of adamantane-like consistency which was easily melted or evaporated by the green laser used to observe PL after removal from the DAC.

Figure 14 gives data from the Si doping experiment LS. The importance of this experiment is that direct observation of the decomposition of adamantane under HPHT was carried out Figure 14(a) by measuring the Raman spectra of the adamantane CH modes (488 nm excitation). As the laser power is increased (red arrow) the peak intensities begin to decay and broaden, suggesting the dehydrogenation and/or thermal decomposition of the adamantane. Other evidence of dehydrogenation is the observation of visible flashes (white to light blue in color), when the 1.06 μm laser is focused onto the Ti coupler washer.

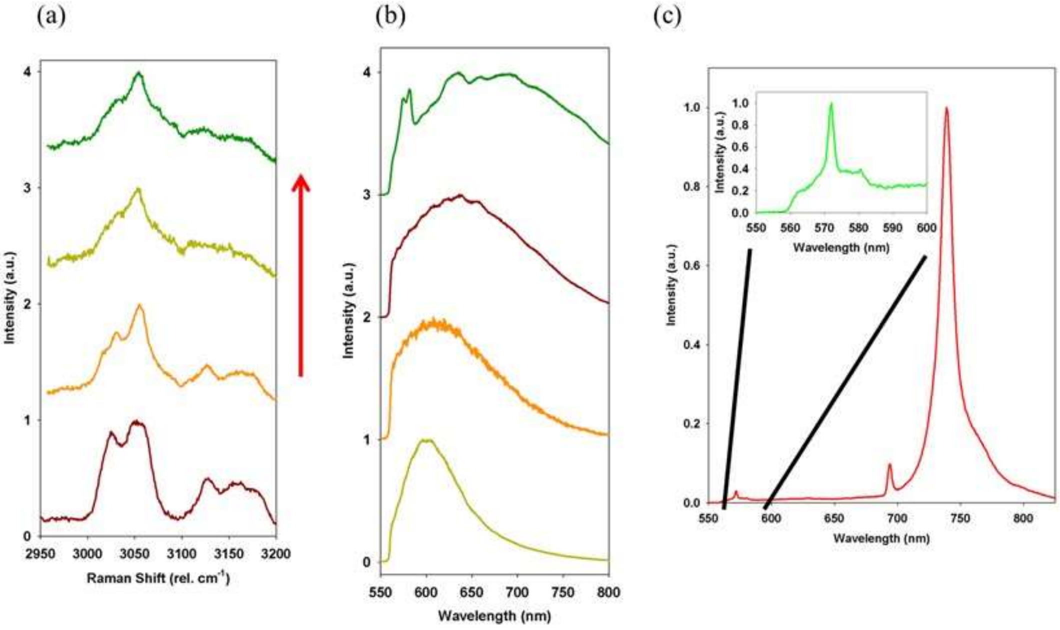

Figure 14. Raman and PL data from the Si doping experiment LS. (a) In situ Raman data of the CH Raman peak of adamantane as the laser power is increased (direction of arrow). As the laser power (and hence the temperature) increase the CH modes begin to decay and broaden, giving direct evidence of the decomposition of adamantane. (b) Various PL spectra of different samples taken outside of the DAC after HPHT, the peak position and width are predicted to be related to the size of the ND, the color-center concentration or surface properties (see text). c) PL spectrum of NDs with SiV. The inset shows the nanodiamond Raman peak.

Figure 14b shows examples of typical PL spectra found when the NDs were removed from the DAC. As can be seen the width and position of the maximum of the emission peak varies. Such diversity in the ND PL spectra has been observed by previous scientists, [42], and is thought to depend on the size, color-center concentration and surface properties of the NDs.

We also observed SiV centers as shown in Figure 14(c). The importance of this observation is that it proves that color-center defects may be incorporated directly inside the ND lattice by mixing molecules with the required defect atom (in this case the molecule was pure Si powder). HRTEM analysis was not performed on the NDs from this experiment, but the growth conditions were similar to experiment LA in which 2-10 nm USNDs were observed.

Figure 15 gives data from the LN laser heating experiment using a mixture of adamantane and AZADO. From the success of the Si doping experiment it was postulated that if adamantane was mixed with a N-containing source (such as AZADO) then NV centers could be created during laser heating HPHT. The architecture for this experiment was different than LA and LS in that the hole of the Ti coupler Figure 10(c) was filled with the adamantane/AZADO mixture (instead of filling the entire SC with the mixture). After growth double-sided tape was used to extract the NDs from the anvils and was subsequently placed on a cover glass that was annealed at 750 ^{o}C for 20 minutes to ash the tape.

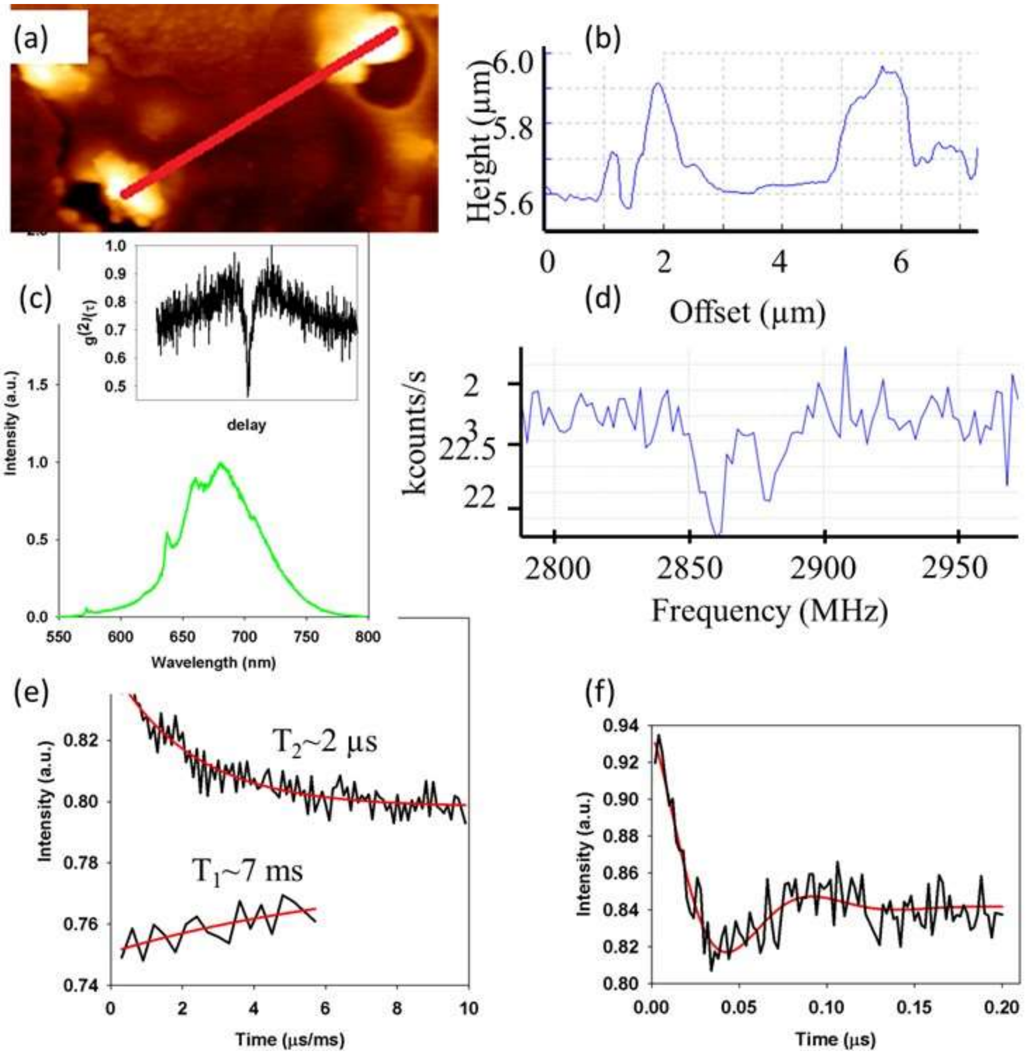

Figure 15. Data taken from the NDs of experiment LN. (a) AFM image of the ND clusters whose emission spectra were recorded. The residue from the double-sided tape used to extract the NDs from the DAC is clearly visible. (b) The height profile along the line marked in the AFM image in (a). (c) NV$^-$ PL spectra of one of the ND clusters in (a). The inset gives anti-bunching data, the contrast of which predicts about 3-4 NVs within the measurement volume. (d), (e) and (f) are ODMR, coherence time, and Rabi nutation data, respectively.

AFM measurements Figure 15(a and b) of the product revealed the NDs to be agglomerated (although this most likely did not occur during growth given the data from Figure 13) but rather is an artifact of using the double-sided tape to extract the sample.

The measured height of the clusters Figure 15(b) is about 200-250 nm which may be an artifact of the tape residue used to extract the NDs (as can be seen in the AFM image).

PL data from the NDs as well as anti-bunching measurements of the NDs, which give evidence of non-classical light emitters, is presented in Figure 15c. The PL spectra is a clear sign of the NV center and the contrast in the anti-bunching data is consistent with about 3-4 NVs within the measuring volume[43].

Data from ODMR measurements is presented in Figure 15(d). As can be seen the spectrum is split under zero applied external magnetic field, which is typical for NV in ND due to strain[44]. The measured T1 and T2 times of the NV spin coherence are presented in Figure 15(e). The coherence times are shorter than for NVs in bulk diamond, which may be due to coupling with the ND surface defects, the tape residue or to the high concentration of NVs within the ND.

Rabi oscillation data is presented in Figure 15(f). The Rabi oscillations decayed about 100 times faster than the T2 measurements Figure 15(e), which is most likely due to inhomogeneous broadening caused by multiple NV centers with different orientations, an assertion that is supported by the anti-bunching data (inset in Figure 15c).

5.1.3 Conclusions

The HRTEM images in Figure 13 imply the most stable nano-size forms of carbon grown under the laser heating HPHT conditions are 2-10 nm for diamond and 10-50 nm OLC with one and two-cores. Emission spectra suggestive of NV were observed for several growth runs, however the only clear evidence of NV (i.e. anti-bunching and ODMR measurements) was found for the NDs grown by the high temperature (~ 1700 ºC) laser heating experiment from a mixture of AZADO and adamantane and subjected to an air annealing after growth. This is significant because NVs were form without any post-irradiation and vacuum annealing.

Evidence of SiV was seen in experiment LS where elemental Si was incorporated into the reactants. This is significant because prior work required the use of organosilicon compounds to create SiV, see Davydov[45].

The clear boundary in size distribution between the NDs (2-10 nm) and the OLC (10-50 nm) (which was also seen by HRTEM in the resistance heating experiments) imply that the NDs may be the first species to form inside the SC, then after reaching ~ 10nm in size the NDs begin to convert to OLC. This is in agreement with prior experiments [46] ,[47]. However, many theoretical and numerical models predict the opposite (i.e. OLC is stable for sizes < 1.9 nm and USND for sizes < 5.4 nm) [48]and[49], and so there is no clear mechanism to account for the data. It should be noted that OLC has been observed to form from ND and then revert back to ND[50].

There were two main features of ND growth learned from these experiments. The first is that total decomposition of the initial diamondoid is not necessary for the ND growth, as is evidenced from the Raman data and the SEM pictures in Figure 13c (which shows evidence of organic-like residue). The importance of this observation is that ND growth happens at lower temperature than that needed for total decomposition of the initial growth material. Therefore, a mechanism of controlled (seeded) growth may be implemented.

The second observation is that color centers may be incorporated into the ND at pressures and temperatures below total decomposition of the growth material. Which like the first observation is important in developing techniques for the controlled growth of color center NDs.

Whereas the evidence presented from the laser heating experiments shows ND and color center formation without total decomposition of the starting material, the evidence is not unambiguous because we do not know the exact HPHT conditions at which ND formation begins. To obtain better, unambiguous data, and have a thorough understanding of the required HPHT conditions, resistance heating experiments were conducted next. These allow better control, uniformity, and more accurate measurement of the SC temperature.

5.2 HPHT Furnace Heating Experiments on Adamantane

To better understand the properties of adamantane, which will later be used as a seed for controlled ND growth, a set of HPHT furnace heating experiments (Figure 11) were conducted. The HPHT properties of adamantane which were analyzed are: phase transitions, de-hydrogenation conditions, decomposition, molecular deformation, and the formation of ND or other carbon allotropes.

As mentioned previously pure adamantane is a Van der Waals crystal with only weak interactions holding the crystal together. Hence, the HPHT stability conditions for adamantane in molecular crystal form should be similar to those for adamantane dissolved in as a seed molecule in a hydrocarbon.

As with the laser heating experiment LN, HRTEM analysis from some of the experiments found 2-10 nm ND and 20-60 nm one and two-core OLC. However, as will be seen the decomposition of adamantane in the furnace heating experiments is even less that in the LN experiment. Nonetheless partial dehydrogenation of the sample is predicted based on blue shifting of the Σ and Γ Raman modes (to be shown later), and the appearance of a liquid inside the SC which quickly evaporated when pressure is released.

5.2.1 Materials and Methods

Four HPHT experiments using furnace heating and one high-pressure ambient-temperature experiment were preformed inside a DAC using the architectures given in Figure 11 and Figure 12c. For all experiments the gasket material was Re with a pre-indentation pressure of ~ 20 GPa. The cylindrical SC was ~100 μm in diameter and ~20 μm thick. No pressure transmitting medium was used. The pressure inside the DAC was monitered using either the ruby PL method or monitoring the high frequency edge of the first order Raman band of the diamond anvils[51], Figure 16.

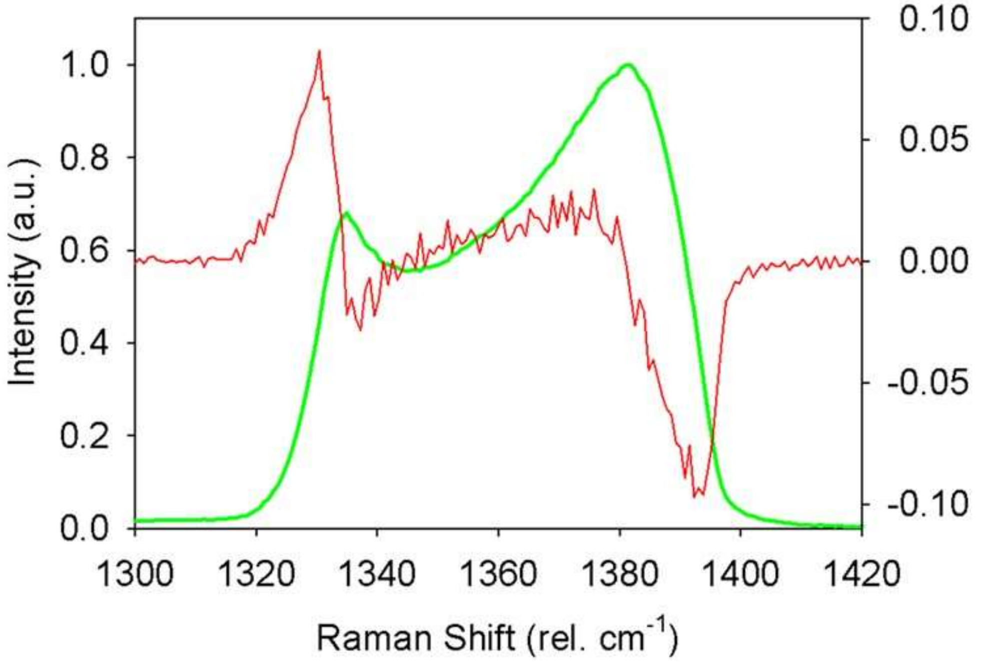

Figure 16 a) Method for estimating the pressure inside the SC by using the high frequency edge of the first order diamond anvil Raman band[51]. The green curve is the first order Raman intensity, left axis, and the red curve is the first derivative, right axis. The minimum of the derivative locates the high frequency edge of the Raman band. The relationship between the edge position and pressure is found in[51].

In the following sections, experimental results will be reported. In the analysis of these results, a number of theoretical curve fitting techniques were used to attempt to identify the physical processes that could explain the observed data. Specifically, studies will be made of changes in the Raman spectra (especially mode frequencies and widths) vs changes in temperature and pressure.

To quantify the Raman mode shifts three different types of exponential fits were considered as a model for the peak position dependence on temperature and pressure, although other authors have used a linear fit for the data[52]. For experiments in the pressure range near the β→γ transition (~18 GPa) the peak positions fit to an exponentially increasing function

$$g(T) = y_o + ae^{bT}. \tag{21}$$

And for experiments well above the β→γ transition (> 30 GPa) the peak positions fit to an exponential rise towards a maximum shift

$$h(T) = y_o + a(1 - e^{-bT}). \tag{22}$$

The third type of fit corresponds to a blue shift of peak positions according to an exponential decay after some initial temperature is reached.

$$f(T) = y_o + ae^{-bT}. \tag{23}$$

The parameters for these exponential fits and their linear approximations are given in Table 4 for the various furnace heating experiments conducted on pure adamantane.

Table 4 Data for the HPHT experiments on Adamantane. The final column represents the slope if the exponential fits are approximated linearly. For experiment RH1 the equations are fitted to the data before the discrete blue shift transition.

Experiment	Initial Pressure(GPa) / Max. Temp. (^{o}C)	Eq.	Raman Mode[3]	y_o	a (cm^{-1})	b (^{o}C^{-1})[1]	m (cm^{-1}/ ^{o}C)[2]
RH1	27 / 789	g(T)	Σ_γ	890.6	4.955	.0025	.0124
			Γ_1	3080	11.54	.0027	.03116
			Γ_2	3014	22.70	.0018	.0409
RH3	22 / 271	g(T)	Σ	816.2	39.32	.0026	.1022
			Γ_1	2987	52.22	.0028	.1462
			Γ_2	2958	49.46	.0025	.1237
RH6	21 / 292	f(T)	Σ	852.3	59.07	.0070	.4135
			Γ_1	2981	112.4	.0031	.3484
			Γ_2	2936	101.8	.0014	.1425
RH7	46 / 404	h(T)	Σ_γ	952.2	10.75	.0074	.0796
			Γ_1	3183	32.05	.0166	.5320
			Γ_2	3131	15.02	.0072	.1081
Z1	18 / 24	g(T)	Σ_β	873.1	3.035	.0870	.2640
Z4/Z7	18-43/24	g(T)	Σ_γ	753	317	.0220	6.974
			Γ_1	2845	368.3	.0304	11.19632
			Γ_3	2886	643.2	.0218	14.02176
			Γ_4	2893	728.0	.0232	16.8896

1 These units do not apply to the rows labeled “Z1” and “Z4/Z7”. For these rows the ^{o}C^{-1} in the column heading should be replaced by GPa^{-1}

2 The units for do not apply to the rows labeled “Z1” and “Z4/Z7”. For these rows the (cm^{-1}/ ^{o}C) in the column heading should be replaced by cm^{-1}/GPa

3 The nomenclature in the column labeled “Raman mode” in

Table 4 is as follows: The capital greek letter gives the CC or CH mode (Γ for the CH modes and Σ for the CC modes). For the CC modes the subscript indicates the phase of adamantane in accordance with nomenclature of this dissertation. For the CH modes the subscripts are numbers that agree with the assignment in Figure 9b

Using these equations and parameters, attempts will be made to quantify pressure and temperature induced changes in the peak positions of the Raman Σ and Γ modes. This will give insight to phase changes and molecular deformation[52]. This is because the in situ Σ and Γ Raman lines are expected to be sensitive to volume changes, phonon interactions and anharmonicity[53].

As will be seen both 532 and 488 nm excitation wavelengths were used for the *in situ* high-pressure ambient-temperature measurements (Z1, Z4 and Z7). However only 532 nm excitation was used for the furnace heating experiments. The maximum temperatures reached for the furnace experiments were limited by failure of the heater wire due to melting or oxidation of the wire.

5.2.2 High Pressure Ambient Temperature Experiments

Data from the high-pressure ambient-temperature Raman scattering experiments is given in Figure 17. The excitation wavelength for the experiments in Figure 17a and b are 532 nm and 488 nm, respectively.

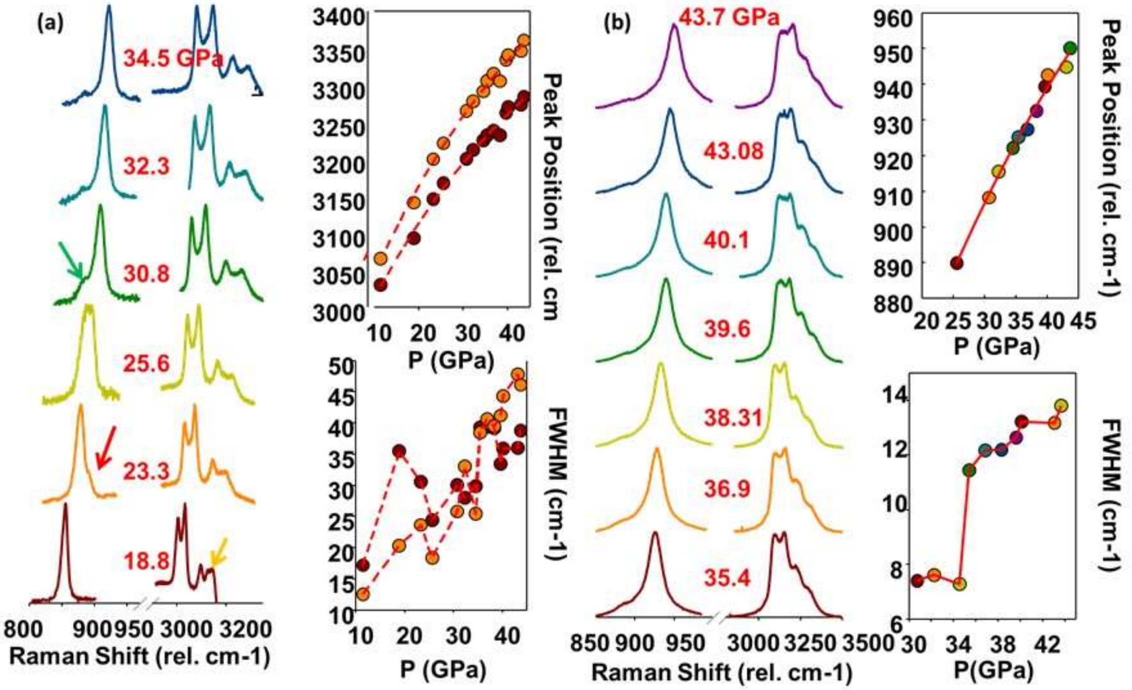

Figure 17 High-pressure ambient-temperature Raman scattering data. (a) Σ and Γ Raman spectrum during the β→γ transition, the excitation wavelength is 532 nm. The red arrow points to the second peak appearing in the Σ spectra as pressure is increased, and is associated with the γ-phase. The green arrows point to the Σ mode in the β-phase just before it disappears at higher pressures. There are also peaks disappearing in the CH spectra as the pressure is increased. The yellow arrow points to Σ_β as the β→ γ transition occurs. Note that the CH modes are always ahead of the CC modes when phase transitions occur. Insets in (a) are the peak positions of the Γ_1 (dark red) and Γ_2 (orange) modes The top plots show the peak positions and the bottom plot shows the FWHM. (b) Raman spectra in the higher pressure γ-phase, except for the lowest pressure CC spectra which still has a small peak below 900 cm^{-1} implying the crystal has not completely converted to the γ-phase. The excitation wavelength is 488 nm. The insets are the peak positions (top figure) and FWHM (bottom figure) of Σ_γ. The red line in the FWHM inset is a guide for the eye, whereas the red line in the peak position inset is the exponential trend.

The lower pressure regime, Figure 17a, depicts the β→γ transition signaled by the appearance of the double peak (red arrow) appearing in the Σ mode around 23.3 GPa, and the disappearance of CH stretch modes (yellow arrow) in between the Γ_3 and Γ_4 peaks around 19 GPa. The new Σ mode peak associated with the γ-phase, Σ_γ, becomes dominant in the pressure range of 23-30 GPa while simultaneously the β-phase Σ_β peak (green arrow) loses intensity.

Notice that the Σ_β is visible up to 35 GPa, whereas the peaks associated with the β-phase in the Γ modes are not visible above 30 GPa. Similarly, the Γ modes first appear at the lower pressure of 18 GPa before the Σ_γ is visible. Thus the CH modes lead the CC modes in signaling the phase transition with increasing pressure. This is a consequence of the CH bonds being the first to be affected by volume contraction at high-pressure.

Above 35 GPa the Γ peaks begin to broaden substantially and merge, with Γ_2 having the largest intensity, a trend which is also seen in the high temperature experiments. Note that the sudden increase in the FWHM for all measured Raman modes around 35 GPa is most likely due to the change in excitation wavelengths from 532nm to 488 nm. Nonetheless, in the high pressure regime, there is a faster increase in the FWHM vs pressure. This is most likely due to an increase in molecular distortion and/or interaction. From the data in Figure 17, the parameters given in Table 4 (rows Z1 and Z4/Z7) are derived.

5.2.3 Experiment RH1

The Raman spectra for experiment RH1 is presented in Figure 18 and the experimental parameters are given in

Table 4. The initial phase of the adamantane was an admixture of the β and γ phases, as can be seen from the double peak of the Σ mode (black arrow in Figure 18a). The sample completely evolves into the γ-phase around 430 °C. As the temperature is further increased above 650 °C the peak position of all measured modes changed direction and decreased (blue-shifted). Specifically the Σ peak position decreased by about 40 cm^{-1}, and the Γ modes decreased by about 35 cm^{-1} for the lowest frequency mode and 75 cm^{-1} for the highest. This blue shifting was not a step response as it first appears in Figure 18 but a more gradual change that occurred on the time scale of ~5 minutes as verified by taking 1 second Raman spectra as the temperature increased. This blue shifting is initially accompanied by an increase in the pressure from 30 to 32 GPa. However as the temperature is further increased, the pressure begins to decrease, yet the Raman spectra begins to red shift. At the highest temperature a broad shoulder begins to appear in the 3300 cm^{-1} range (green arrow in Figure 18b). This high-temperature transition around 780 °C may be a consequence of partial dehydrogenation of the adamantane and subsequent polymerization of the Carbon radicals to form higher order diamondoids and other allotropes of carbon including ND. The prospect of this transition being due to a phase change like melting is unlikely because the melting temperature is typically higher at high pressure.

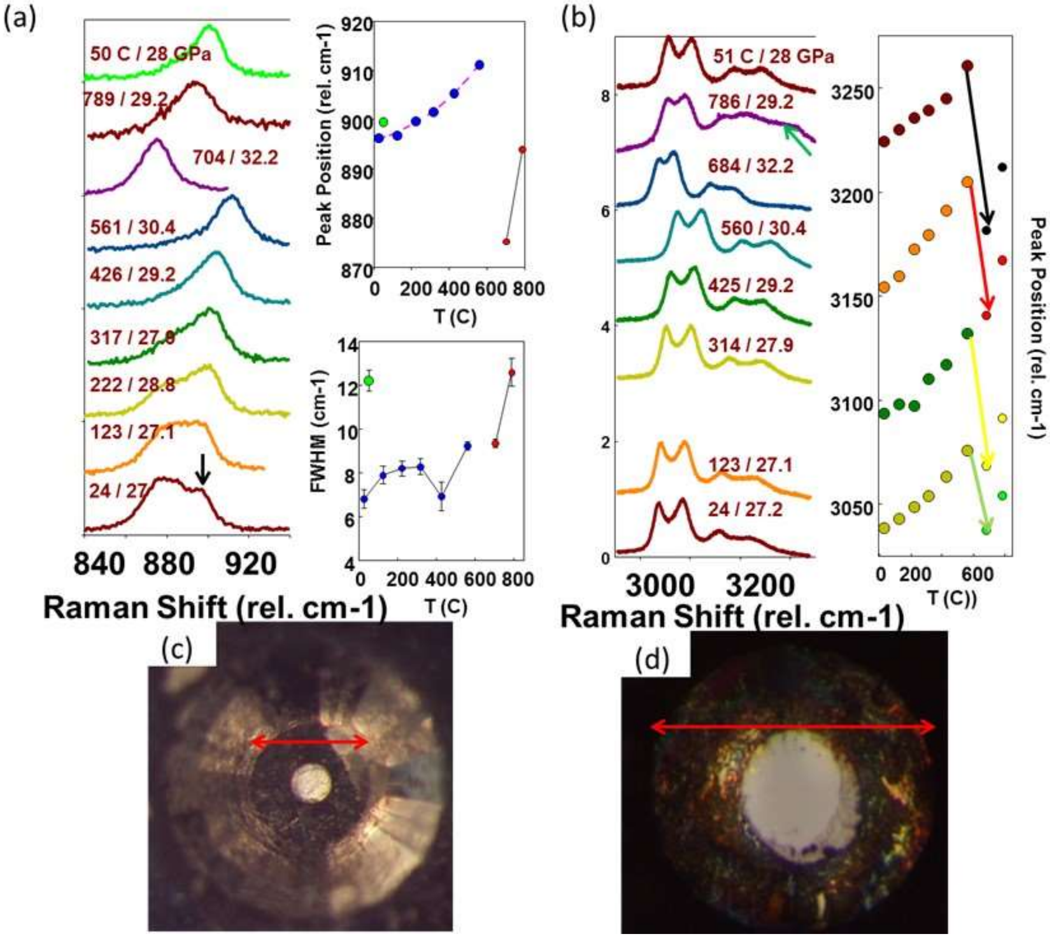

Figure 18 HPHT Raman data from experiment RH1 for the Σ (a) and Γ (b) modes of adamantane, the initial pressure was 27 GPa. The black arrow in (a) depicts the Σ_γ mode which is analyzed in the insets. The top inset shows Raman peak positions and the bottom inset shows FWHM vs pressure. In the insets the blue and red data points represent the Raman peak positions (or FWHM) before and after the sudden blue shift, respectively. This blue shift might be interpreted as a β→γ phase transition. The green points show the peak positions (or FWHM) after the temperature is returned to ambient (quenched) but still at high pressure. The inset in (b) gives the peak positions of the Γ modes as a function of temperature, the arrows are used to track the shifts in the locations after the transition. (c) and (d) are pictures with the gasket loaded with the sample at ambient conditions, where (c) is before and (d) is after heating. The scale bar in both is 100 µm.

After the temperature quench the peak positions returned a value associated with higher pressures and temperatures (~28 GPa and 300 °C). This hysteresis is not typical of measured phase transitions of adamantane [52] and[54], implying there was a chemical reaction during the HPHT. This hypothesis is further supported by comparing experiment RH1 to Z1. Specifically, for experiment RH1 (Figure 18) the high-temperature caused the β→γ transition, compared to high pressure in experiment Z1 (Figure 17). However, the temperature increase caused an exponentially increasing shift in peak positions (equation 21), compared to pressure which caused a shift of peak positions toward a saturated value (equation 22). This exponential increase is expected for activation of phonon modes [reference] which might enable the adamantane molecules to come closer together and react.

5.2.4 Experiment RH3

The Raman spectra for experiment RH3 is given in Figure 19 . As depicted in the insets, the temperature dependence of the peak positions increased with an exponential behavior similar to experiment RH1. An anomaly with this experiment is that the initial pressure was measured to be 32 GPa immediately after preparation. However the pressure dropped to 21 GPa in the time it took to transfer the cell from the preparation area to the growth setup. Such a pressure drop could be due to deformation in the gasket before the experiment was started, or to pressure gradients in the SC. The fact the the peak positions increased during heating and did not decrease implies that the SC did not deform during the HPHT part of the experiment.

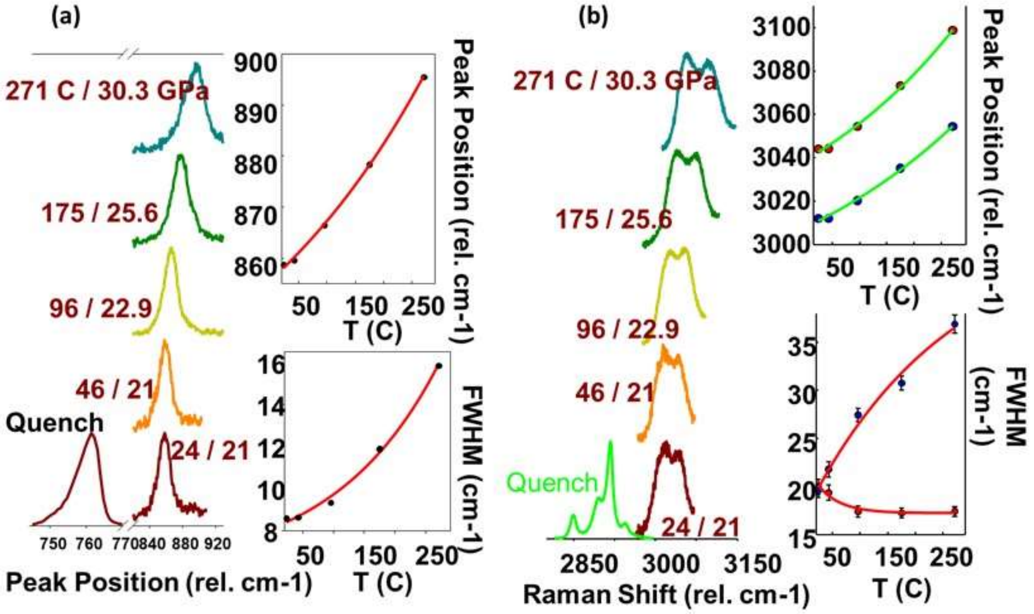

Figure 19. HPHT Raman data for experiment RH3. The initial pressure is 21 GPa. (a) Raman spectra for the Σ mode as the temperature is increased. The insets show peak position (upper) and FWHM (lower). (b) Raman data for the Γ_1 and Γ_2 modes as the temperature is increased. The insets show peak position (upper) and FWHM (lower). The blue data points in the insets correspond to Γ_1 and the red data points are Γ_2. The FWHM data for Γ_1 was fitted to an exponential rise to a maximum and the FWHM data for Γ_2 was fitted function to an exponential decay. The spectra taken after the temperature and pressure are returned to ambient, as labelled by "quench" in (a) and (b) look like the original adamantane spectra, i.e. there is no observed hysteresis for this experiment.

Figure 20 shows the Γ_3 and Γ_4 modes for experiment RH3. As seen the Γ_4 mode was difficult to resolve in the Raman spectra (as compatred to RH1), even at room temperature.

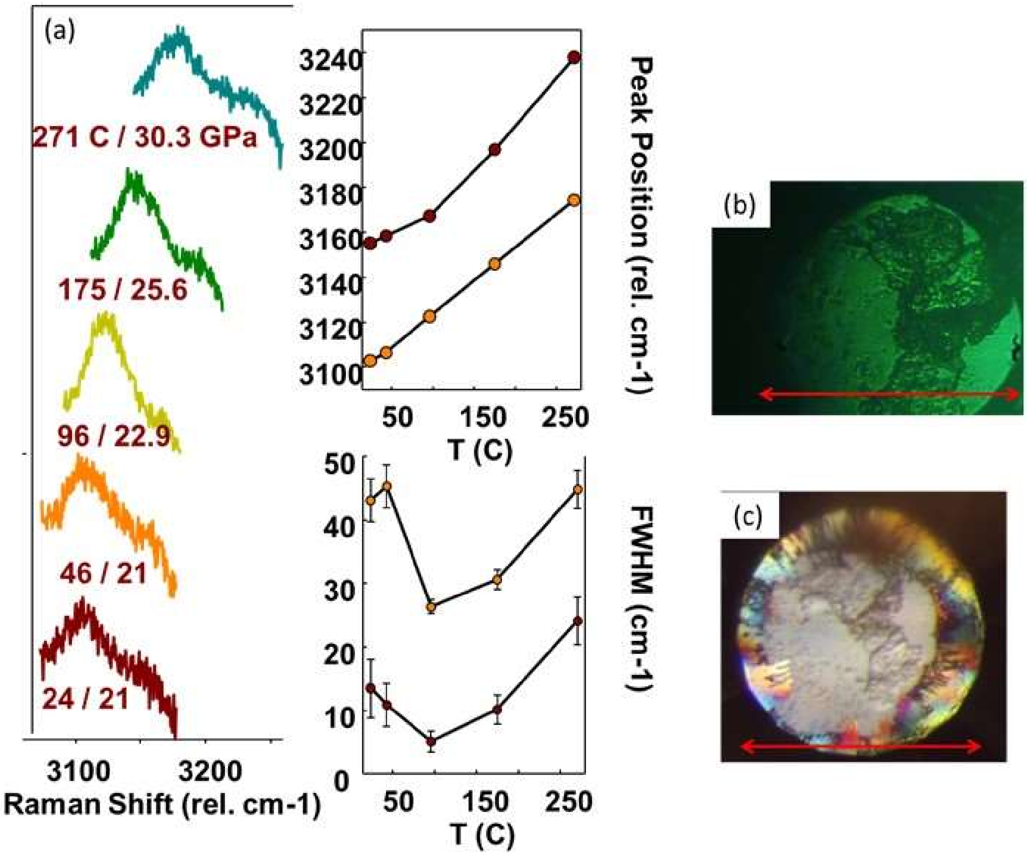

Figure 20 HPHT Raman data for experiment RH3. The initial pressure is 21 GPa. (a) Raman data for the Γ3 and Γ4 modes with insets giving the peak positions and FWHM as indicated. The red data points are Γ4 and the orange are Γ3. (b) and (c) are images of the sample pressurized before and after the high-temperature, respectively, the scale bar is 300 µm.

5.2.5 Experiment RH6

The Raman spectra for experiment RH6 is given in Figure 21, it is important to note that for this experiment the Σ_γ mode was not observed implying the adamantane remained in the β-phase. Whereas both experiments RH6 and RH3 (Figure 19) began around the same pressure, ~21 GPa, the pressure decreased upon heating in RH6 but increased in RH3. Moreover, the Raman Σ_β mode peak positions decreased with increasing temperature in RH6, following an exponential behavior, whereas the peak positions increased in RH3. One possible explanation is that in experiment RH6 the SC deformed as the temperature increased, allowing expansion of the sample. This blue-shifting is typical for high-temperature experiments when the volume is not constrained[53]. This is further supported by the fact that the Γ_4 mode peak height increased with temperature (Figure 21c) implying a decrease in the intra-molecular interactions which is consistent with the observed decrease in pressure. Γ_4 also began blue-shifting from the beginning of the heating. Therefore, it is concluded that in RH6, unlike the other experiments, the blue shift at higher temperature was likely not caused by a chemical reaction but by a deformation of the gasket.

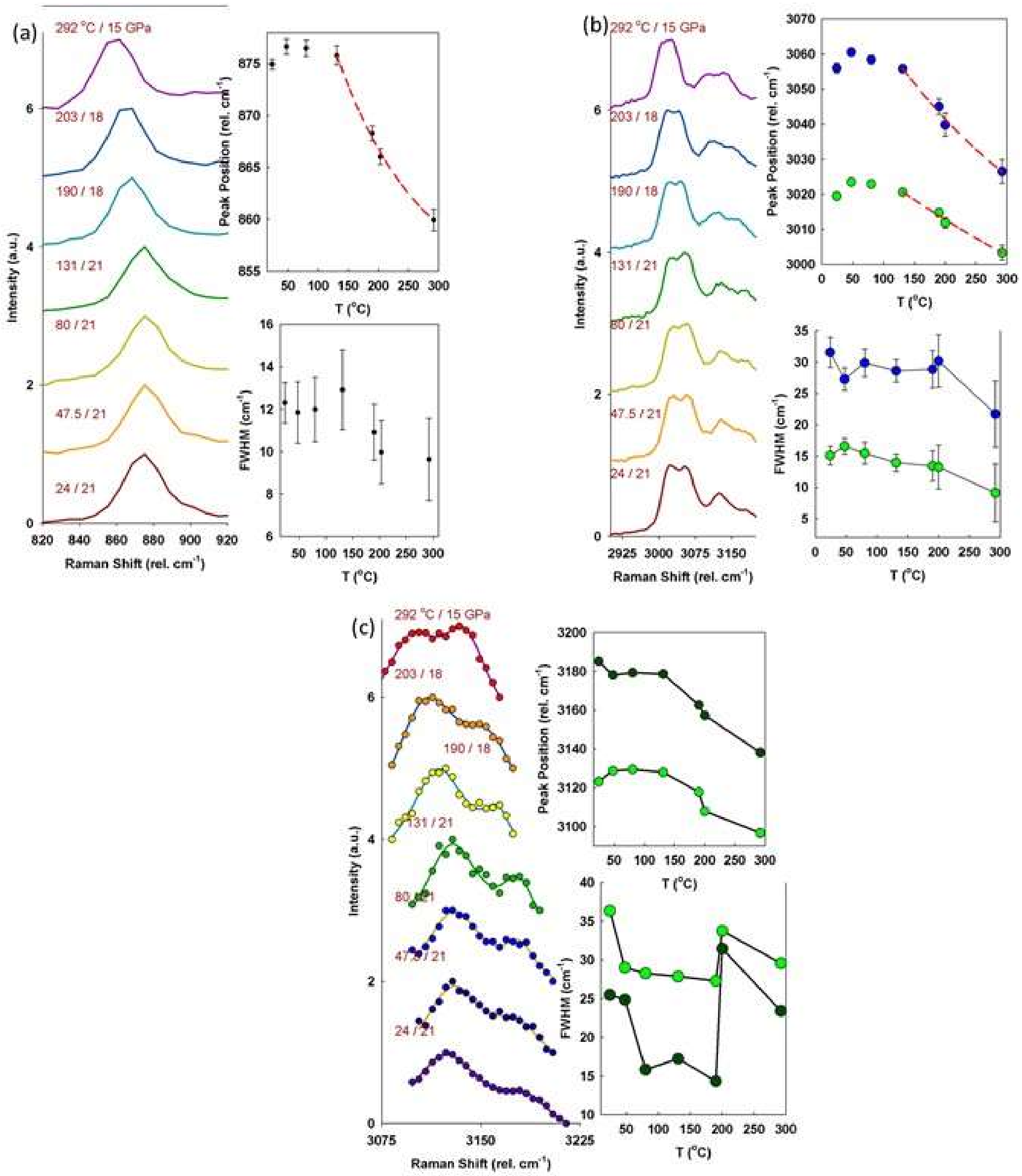

Figure 21 HPHT Raman data from experiment RH6, the initial pressure is 21 GPa. (a) Raman data for Σ_β. The upper and lower insets show the peak position and FWHM, respectively. After reaching a temperature of ~150 ºC the modes begin to blue shift with an exponential decay profile. (b) Raman spectra of the Γ_1 and Γ_2 modes. The upper and lower insets show the peak position and FWHM, respectively. The green data points are Γ_1 and the blue data points are Γ_2. As with Σ_β the Γ modes begin to blue shift around 150 ºC and may be mapped to an exponential decreasing function. (c) Magnification of the Γ_3 and Γ_4 modes. The upper and lower insets show the peak position and FWHM, respectively. The green data points are Γ_3 and the black data points are Γ_4.

5.2.6 Experiment RH7

The Raman spectra for experiment RH7 is given in Figure 22. This experiment began at the highest pressure of 46 GPa, and the final pressure was 49 GPa. Both the Σ and Γ modes did not substantially change position as compared to the previous experiments (only ~8 cm^{-1} increase for Σ). This may be a consequence of steric hindrance due to H…H repulsion at the higher pressure. The peak positions of the Γ could not be readily resolved as they could in the lower pressure experiments.

The pressure also did not increase as the temperature increased above ~200 ºC. Also at around this temperature the FWHM of the Σ mode increased abruptly and then decreased back to its original value as the temperature was further increased (Figure 22a bottom inset).

Another anomaly of this experiment is that once the DAC was opened bubbles appeared and the sample leaked out of the SC onto the diamond anvils. The bubbles may be due to liquid H_2 evaporating upon exposure to the atmosphere since the HPHT growth conditions are within the liquid H_2 stability field[55].

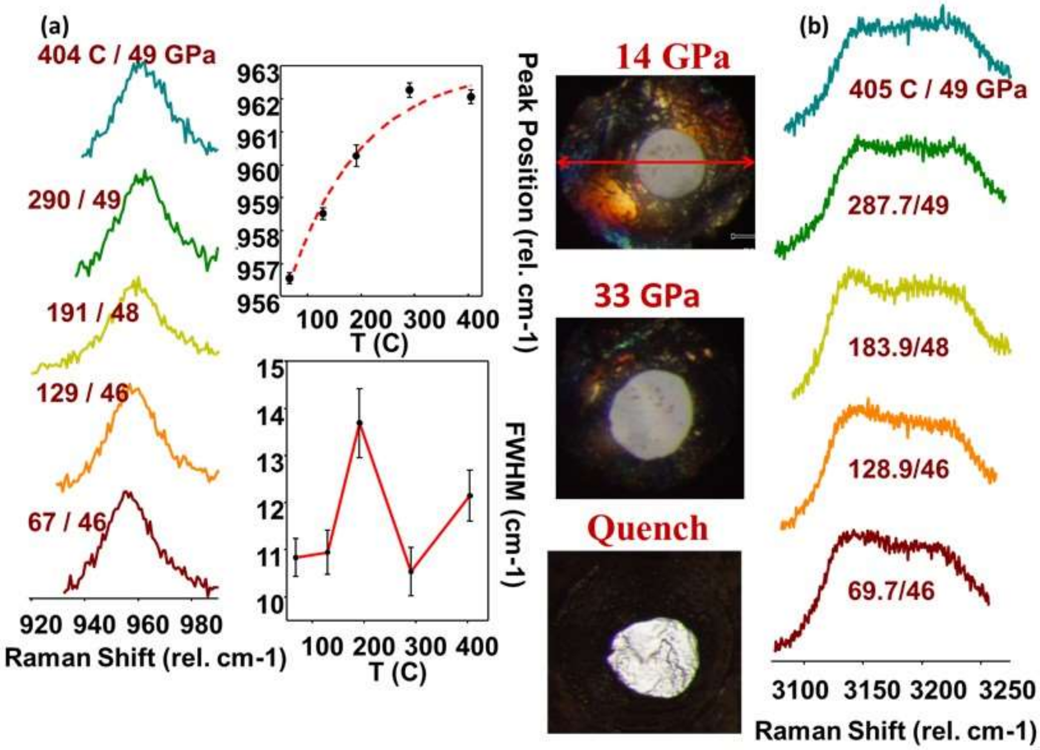

Figure 22 HPHT Raman data for experiment RH7, the initial pressure is 46 GPa. (a) Raman spectra of the Σ mode where pressure and temperatures are as indicated. The upper and lower insets show the peak position and FWHM, respectively. The peak position maps to an exponential rise to maximum with increasing temperature, and the FWHM abruptly increases around 200 ºC but then reduces back to the original value with further increase in temperature. (b) Raman data for the Γ modes. The peak positions could not be identified using SigmaPlot software. The distortion and broadening of the spectra is thought to be due to inter-molecular interactions. The middle three photos are pictures of the SC at 14 GPa, 33 GPa and at ambient temperature and pressure conditions after the HPHT ("Quench"). The photo labeled "Quench" also depicts a liquid-like substance inside the SC.

5.2.7 Conclusions

Experiments Z1and Z4/Z7 (Figure 17) are the highest ambient-temperature measurements made on adamantane thus far. No new Raman active modes could be unambiguously distinguished in the γ-phase. Therefore it is concluded that no new phase changes occur up to 45 GPa in adamantane at ambient temperatures. Although the Γ modes do become obscure at higher pressures (especially Γ_3 and Γ_4) it is more probable that this broadening is due to the molecules interacting and distorting due to the strong H…H repulsion at these high pressures. Furthermore since the red-shifting is correlated with volume contraction, the saturation of the red-shifting of the peak position of the Raman modes implies that the molecules are reaching a critical distance between neighbors.

The most notable part of experiment RH1 (Figure 18) is that a sudden blue shift appeared at high-temperature between 561 – 704 °C. This was due to the temperature increase rather than pressure because it was opposite to the trends observed in the ambient-temperature experiments Z1 and Z4/Z7. Furthermore, the red-shifting in RH1 at lower temperatures followed an exponential rise with temperature, whereas the red-shifting in Z1 and Z4/Z7 followed an exponential decay toward a maximum with increasing pressure. One possible explanation for this difference in functional behavior is that pressure-induced shifts are caused by volume contraction, whereas temperature-induced shifts are cause by phonon activation and anharmonicity[53].

Figure 23a is an attempt to separate pressure and temperature effects. Specifically it gives a comparison of the Raman Σ and Γ modes at a nearly constant pressure of ~ 30

GPa at various temperatures. Only at the highest temperature of ~785 ºC do the Σ modes begin to broaden. In contrast the Γ modes typically always broaden as soon as temperature is increased. This is most likely a consequence of the CH bonds distorting more drastically due to stronger inter-molecular interaction.

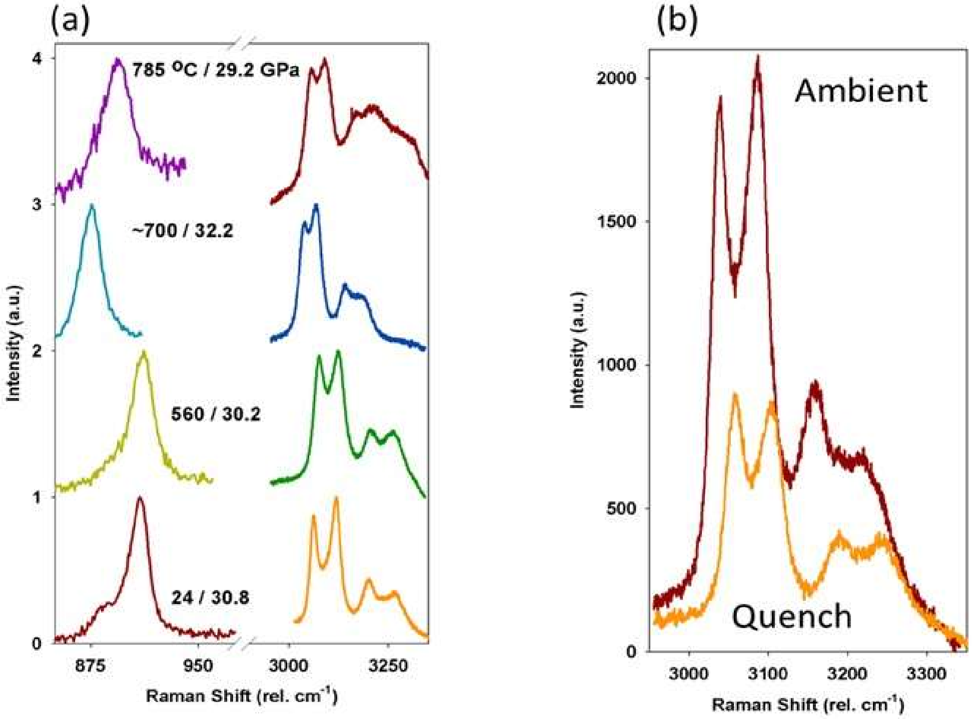

Figure 23 (a) Raman data showing Σ and Γ regions at different temperatures around the same pressure. Specifically the bottom row shows ambient-temperature whereas the top three rows show higher temperatures, taken from RH1. As can be seen, the Γ modes all broadened at higher temperature, but the Σ modes do not, at least until a temperature of 785 ºC. Also at higher temperature the Σ spectra no longer exhibit the β-phase peak. (b) Before and after comparison of the Raman spectra of the Γ modes from experiment RH1, taken at the same pressure. Specifically the red curve is before and the orange curve is after. As can be seen the intensity of the Γ modes decreased by more than 50%, where the intensity of the Γ_3 mode decreased the most. Such loss in intensity of the CH modes implies that CH bonds were broken during the experiment.

Figure 23b attempts to show loss of CH bonds during the experiment RH1, which is evidence of partial decomposition. Specifically the red curve shows the Γ modes before heating and the orange curve shows the Γ modes after heating. As can be seen the intensity of the Γ modes decreased more than 50%, with the difference in the Γ_3 intensities being the greatest. The loss in the Γ intensity implies the loss of CH bonds during the high-temperature part of RH1.

The loss of CH bonds could be due to dehydrogenation. This is supported by experiment RH7 in which liquid H_2 escaped from the SC after the cell was opened following the experiment. Intuitively, partial dehydrogenation would cause the observed blue-shift in the peak positions of all Raman active modes by releasing strain on the remaining bonds, assuming the hydrogen was allowed to diffuse away.

Another important observation made after RH1 (Figure 18) was that NDs (of size 2-10 nm) and OLC (of size 20-50 nm) were found in the reaction products using HRTEM analysis. This is further evidence of dehydrogenation, but more importantly is proof that diamond can grow under conditions where adamantane is mostly stable.

Thus the HPHT experiments on adamantane reveals that the dehydrogenation of adamantane occurs around 30 GPa starting between 560 and 700 C and continuing up until the highest temperature of 790 C, and also gives more concrete evidence that the adamantane is not completely dissociating, but rather that the dehydrogenation is followed by the radical-like adamantane bonding to form ND and OLC. Hence, to grow ND from a seeding technique will require a hydrocarbon which cracks before the measured dehydrogenation HPHT conditions of adamantane. Such cracking may then lead to a seeding process if the adamantane dehydrogenates after the cracking, or the created carbon radicals dehydrogenate the diamondoid seeds. To study this possibility the carbon radical source was chosen as paraffin wax.

5.3 The Diamondoid Seeding Experiments and Oven Heating

The above furnace-heating experiments of adamantane revealed a HPHT region where adamantane will dehydrognate and form ND. It also showed that the dehydrogenation does not cause complete dissociation of the adamantane. Therefore it is plausible that a single adamantane (or diamondoid) molecule will form ND when immersed in a sample of carbon radicals under similar high pressure and high temperature conditions. To test this hypothesis HPHT experiments were next conducted on samples of diamondoid seeds diluted in paraffin wax (and other easily cracked organic compounds).

Is should be noted that these new experiments were conducted using oven heating instead of furnace heating since this gives a more accurate measure of temperatue and better uniformity, as mentioned previously. To relate the temperature measurements of the diamondoid-seeded experiments to the adamantane-only experiments, one additional experiment was conducted. This involved repeating an adamante-only experiment using oven (instead of a furnace) heating. Although this experiment is not described in this thesis the result was that the furnace experiments over-estimated temperature by about 150 C. Specifically, in the furnace heating experiment RH1 (Figure 18) the adamantane partial decomposition started in the range of 560-700 C and continued up to 790 C. However in the oven heating version of this experiment, partial decomposition started in the range of 410-510 C and continued up to 660 C.

For the above reason all seeding experiments were done at temperatures less than 660 C. The first experiment tested weather the seeding process is possible using paraffin wax as the carbon matrix and adamantane as the seed (experiment 1). The second experiment tested if AZADO may be substituted for the diamondoid seed and if it will facilitate the growth of NV^- centers (experiment 2). Experiment 3 incorporated a Phosporhus containing molecule (Tricyclohexylphosphine ($P(Cy)_3$), into the Paraffin/AZADO charge to test weather the grown ND will become n-doped, hopefully aiding in the stability of NV^-. And experiment 4 used only Paraffin wax as a base line for the seeding experiments. This is the most important paraffin experiment because it will show that no ND were formed without seeding.

One goal of these experiments is to determine how the ND size, quality, defect and doping concentrations can be manipulated. The experimental parameters to manipulate are: initial concentrations of seed and dopants, the HPHT growth conditions including annealing time, the carbon radical source and air oxidation time after growth.

After growth, some of the samples were annealed inside an oven to ~ 530 ^oC in air to test wheather PL associated with NV^- would emerge due to the etching of sp^2 surface carbon and H-termination on the surface.

5.3.1 Materials and Methods

The samples were created by melting paraffin wax between 100-150 ºC and subsequently adding diamondoid seeds and dopant chemicals. The various constituients and their masses added into the paraffin wax, initial (P_o) and final (P_f) pressures and the final temperatures (T_f) of the experiments are given in Table 5.

Table 5 Chemicals, mass of reactants, and initial and final HPHT parameters used in the ND seeding growth experiments.

Exp	Paraffin (g)	Adamantane (g)	AZADO (g)	$P(Cy)_3$ (g)	P_o/P_f (GPa)	T_f(ºC)
1	5	1	-	-	28.4/11.7	580
2	1.4	-	.032	-	31/10	510
3	1.4		.032	.05	30.2/7.7	580
4	1	-	-	-	31/14	550

The samples were placed into a 100 µm diameter ~20 µm deep cylindrical SC, laser cut into an Inconel gasket of 20 GPa pre-indentation pressure. The DAC and furnace were purchased from D'Anvils (Piston-Cylinder mighty miniDAC and DAC heater, Figure 12a, right, and Figure 12b, respectively). The temperature was monitered inside the oven using a therocouple in contact with the DAC, and the pressure was measured using the standard Ruby PL method[18]. During all HPHT growths the pressure dropped considerably (~30 to 10 GPa or lower) as the temperatutre increased implying a change in the composition of the initial sample. Due to the small concentration of the seeding and doping chemicals with respect to the paraffin wax the *in situ* Raman spectra for all experiments only reveal the CH peaks associated with the paraffin around 3000 cm^{-1}.

5.3.2 Results

The initial Raman spectra obtained during experiment 1 at the various growth temperatures and pressures are given in Figure 24. The first-order diamond anvil Raman peak has been omitted for clarity. During HPHT the sample began to change as is evident from the pictures taken *in situ* as shown in the insets in Figure 24.

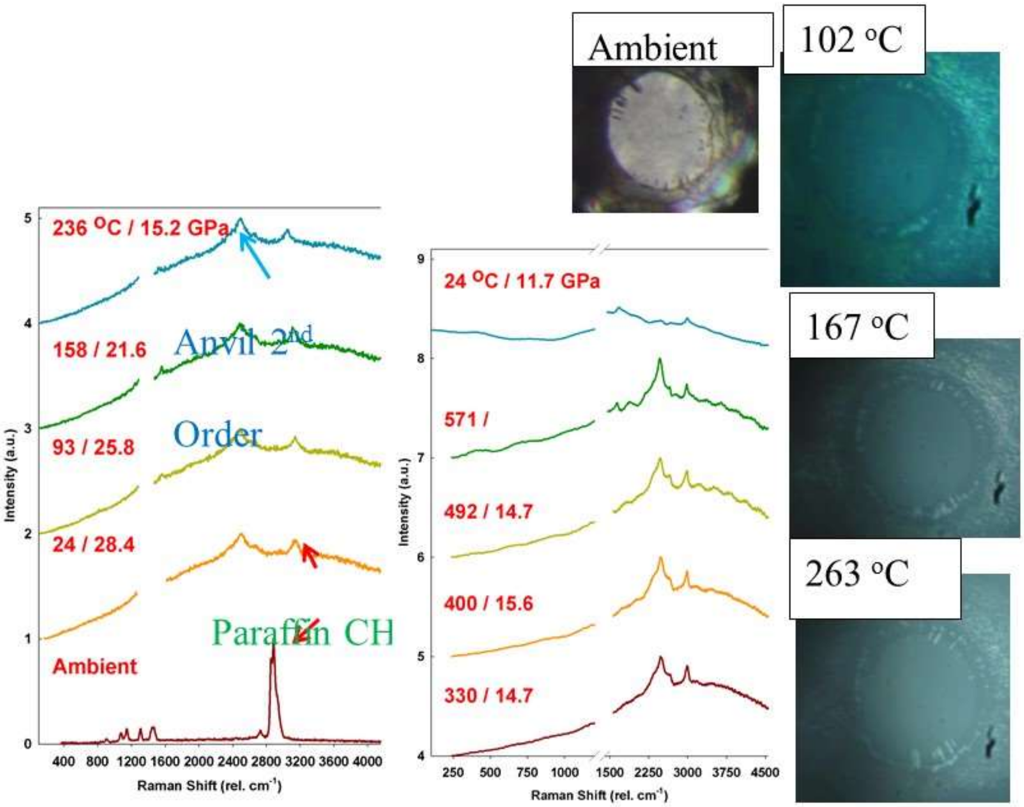

Figure 24. Raman spectra and pictures of the sample during HPHT for experiment 1. These are similar to those observed for all HPHT seeding experiments. Pressure and temperature are as indicated. The red arrow points to the only visible peaks from the paraffin wax that could be observed inside the DAC. As the temperature increases the pressure inside the SC decreases considerably, again observed in all experiments. The top spectrum on the right was obtained at ambient temperature, after the HPHT experiment, but still at high pressure. The insets give pictures of the sample at various growth temperatures and pressures. The needle-like substance growing from the edge of the gasket into the SC is most likely graphite or diamond whose growth was catalyzed by the Inconel gasket[60]. The Raman spectrum for this material is in Figure 30.

Concurently, as the temperature is increased an opaque (needle-like) substance began to grow from the side of the gasket, the Raman spectra of this substance at ambient conditions (to be presented later) show graphitic D and G peaks[59]. Accompanying this graphitic needle growth is the drastic decrease in pressure mentioned previously. The needle growth from the side of the gasket is most likely due to diamond/graphite formation catalyzed by carbide formation in the gasket material[60].

After HPHT growth the sample was molded into the shape of the SC (Figure 25b), making it easier to remove onto a Si or quartz substrate. Figure 25a gives the Raman spectra of the initial sample and the final product for experiment 1, as well as the substrate (Si) spectrum (background), for reference. Most spectra of the final product exhibited graphitic D and G peaks (~1360 and 1600 rel. cm^{-1}, respectively)[59].

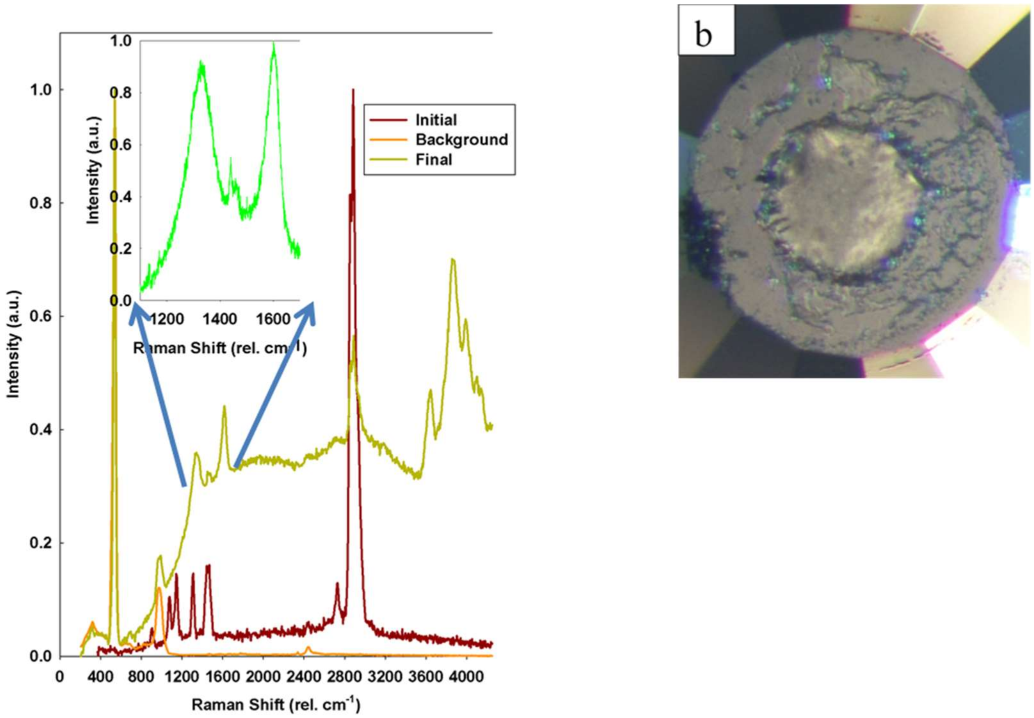

Figure 25 (a) Raman spectra of the sample before (red) and after (green) the HPHT treatment in experiment 1, as well as the background of the Si wafer used as the substrate (orange). The inset is a magnification of the D- and G-bands from the sample after growth. (b) The sample after the HPHT growth, but still on the diamond anvil. As can be seen it is molded in the shape of the SC and "sandy" in texture. The only experiment which did not exhibit this behavior is experiment 3.

In experiment 2 adamantane was substituted with the diamondoid derivative AZADO in an attempt to create NV color centers. Figure 26compares the Raman spectra from experiments 1 and 2. As seen, there are similarities and differences between the adamantane and AZADO growth products. Both spectra have the D and G-band Raman peaks, which are indicative of disordered carbon and graphite, respectively. However, the D-band can also be associated with single digit H-terminated ND[61]. Only the experiment with AZADO exhibits photoluminescence (PL), which originally was thought to include fluorescence from NV^- centers within nanodiamond[62]. Figure 26(b) is the spectra from the AZADO experiment taken with two different excitation wavelengths to determine if the broad spectrum in Figure 26a centered around 640 nm is associated with PL or Raman. As seen the Raman shifts are different using different excitation wavelengths, which identifies the emission as PL.

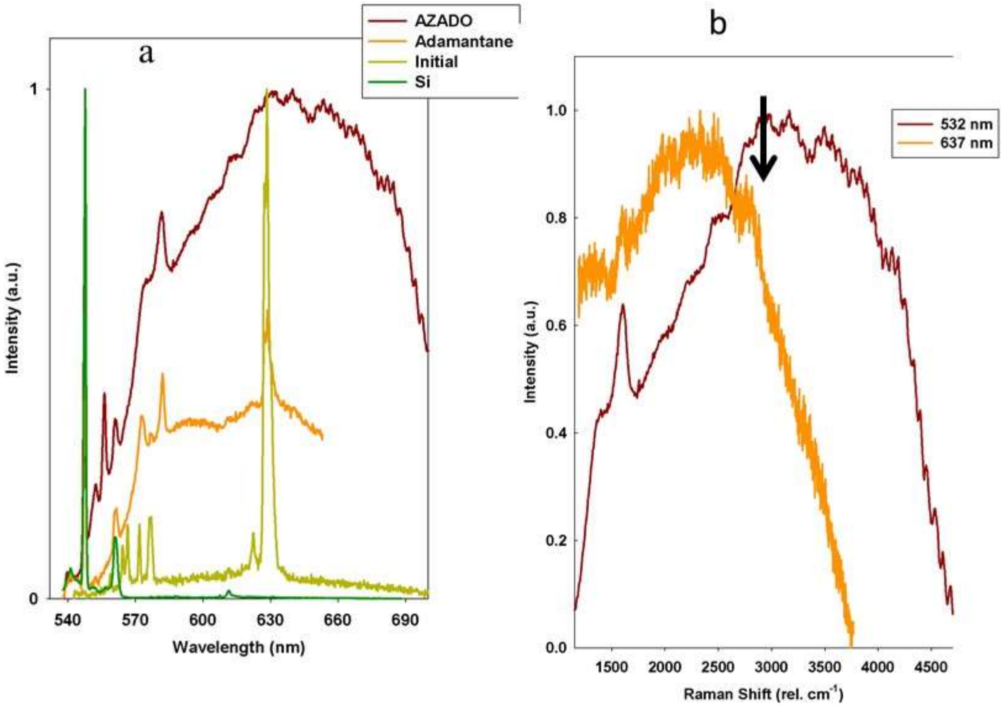

Figure 26. Raman spectra from experiments 1 and 2 after the HPHT. (a) Comparison between the initial Paraffin wax Raman spectrum (light green), and the spectra from the final products of the adamantane and AZADO experiments (orange and dark red, respectively). The Si substrate background is the dark green spectrum. (b) Spectra of the sample from the AZADO experiment taken with two different excitation wavelengths (532 and 637 nm). The black arrow points to the graphitic G-peak which is visible for both excitation wavelengths. From this data it can be concluded that the broad emission seen in the product of the AZADO experiment is PL. No such PL was seen in the product of the adamantane seeding experiment.

As mentioned above, an attempt was made to dope the diamond with phosphorous (P) (and nitrogen) in experiment 3. The Raman and PL spectra for this P-doping experiment (3) are shown in Figure 27. Figure 27a,b,c show spectra from different locations (A,B,C, respectively in the leftmost picture) of the sample from experiment 3 during an anneal in reducing atmosphere. Unlike experiments 1 and 2 there was initially a liquid in the final product for experiment 3 implying the P (Cy) $_3$ dopant decomposed into a liquid.

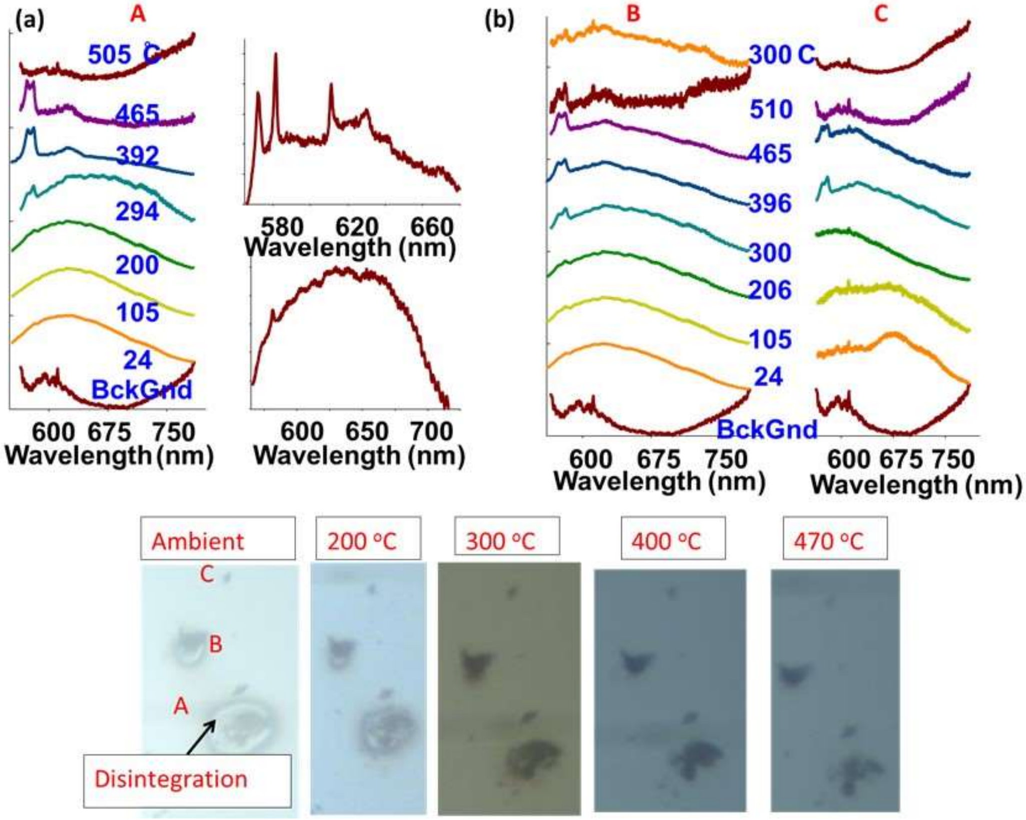

Figure 27 Images and Raman spectra for the high-temperature ArH$_2$ anneal of the NDs created with P-doping (experiment 3). The Raman spectra are given as the temperature is increased for the samples A, B and C depicted in the left-most picture labeled "Ambient". (a) Shows the Raman spectra of the sample at location A during anneal. (b) Shows the Raman spectra of the sample at location B during anneal. (c) Shows the Raman spectra of the sample at location C during anneal. The insets in (a) are other Raman spectra of the products from experiment 3 in regions that are not labeled in the left-most picture. The top inset shows a pristine ND Raman peak at 1328 cm^{-1}, and the bottom inset shows a spectrum with ND and PL peaks. The arrow in the picture labeled "Ambient" points to photo-disintegration from 532 nm excitation laser of the sample before the annealing. This photo-disintegration of the sample occurred for all experiments except 4. The remaining pictures show the changes that occur during anneal.

The pictures given in Figure 27 show what happens to the product of experiment 3 during anneal to increasing temperatures in a reducing atmosphere. As seen the liquid-like product evaporates leaving behind a solid product. The PL in Figure 27(a,b) matches that of USND[63]. It should be noted that the PL in (a) and (b) are more intense than that from the experiments without the P-doping (i.e. the D and G peaks are not visible for (a) and (b) before anneal).

It is also important to note that the 532 nm laser used for the Raman spectroscopy photo-damages the samples. This is visible in the left-most picture (labeled "Ambient") in Figure 27 as the outlines indicated by the arrow.

As can be seen from Figure 27 increasing the annealing temperature to 300 ^{o}C has the effect of making the graphitic D- and G-band Raman intensities more pronounced relative to the PL. As the temperature is further increased from 400-500 ^{o}C the D-band intensity begins to increase relative to the G-band and surpasses it. However, above 500 ^{o}C the D and G band signals were almost completely lost possibly because of the sample being etched.

The PL in Figure 27a changed at relatively low annealing temperatures, between 200-300 ^{o}C. Specifically, the center of the broad PL shifted from about 625 nm to 670 nm, and subsequently vanished around 400 ^{o}C. The shifting and disappearance of the PL might be a consequence of the organic residue decomposing.

The sample from experiment 3 showed very different PL and Raman spectra depending on anneal conditions. Figure 28a shows the spectra during an anneal in an ArH_2 environment (98% Ar, 2% H_2) and Figure 28c shows the spectra during an air-anneal. As can be seen the D and G peaks rapidly lose amplitude as the temperature increases in the air anneal case, compared to anneal in an ArH_2 environment. This is to be expected as graphite and amorphous carbon are known to etch in air at these temperatures. In contrast for the ArH_2-annealing environment, Figure 28a, the graphitic D and G peaks not only became more pronounced around 300 ºC, but did not vanish at the highest temperature of 520 ºC. This implies that the mechanism responsible for the loss of the Raman signal in Figure 27 is air oxidation.

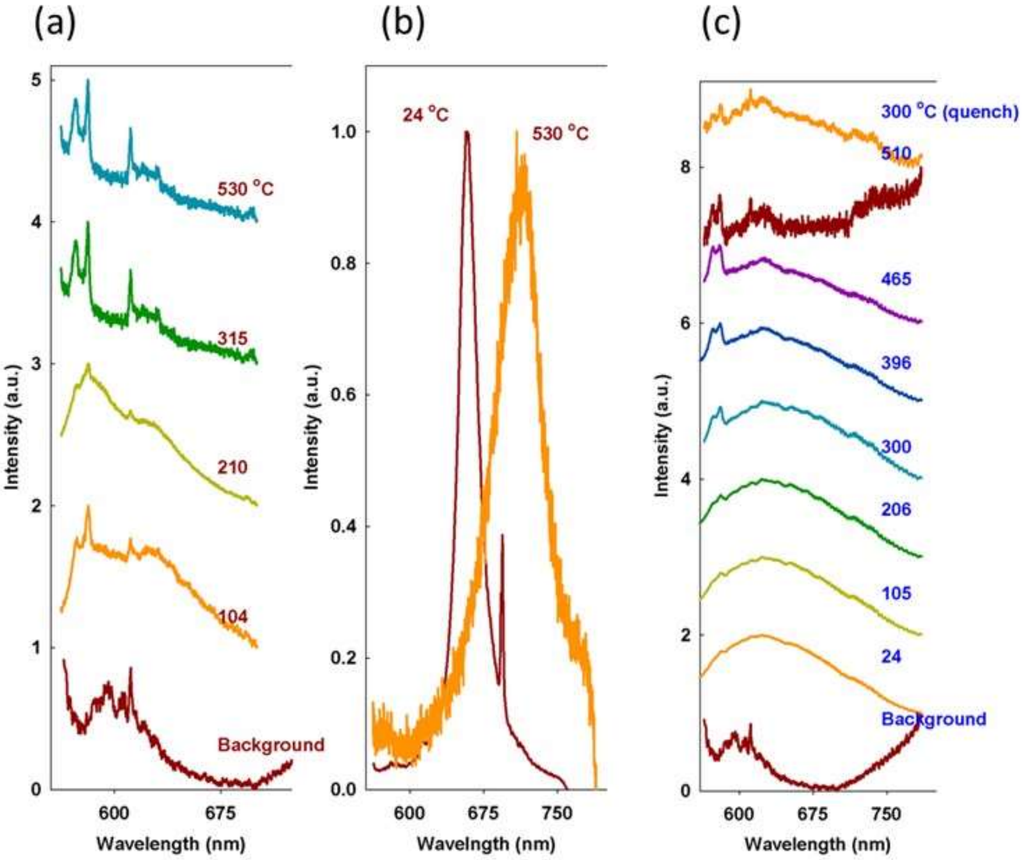

Figure 28. Raman and PL data from a high temperature anneal on the sample from experiment 3. (a) The anneal takes place inside an ArH$_2$ environment, (b) PL exhibited after anneal to 530 ºC in an ArH$_2$ environment followed by exposure to air for 10 minutes. The spectra were taken as the sample was allowed to cool where the temperatures are as indicated. (c) The anneal takes place is inside an air environment.

The ratio of D and G-band intensities can be used to estimate crystal size. For the equal D and G-band intensities, occurring around 400 ºC in Figure 28c, in-plane crystallite size of graphite, L$_a$, is approximately 20 nm[64].

Air oxidation of sp^2 carbon on 5-8 nm detonation ND has been studied previously[65],[66]. In the annealing experiment [66] the temperature at which the sp^2 surface content began to oxidize, which may be deduced from the increase in the intensity ratio of the D to G bands, was lower than measured in this experiment. However the detonation ND used in [66] contained metal impurities, with Fe in the highest concentration which acts as a catalyst for oxidation of sp^2. Therefore the higher oxidation temperature is most likely due to the lack of metal impurities within the seeded ND, which also implies that the ND measured in experiments 1-3 are not a consequence of the Inconel/Carbon solution mentioned in[60].

Something interesting is observed in the case when air was only to react with the product from experiment 3 for a short time. Specifically the sample was first annealed to 530 C in ArH_2 but then air was allowed into the chamber for about 10 minutes. During this brief time the D and G peaks vanished and instead a bright PL appeared, as shown in Figure 28b, centered at 750 nm at 530 ^oC. And as the oven cooled down the peak position of the new PL blue shifted and narrowed, and finally remained centered around 655 nm at room temperature. The large difference in PL for short time exposure to air at high temperature compared to long exposure can be attributed to the ND being etched by air oxidation, which has been measured to have an etch rate of 10nm/hr at 600 ^oC[65].

As mentioned earlier, it order to show that the diamond-like seed molecules are in fact seeding ND growth it is necessary to show that diamonds do not grow under identical conditions when the seeds are absent. To test this, experiment 4 was conducted with pure paraffin. Pictures of the samples extracted from experiment 4 are given in Figure 29. The Raman spectra were entirely of the initial Paraffin matrix ((a) and (b)) with the exception of one large crystal ((c) and (d)). The majority of the extracted sample (the paraffin) evaporated off of the quartz cover glass substrate after an air-anneal at ~ 300 °C (Figure 29b-d).

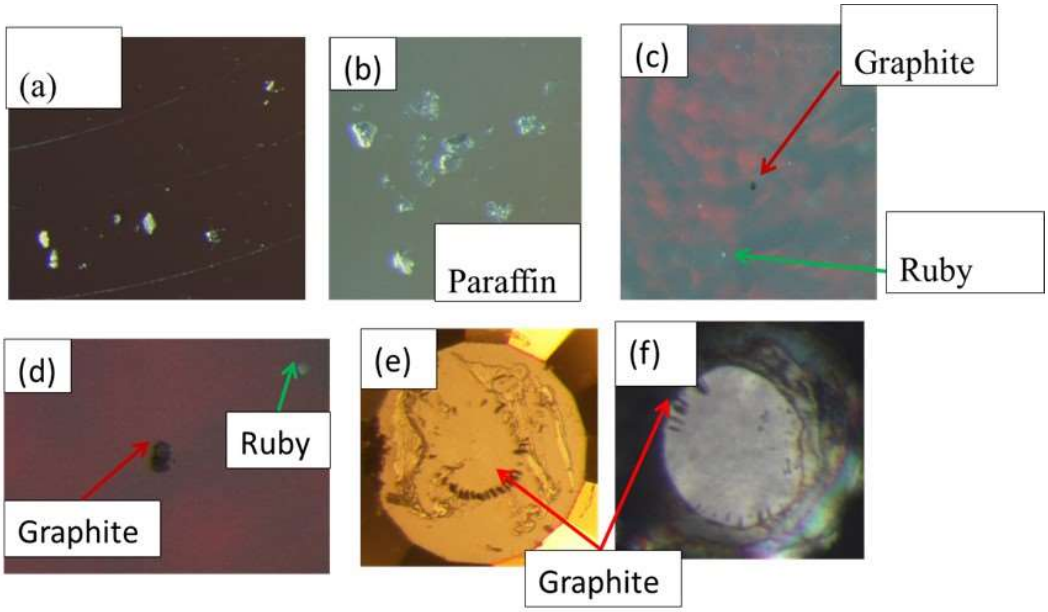

Figure 29 Images from a pure Paraffin HPHT experiment (4). (a) Photo of sample from experiment 3 and placed on a Si substrate. This will serve as a reference for the samples extracted from experiment 4. (b), (c) and (d) shows the sample from experiment 4 on a quartz cover glass before (b) and after (c and d) an air aneal. (d) is a magnification of the only region of the sample from experiment 4 to give a diampnd/graphite Raman signal. (e) and (f) are images of the graphite/diamond needles produced by a catalyzation by the Inconel gasket. (e) The photo shows product still stuck to the anvil after experiment 4. (f) The photo shows graphitic needles growing from the gasket during HPHT. This is most likely the source of the large particle which gave the only diamond/graphite Raman peaks in expeirment 4.

As already mentioned, the "graphite" crystal depicted in Figure 29d has a diamond/graphite Raman spectrum. This is seen in Figure 30(top). It is believed that the mechanism for growth is the same as mentioned in[60]. The remaining pieces seen in Figure 28(c) after the anneal are ruby.

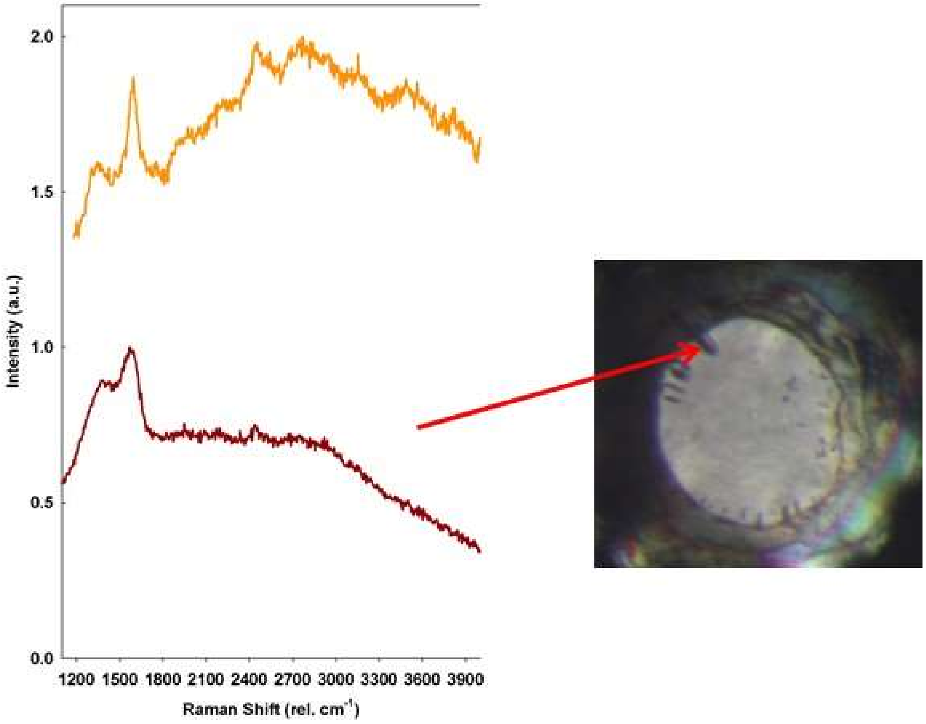

Figure 30 Raman spectrum of the needle on gasket edge (bottom), and the black graphite/diamond crystal (top plot) from experiment 4 after a 400 ºC anneal. The method of diamond/graphite needle growth is thought to be due to the same mechanism as mentioned in[60].

Here it should be noted that it is unlikely that that the diamond/graphite Raman spectra observed in the products from experiments 1-3 (Figure 26, Figure 27, Figure 28) come from the Inconel/Carbon catalyzed needles because they come from product regions that appear white in color (Figure 29a).

5.3.3 Conclusions

Around 100 - 300ºC and 30 GPa the paraffin wax undergoes a chemical reaction in which the pressure begins to decrease with increasing temperature until reaching a value of about 10 GPa for all experiments. However, the lowest final pressure measured is for the experiment with P-doping (7.7 GPa), and the highest final pressure was measured for the pure paraffin experiment (14 GPa)[5]. Accompanying this reaction is the growth of a needle-like graphite/diamond-like substance from the gasket edge. When the pressure has dropped to a low enough value the needle growth stops, and the pressure stabilizes.

The mechanism for the graphite/diamond needle growth from Inconel is predicted in [60] to be due to the Inconel acting as a Carbon getter, creating different Inconel Carbides until the carbon stoichiometric coefficient obtains the highest possible value. Then the carbon will be ejected from the Inconel. The end product will then depend on the pressure and temperature inside the SC with respect to the diamond/graphite stability curve. It is therefore possible that the loss in pressure signifies the decomposition of the paraffin wax into carbon radicals, which is lower than the temperature required to dissociate Adamantane as deduced from the experiments in Chapter 5.1. These radicals then enter into the Inconel gasket to form carbides and subsequently form diamond/graphite around the edges.

When the paraffin is doped with either Adamantane or AZADO the final product is diamond or graphite as deduced from the Raman spectra. The PL is seen in the AZADO seeding experiment, but not in the Adamantane seeding experiment. High-temperature air-anneal etches the diamond/graphite product, whereas a high-temperature ArH_2 anneal

---

[5] **The temperature for the P-doping experiment was 550 °C and the final temperature for the pure paraffin experiment was 580 °C,**

Table **5**.

does not. And the sample from experiment 4 contains nothing but paraffin and one piece of diamond/graphite which most likely comes from the gasket due to its size, color and the fact that it did not etch away when annealed to 550 ºC (whereas ND from experiment 1-3 did etch away completely).

CHAPTER VI

CONCLUSIONS

Aspects of the ND growth dynamics are given pictorially in Figure 31. The photographs are of Paraffin wax/Adamantaylamine mixtures after extraction from the DAC while the sample is still on the diamond anvil. The temperatures labels correspond to the maximum temperature reached during HPHT growth. As can be seen, increasing the final temperature changes the opacity and color of the final product. It is thought that the opaqueness is a consequence of graphite and/or disordered carbon either growing on the ND surface or self-nucleating. The lowest temperature runs (< ~ 530 ºC) are typically transparent but also contain more organic residue which easily burns or dissociates when excited with the 532nm Raman pump laser spot. This is predicted to be the result growth times too short to crack a majority of the hydrocarbon sample or for the carbon radicals to bond to the adamantylamine seed.

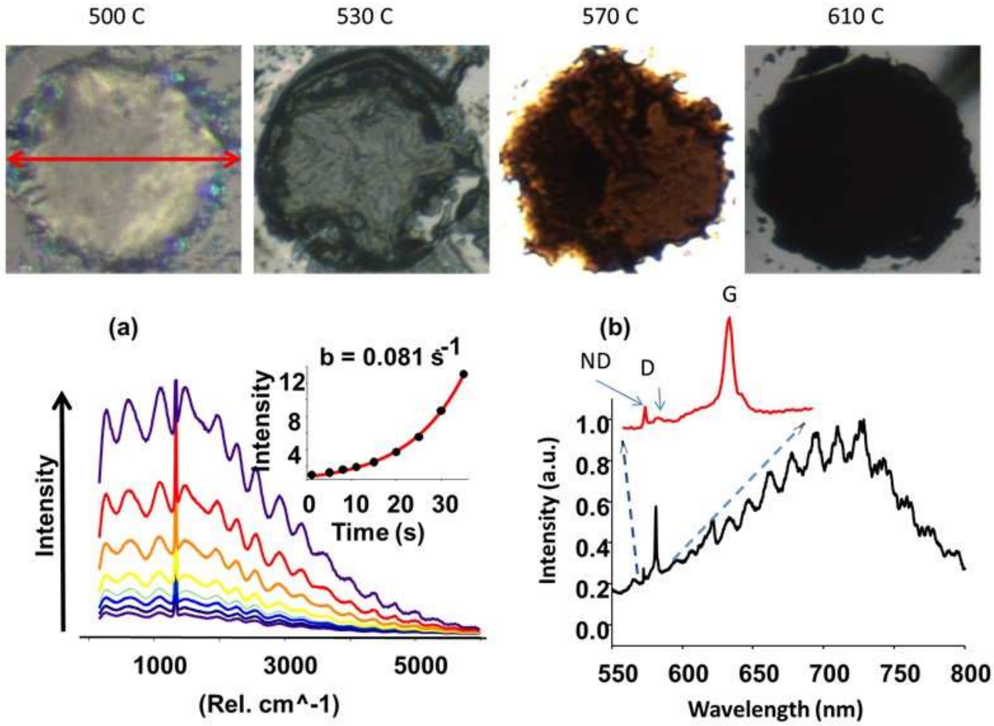

Figure 31 Images of different samples after HPHT at different temperatures and PL and Raman data during and after growth. The top pictures are from the sample after HPHT on the diamond anvils before extraction, the maximum growth temperature labels each picture. As the maximum temperature increases the opacity (and hence the disordered Carbon content) increases. (a) Around 570 °C the in-situ spectrum begins to broaden and increase in intensity. Inset shows the intensity increase is exponential with time. After some time the strong luminescence dies down and eventually ends with only a graphitic G-peak visible. (b) Spectrum from the product of a multi-anvil growth after anneal in air at 500 C for 30-40 minutes. The broad spectrum centered near 700 nm could be due to NV. Inset shows an enlarged scan of the D and G peak region in which resolved ND and amorphous carbon peaks are visible.

Figure 31a depicts *in situ* spectra during what is believed to be both self-nucleation of the cracked hydrocarbons into amorphous carbon, and seeding of the hydrocarbons to form ND. The spectra are very broad and the intensity grows as temperature (and time) increases. The inset plots the intensity of the spectra as a function of time for an experiment where the intensity grew exponentially with a time constant of about 0.081 s^{-1}. Since this broad luminescence does not appear at temperatures lower than 550 °C, whereas ND are still found at lower temperatures, it is believed that this luminescence is a consequence of "rapid-cracking" and consequently re-bonding (either self-nucleation or seeding).

The reason it is believed that the amorphous carbon is both grown by self-nucleation and growing on the surface of the ND is given in Figure 31b. This is spectra taken from an experiment where the maximum temperature was around 560 °C. The broad PL centered around 700 nm is believed to be from NV phonon side-bands, whereas the three Raman peaks (expanded in the inset), are the 1st order ND peak ("ND"), disordered carbon ("D") and the graphite peak ("G"). Hence the ND likely has disordered carbon and graphite on the surface. The fact that the NV PL is visible implies that the ND was grown from the seeding technique because the seed molecule has a Nitrogen atom. It should be noted that the NV PL and ND Raman peak could not be measured when the product was first extracted from the multi-anvil, but required an air anneal at 550 °C for 30 minutes to become visible. Pure amorphous carbon was also seen from this growth run, but it mostly burned off after the 550 °C air anneal.

Figure 32 gives PL data from NDs before any air-anneal showing some of the consequences of amorphous and graphitic surface carbon. Figure 32a gives the typical PL spectra associated with NV encased within a ND with amorphous and graphitic surface carbon. Such spectra have been seen at both high-temperature (> 550 °C) and low-temperature (< 530 ºC) growth temperatures (refer to Figure 26a). Figure 32(b) is a PL spectra associated with amorphous and graphitic surface carbon on a ND without NV fluorescence. It is obtained from a different region of the same sample. And Figure 32(c) gives the result when the spectrum associated with surface contamination on ND (orange curve copied from (a)) is subtracted from the spectrum containing an “impure” ND with NV fluorescence (red curve copied from (b)). The resulting spectrum (yellow curve) gives possible evidence of NV fluorescence. The confocal scan in Figure 32(d) is from the region where the spectra from (a) and (b) were taken.

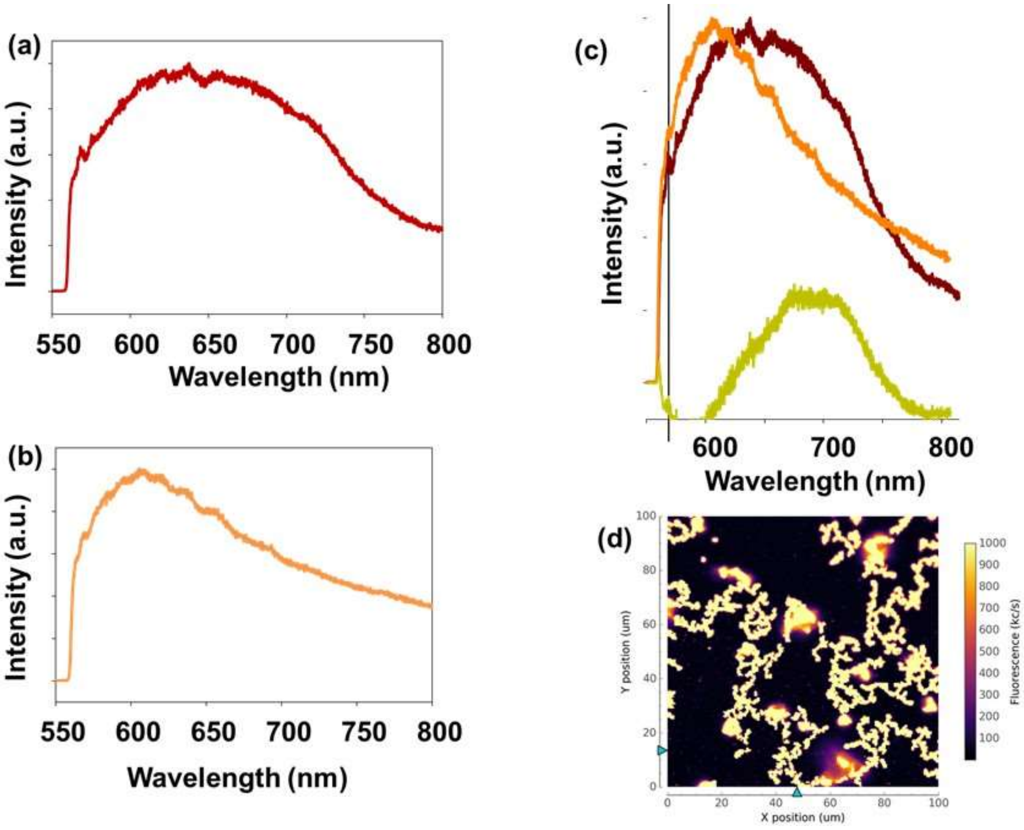

Figure 32. PL data and confocal scan of HPHT seeded NDs before air anneal. (a) PL spectra from a multi-anvil growth considered to be representative of ND with NV and background fluorescence generated by amorphous and graphitic surface carbon. (b) Typical spectra from a different region of the same growth product. The spectrum here is attributed to ND with amorphous C and graphitic surface carbon, but no NV. (c) Subtraction of Pl spectra of (b) from PL spectra from (a). The yellow curve gives possible evidence of NV PL. (d) Typical confocal scan from HPHT seeded NDs.

There are two main conclusions from the presented data. The first is that the seeding technique is working. Proof of this conclusion is given by the fact that the NV and ND Raman spectra are measured from HPHT experiments way below the temperature threshold for ND creation by the decomposition of organics [46]. The second conclusion is that despite the temperature regimes investigated, amorphous or graphitic surface carbon seems to always be present on the seeded HPHT NDs. This surface carbon represents a problem in that it complicates ODMR measurements of the NV which are required for the high-resolution sensing protocols. However, as is evident from Figure 31(b), the surface impurities may be oxidized in air at high-temperatures. The only difficulty with the air oxidation is that the times required to etch a significant amount of the surface impurities is longer than predicted by previous ND air-anneal experiments[66].

The *in situ* and *ex situ* spectra imply a type of "phase--diagram" for the growth of HPHT organic NDs as given in Figure 33. The green curve gives the typical pressure dependence on temperature for the HPHT experiments. The plot is divided into 3 regions: Initial, Cracking and Nucleation/Growth. In the Initial region for temperatures lower than ~100 ^{o}C there is not much change in the pressure or the state of the hydrocarbon source. The typical Raman spectra for paraffin wax at high-pressure and relatively low temperatures is given in Figure 33a.

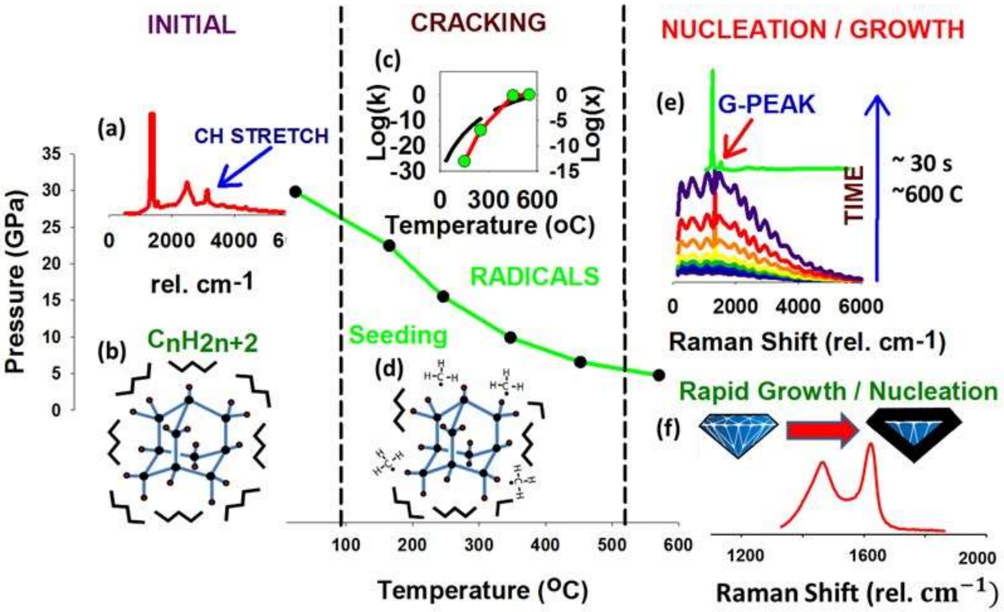

Figure 33 Hypothetical phase diagram for the creation of HPHT seeded NDs. The Green curve gives the typical dependence of pressure inside the DAC as a function of temperature. (a) Typical Raman spectrum of paraffin at ambient temperatures and high-pressures, the CH stretch is marked for paraffin wax. (b) Pictorial representation of an organic ND seed (adamantane) surrounded by a hydrocarbon source at ambient temperatures. (c) In the medium-temperature regime (~100 – 500 ^{o}C) typical hydrocarbons such as paraffin wax begin to crack. The left axis (black curve) and right axis (red curve) gives the rate of cracking and the amount of material cracked (for the measured exponential temperature rise observed in DAC experiments) as a function of temperature for paraffin wax at pressures around 6 MPa. (d) Pictorial representation of the ND seed surrounded by the hydrocarbon source partially cracked into methyl radicals. (e) Around 550 – 600 ^{o}C rapid growth of both seeded ND and amorphous carbon begins to take place. This is predicted due to the broad PL which gains intensity with time. The top curve (green) gives the final *in situ* Raman spectra for HPHT growth after all the cracked hydrocarbons have been converted. The graphitic G-peak is labeled. The D-peak is obscured from the DAC Raman peak. (e) Pictorial representation of the growth of amorphous and graphitic surface carbon on the NDs in this high-temperature region. The Raman spectrum was taken from a sample extracted from the DAC revealing the disordered graphite and graphite Raman peaks.

The "mid-temperature" region is labeled "cracking". In this region the pressure begin to decrease substantially. It is believed that the pressure drop is associated with the cracking of the hydrocarbon, which subsequently form the radicals required for the seeded growth. Figure 33(c) gives a plot of the cracking rate of paraffin wax as a function of temperature, and the total amount of cracked paraffin wax using the reaction rate parameters calculated from[67]. Prior paraffin cracking experiments [reference] were done at ~6 MPa, which are much lower than those used for the seeded growth experiments. However, the temperatures are very similar, and it is thought that there is not a strong dependence of hydrocarbon cracking on pressure at the temperatures considered. It is also thought that in this temperature/pressure region seeding might begin but at a very low rate of bonding.

The final region, "Nucleation/Growth", is associated with temperatures around 530 °C and higher. Here the pressure tends to stabilize around 8 GPa implying that the cracking process has finished. When the temperature increases above ~560 °C the broad PL begin to be measured, the evolution of which is depicted in Figure 33(e). It is predicted that in this region the growth rate begins to increase substantially, and that if the temperature is too high then not only will the radicals bond to the seed but will also self-nucleate as described in[15]. It is also predicted that in this region the amorphous and graphitic carbon will grow on the surface of the ND, as depicted pictorially and with a typical *ex situ* Raman spectra of amorphous carbon.

In conclusion because NDs with NV centers do form at temperatures and pressures below the seed decomposition conditions, and also well below the temperatures needed for ND formation from decomposed hydrocarbons, it is concluded that the NDs are likely being created by the seeding technique. The key test of this hypothesis comes from the lack of ND formation in the paraffin-only growth where no seed molecules were present.

Some questions about the growth dynamics which still need to be answered are in regard to the yield of the NDs by the seeding technique, whether lower temperatures (< 500 °C) may result in higher purity NDs (i.e. less surface contamination) and how the size of the seed impacts the ND (i.e. what are the consequences of using diamantane or triamantane for the seeding technique).

WORKS CITED

[1] V. A. Davydov, A. V. Rakhmanina, S. G. Lyapin, I. D. Ilichev, K. N. Boldyrev, A. A. Shiryaev and V. N. Agafonov, "Production of nano- and microdiamonds with Si-V and N-V luminescent centers at high pressures in systems based on mixtures of fluorocarbon compounds," *JETP Letters,* vol. 99, no. 10, pp. 585-589, 2014.

[2] S. Hong, "Nanoscale magnetometry with NV centers in diamond," *MRS Bulletin,* pp. 155-161, 2013.

[3] J. R. Maze, "Nanoscale magnetic sensing with an individual electronic spin in diamond," *Nature Letters,* pp. 644-648, 2008.

[4] e. a. P. Neumann, "High-precision nanoscale temperature sensing using single defects in diamond," *Nano Letters,* pp. 2738-2742, 2013.

[5] L. Shang, "Engineered nanoparticles interacting with cells: size matters," *Journal of Nanobiotechnology,* vol. 12, no. 5, 2014.

[6] e. a. C. Bradac, "Observation and control of blinking nitrogen-vacancy centres in discrete nanodiamonds," *Nature Nanotechnology Letters,* vol. 5, May 2010.

[7] e. a. Vadym N. Mochalin, "The properties and applications of nanodiamonds," *Nature Nanotechnology,* vol. 7, January 2012.

[8] J. R. H. Wentorf, "The behavior of some carbonaceous materials at vry high pressures and temperatures," *The Journal of Physical Chemistry,* pp. 3063-3069, 1965.

[9] e. a. V. A. Davydov, "Nanosized carbon forms in the process of pressure-temperature-induced transformations of hydrocarbons," *Carbon,* vol. 44, pp. 2015-2020, 2006.

[10] e. a. V. A. Davydov, "Production of nano- and microdiamonds with Si-V and N-V luminescent centers at high pressures in systems based on mixtures of fluorocarbon compounds," *JETP Letters,* vol. 99, no. 10, pp. 585-589, 2014.

[11] L. Fang, "A novel technique for the synthesis of nanodiamond powder," *Journal of Nanomaterials,* p. 201845, 2013.

[12] D. J. Dunstan, "Theory of the gasket in diamond anvil high-pressure cells," *Rev. Sci. Instrum.,* vol. 60, no. 12, pp. 3789-3795, 1989.

[13] P. Bridgman, The physics of high pressure, London: Bell, 1952.

[14] e. a. V Vijayakumar, "Pressure induced phase transitions and equation of state of adamantane," *Journal of Physics : Condensed Matter,* pp. 1961-1972, 2001.

[15] e. a. Sorin Bodea, "Model calculations of the temperature distribution in the laser-heated diamond cell," *Journal of Applied Physics,* vol. 65, no. 12, pp. 4688-4692, 1989.

[16] W. panero, "Temperature gradients in the laser-heated diamod anvil cell," *Journal of Geophysical Research,* vol. 106, no. B4, pp. 6493-6498, 2001.

[17] e. a. R. G. Munro, "Temperature distribution in the diamond anvil pressure cell at high temperature," *Journal of Applied Physics,* vol. 55, no. 1, pp. 4-8, 1984.

[18] M. Kaviani, P. Deak, B. Aradi, T. Frauenheim, J.-P. Chou and A. Gali, "Proper surface termination for luminescent near-surface NV centers in diamond," *NANO Letters,* vol. 14, pp. 4772-4777, 2014.

[19] A. Gali, E. Janzen, P. Deak, G. Kresse and E. Kaxiras, "Theory of spin-conserving excitation of the NV center in diamond," *Physical Review Letters,* p. 186404, 2009.

[20] J. O. Jensen, "Vibrational frequencies and structural determination of adamantane," *Spectrochemica Acta A Part A,* vol. 60, pp. 1895-1905, 2004.

[21] L. Bistricic, "A vibrational assignment of adamantane and some of its isotopomers. Emperical versus scaled semiempirical force field," *Spectrochimica Acta A Part A,* vol. 51, pp. 1643-1664, 1995.

[22] e. a. V Vijayakumar, "Pressure induced phase transitions and equation of state of adamantane," *Journal of Physics : Condensed Matter,* pp. 1961-1972, 2001.

[23] V. Vijayakumar, "Pressure induced phase transitions and equation of state of adamantane," *Journal of Physics : Condensed Matter,* vol. 13, pp. 1961-1972, 2001.

[24] J. O. H. E. A. Mason, "Short-range intermolecular forces. II. H2–H2 and H2–H," *Journal of Chemical Physics,* vol. 26, p. 756, 1957.

[25] e. a. C. G. Windsort, "Lattice dynamics of adamantane in the disordered phase," *Journal of Physics C: Solid State Physics,* vol. 11, pp. 1741-1759, 1978.

[26] M. F. J. P. Amoureux, "Comparison between structural analyses of plastic and brittle crystals," *Crystallographia B,* vol. 43, p. 470, 1987.

[27] e. a. Rekha Rao, "High pressure raman scattering studies on adamantane," *Journal of Chemical Physics,* p. 6739, 2000.

[28] e. a. R. S. Butler, "The enthalpy of formation of adamantane," *Journal of Chemical Thermodynamics,* vol. 3, pp. 277-280, 1971.

[29] A. B. Bazyleva, "Thermodynamic properties of adamantane revisited," *The Journal of Physical Chemistry B,* pp. 10064-10072, 2011.

[30] J. Loubser and J. v. Wyk, *Diamond Research,* vol. 11, 197.

[31] G. Davies and M. Hamer, "Optical studies of the 1.945 ev vibronic band in diamond," *Proceedings of the Royal Society of London A,* vol. 348, no. 1653, 1976.

[32] M. W. Doherty, N. B. Manson, P. Delaney, F. Jelezko, J. Wrachtrupe and L. C. Hollenberga, "The nitrogen-vacancy colour centre in diamond," *arXiv:1302.3288v1,* 2013.

[33] F. Maier, J. Ristein and L. Rey, "Electron affinity of plasma-hydrogenated and chemically oxidized diamond (100) surfaces," *Physical Review B,* vol. 64, p. 165411, 2001.

[34] K. J. Rietwyk, S. L. Wong, L. Cao, K. M. O'Donnell, L. Ley, A. T. S. Wee and C. I. Pakes, "Work function and electron affinity of the fluorine-terminated (100)," *Applied Physics Letters,* vol. 102, p. 091604, 2013.

[35] P. Siyushev, H. Pinto, M. Voros, A. Gali, F. Jelezko and J. Wrachtrup, "Optically controlled switching of the charge state of a single nitrogen-vacancy center," *Pysical Review Letters,* vol. 110, p. 167402, 2013.

[36] J. P. Amoureux, M. Bee and J. C. Damien, "Structure of Adamantane, C10H16, in the disordered phase," *Acta Crystallographica,* vol. B36, pp. 2633-2636, 1980.

[37] N. A. Murugan, R. S. Rao, S. Yashonath, S. Ramasesha and B. K. Godwal, "High-pressure study of Adamantane: Variable shape simulations up to 26 GPa," *Journal of Physics and Chemistry B,* vol. 109, pp. 17296-17303, 2005.

[38] J. Reiser, E. McGregor, J. Jones, R. Enick and G. Holder, "Adamantane and Diamantane; phase diagrams, solubilities, and rates of dissolution," *Fluid Phase Equilibria,* vol. 117, pp. 160-167, 1996.

[39] G. A. Mansoori, "Diamondoid molecules," *Advances in Chemical Physics,* vol. 136, pp. 207-258, 2007.

[40] S. K. Sikka and S. M. Sharma, "Close packing and pressure-induced amorphization," *Current Science,* vol. 63, no. 6, pp. 317-320, 1992.

[41] E. Katoh, H. Yamawaki, H. Fujihisa, M. Sakashita and K. Aoki, "Raman and infared studies of phase transitions in solid HBr under pressure," *Physical Review B,* vol. 59, no. 17, 1999.

[42] T. Steiner and W. Saenger, "H...H van der Waals distance in cooperative O-H...O-H...O hydrogen bonds determined from neutron difraction data," *Acta Crystallographica B,* vol. 47, pp. 1022-1023, 1991.

[43] P. Vinet, J. H. Rose, J. Ferrante and J. R. Smith, "Universal features of the equation of state of solids," *Journal of Physics: Condensed Matter,* vol. 1, pp. 1941-1963, 1989.

[44] N. Voëadlo and G. D. Price, "The Grüneisen parameter — computer calculations via lattice dynamics," *Physics of Earth and Planetary Interiors,* vol. 82, pp. 261-270, 1994.

[45] G. Mazzola, S. Yunoki and S. Sorella, "Unexpectedly high pressure for molecular dissociation in liquid hydrogen by electronic simultion," *Nature Communications,* vol. 5, no. 3487, 2014.

[46] S. Block, C. E. Weir and G. J. Piermarini, "Polymorphism in Benzene, Naphthalene, and Anthracene at high pressure," *Science,* vol. 169, pp. 586-587, 1970.

[47] F. H. Ree, "Systematics of high-pressure and high-temperature behavior of hydrocarbons," *Journal of Chemistry and Physics,* vol. 70, no. 02, pp. 974-983, 1979.

[48] E. A. Kraut and G. C. Kennedy, "New melting law at high pressures," *Physical Review,* vol. 151, no. 2, pp. 668-675, 1966.

[49] e. a. Vladimir L. Kuznetsov, "Onion-like carbon from ultra-dispersed diamond," *Chemical Physics Letters,* vol. 222, pp. 343-348, 1994.

[50] T. J. R. R. J. A. Yu-Ran Luo, Handbook of bond dissociation energies in organic compounds, CRC Press, 2002.

[51] M. T. Dove, Introduction to lattice dynamics, Cambridge University press, 1993.

[52] J. Orwa and e. al., "Diamond nanocrystals formed by direct implantation of fused silica with carbon," *Journal of Applied Physics,* vol. 90, no. 6, pp. 3007-3018, 2001.

[53] P. H. Chung, E. Perevedentseva and C. L. Cheng, "The particle size-depndent photoluminescence of nanodiamonds," *Surface Science,* vol. 601, pp. 3866-3870, 2007.

[54] M. A. Pimenta, G. Dresselhaus, M. S. Dresselhaus, L. G. cancado, A. Jorio and R. Saito, "Studying disorder in graphite-based systems by Raman spectroscopy," *Physical Chemistry Chemical Papers,* vol. 9, pp. 1276-1291, 2007.

[55] S. Osswald, "Control of sp2/sp3 carbon ratio and surface chemistry of nanodiamond powders by selective oxidation in air," *Journal of the American Chemical Society,* pp. 11635-11642, 2006.

[56] S. Bodea, "Model calculations of the temperature distribution in the laser-heated diamond cell," *Journal of Applied Physics,* vol. 65, no. 12, pp. 4688-4692, 1989.

[57] W. R. Panero, "Temperature gradients in the laser-heated diamod anvil cell," *Journal of Geophysical Research,* vol. 106, no. B4, pp. 6493-6498, 2001.

[58] D. Ugarte, "Curling and closure of graphitic netwroks under electron-beam irradiation," *Nature,* vol. 222, no. 4, pp. 707-709, 1992.

[59] M. Huth, "Focused electron beam induced deposition: A perspective," *Journal of Nanotechnology,* vol. 3, pp. 597-619, 2013.

[60] A. S. Bernard, "Self-assembly in nanodiamond agglutinates," *Journal of Materials Chemistry,* vol. 18, pp. 4038-4041, 2008.

[61] V. L. Kuznetsov, "Onion-like carbon from ultra-dispersed diamond," *Chemical Physics Letters,* vol. 222, pp. 343-348, 1994.

[62] A. Barnard, "Size dependent phase stability of carbon nanoparticles: Nanodiamond versus fullerenes," *Journal of Chemical Physics,* vol. 118, no. 11, pp. 5094-5097, 2002.

[63] Q. e. a. Jiang, "Thermodynamic phase stabilities of nanocarbon," *Carbon,* vol. 44, no. 1, pp. 79-83, 2006.

[64] J. Xiao, G. Ouyang, P. Liu, C. X. Wang and G. W. Yang, "Reversible nanodiamond-carbon onion phase transformation," *Nano Letters,* vol. 14, pp. 3645- 3652, 2014.

[65] T. A. Strobel, "Raman spectroscopic studies of hydrogen clathrate hydrates," *The Journal of Chemical Physics,* vol. 130, no. 1, p. 014506, 2009.

[66] P. Chung, "The particle size-dependent photoluminescence of nanodiamonds," *Surface Science,* pp. 3866-3870, 2007.

[67] C. Bradac, "Observation and control of blinking nitrogen-vacancy centres in discrete nanodiamonds," *Nature Nanotechnology Letters,* vol. 5, May 2010.

[68] T. Gaebel, "Size reduction of nanodiamonds via air oxidation," *Diamond and Related Materials,* vol. 21, pp. 28-32, 2012.

[69] J. Tisler, "Fluorescence and spin properties of defects in single digit nanodiamonds," *ACS Nano,* vol. 3, no. 7, pp. 1959-1965, 2009.

[70] J. Liu, M. Yu, C. Zhou and J. Zheng, "Renal clearable inorganic nanoparticles: A new frontierof bionanotechnology," *Materials Today,* vol. 16, no. 12, p. 477, 2013.

[71] C. Bradac, T. Gaebel, N. Naidoo, J. R. Rabeau and A. S. Barnard, "Prediction and measurement of the size-dependent stability of fluorescence in diamond over the entire nanoscale," *Nano Letters,* vol. 9, no. 10, pp. 3555-3564, 2009.

[72] C. Schreyvogel, V. Polyakov, R. Wunderlich, J. Meijer and C. E. Nebel, "Active charge state control of single NV centres in diamond by in-plane Al-Schottky junctions," *Scientific Reports,* 2015.

[73] J. Meijer, B. Burchard, M. Domhan, C. Wittmann and T. Gaebel, "Generation of single color centers by focused nitrogen implantation," *Applied Physics Letters,* vol. 87, p. 261909, 2005.

[74] G. Lucazeau, "Effect of pressure and temperature on Raman spectra," *Journal of Raman Spectroscopy,* vol. 34, p. 478–496, 2003.

[75] R. A. Forman, G. J. Piermarini, J. D. Barnett and S. Block, "Pressure measurement made by the utilization of Ruby sharp-line luminescence," *Science,* vol. 176, p. 284, 1972.

[76] L. Bragg, "Rate of cracking of paraffin wax," *Industrial and Engineering Chemistry,* vol. 33, no. 3, pp. 376-380, 1941.

[77] A. Lenef and S. C. Rand, "Electronic structure of the N-V center in diamond: Theory," *Physical Review B,* vol. 53, no. 20, pp. 13441-13455, 1996.

[78] L. Bistricic, G. Baranovic and K. Mlinaric-Majerski, "A vibrational study assignment of adamantane and some of its isotopomers. Empirical versus scaled semiempirical force field," *Spectrochimica Acta A,* vol. 51, pp. 1643-1664, 1995.

[79] H. Huang, E. Pierstorff, E. Osawa and D. Ho, "Active nanodiamond hydrogels for chemotherapeutic delivery," *Nano Letters,* pp. 3305-3314, 2007.

[80] A. A. Giardin and J. E. Tyding, "Diamond synthesis: Observations on the mechanism of formation," *The American Mineralogist,* vol. 47, pp. 1393-1421, 1962.

[81] A. C. Ferrari and J. Robertson, "Raman spectroscopy of amorphous, nanostructured, diamond-like carbon, and nanodiamond," *Philisophical Transactions of the Royal Society of London,* vol. 362, p. 2477–2512, 2004.

[82] Y. Akahama, "Pressure calibration of diamond anvil Raman gauge to 410 GPa," *Journal of Physics: Conderence Series,* vol. 215, p. 012195, 2010.

[83] J. M. Taylor, P. Cappellaro, L. Childress, D. B. L. Jiang2, P. R. Hemmer, A. Yacoby, R. Walsworth and M. D. Lukin, "High-sensitivity diamond magnetometer with nanoscale resolution," *Nature,* pp. 810-817, 2008.

[84] V. Davydov, A. Rakhmanina, J.-P. Boudou, A. Thorel, H. Allouchi and V. Agafonov, "Nanosized carbon forms in the process of pressure-temperature-induced transformations of hydrocarbons," *Carbon,* vol. 44, pp. 2015-2020, 2006.

[85] V. Davydov, A. Rakhmanina, V. Agafonov, B. Narymbetov, Jean-PaulBoudou and H. Szwarc, "Conversion of polycyclic aromatic hydrocarbons to graphite and diamond at high pressures," *Carbon,* vol. 42, pp. 261-269, 2005.

[86] C. Bradac, T. Gaebel, N. Naidoo, M. J. Sellars, J. Twamley, L. J. Brown, A. S. Barnard, T. Plakhotnik, A. V. Zvyagin and J. R. Rabeau, "Observation and control

of blinking nitrogen-vacancy centers in discrete nano-diamonds," *Nature Nanotechnology,* vol. 5, pp. 345-349, 2010.

[87] F. Dolde, H. Fedder, M. W. Doherty, T. Nöbauer, F. Rempp, G. Balasubramanian, T. Wolf, F. Reinhard, L. C. L. Hollenberg, F. Jelezko and J. Wrachtrup, "Electric-field sensing using single diamond spins," *Nature Physics,* pp. 459-463, 2011.

[88] R. Rao, T. Sakuntala, S. K. Deb, A. P. Roy, V. Vijaykumar, B. K. Godwal and S. K. Sikka, "High pressure raman scattering studies on adamantane," *Journal of Chemical Physics,* p. 6739, 2000.

[89] T. Gaebel, C. Bradac, J. Chen, P. Hemmer and J. Rabeau, "Size-reduction of nanodiamonds via air oxidation," *arXiv:1104.5075v1 [cond-mat.mes-hall].*

[90] A. Jayaraman, "Diamond anvil cell and high-pressure physical investigations," *Reviews of Modern Physics,* vol. 55, no. 1, 1983.

APPENDIX 1

THE NITROGEN VACANCY CENTER

Of the several color center defects in diamond the NV has been studied and utilized the most. Its photoluminescence properties make it a prime candidate for new sensing, biological and quantum computing applications. Because of these applications attempts to fabricate the NV using the seeding technique have been most prevalent. This section will review the basic properties of the NV which give the properties responsible for the possible sensing applications.

The NV in diamond is a naturally occurring defect in which a substitutional nitrogen is nearest neighbor to a carbon vacancy **(Figure 34)**. Current theory models the negatively charged NV as a 6-electron system, with an additional 2 electrons being donated possibly from substitutional N within the lattice. The 6 electrons are predicted to occupy the four dangling bonds surrounding the vacancy (labeled σ in Figure 34, and the axis of quantization lies along the line connecting the vacancy center with the substitutional nitrogen atom (labeled Z in Figure 34).

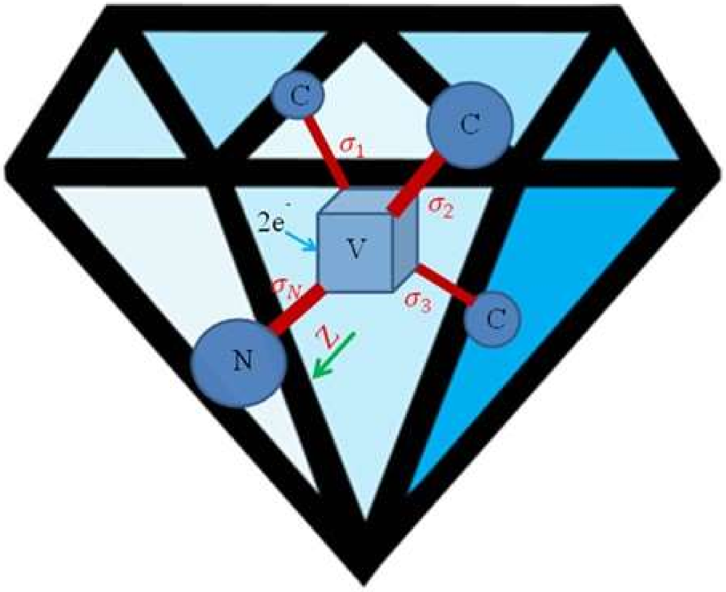

Figure 34. Illustration of the negatively charged NV. The carbon vacancy, V, is a nearest neighbor to a substitutional N atom. The center is composed of the 4 electrons associated with the dangling bonds from the 3 C atoms and substitutional N, and two extra electrons which might come from other substitutional N atom inside the diamond lattice. The axis of quantization, Z, lies along the line joining the vacancy with the substitutional N.

The NV point group symmetry is C_{3v}, Table 6, which gives rise to a unique triplet ground and excited-state; whereas typical defects in diamond have symmetries which yield singlet ground and excited states, which do not allow optically detected magnetic resonance (ODMR); a key component for sensing applications.

Table 6. Character table for the point group with the symmetry of the NV, C_{3v}. The symmetry is the same for an equilateral triangle with two 120° rotations (C_3 and C_3^2), three mirror (or reflection) planes (σ_a, σ_b σ_c), and the identity element (E).

C_{3v}	E	C_3	C_3^2	σ_a	σ_b	σ_c
A_1	1	1	1	1	1	1
A_2	1	1	1	-1	-1	-1
E	2	-1	-1	0	0	0

Using the four covalent bonds from the N and three C's to form symmetry adapted linear combinations (SALC's) group theory predicts the four basis states will transform as $2A_1 \oplus E$, and the SALCs (ignoring overlap) are given by (c.f. Figure 34 for the bond labels)

$$u = \sigma_n \tag{24}$$

$$v = \frac{\sigma_1 + \sigma_2 + \sigma_3}{\sqrt{3}} \tag{25}$$

$$e_x = \frac{2\sigma_1 - \sigma_2 - \sigma_3}{\sqrt{6}} \tag{26}$$

$$e_{y=} \frac{\sigma_2 - \sigma_3}{\sqrt{2}} \tag{27}$$

Where e_x and e_y transform as x and y in the co-ordinate system where the N is in the direction of the z-axis, and u and v transform according to the A_1 irreducible representation. To agree with experimental observations of the triplet structure of the ground and excited states the predicted configurations are $u^2v^2e^2$ and u^2ve^2 , respectively. Including spin the complete symmetry of the ground and excited states are

$^3A_2$ and ^3E. The lowest energy MO is predicted to lie within the valence band of the diamond lattice, and the higher energy v and e MOs lie within the band gap[69], Figure 35.

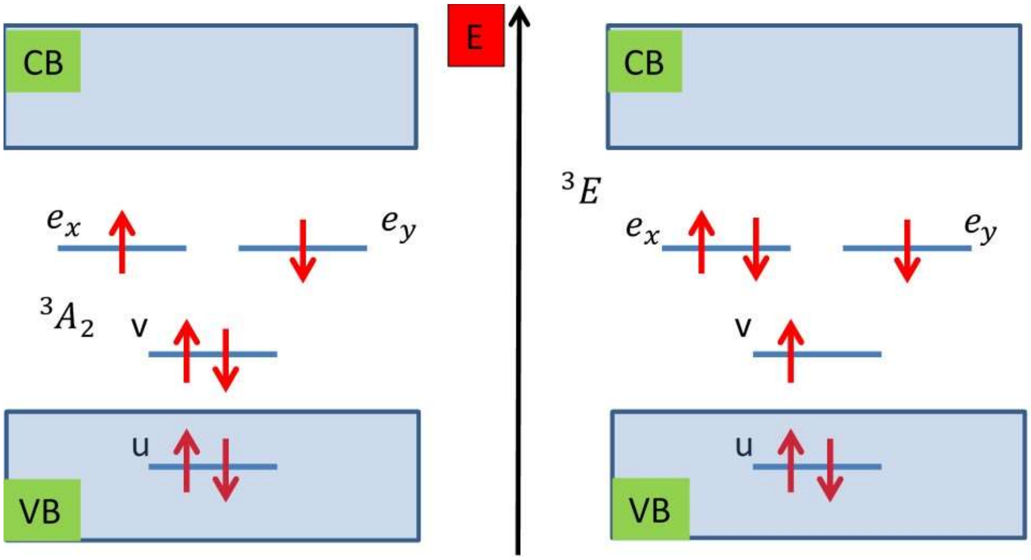

Figure 35. Schematic of the ground ($^3A_2$) and excited (^3E) state structure of the NV$^-$ relative to the valence band (VB) and conduction band (CB) in bulk diamond. The diagram was first proposed by[69]. The lowest energy MO, i.e. the one composed mostly of the N bond, lies within the VB of diamond, whereas the two higher energy orbitals lie within the band gap.

Figure 36(Error! Reference source not found.a) and b depict the basic energy level diagram for the NV center and the absorption and emission spectra respectively. The typical excitation wavelength used is 532nm and the zero phonon line (ZPL) is 1.94 e.v. (~ 637 nm). There also exists an intermediate singlet state with A_1 symmetry which gives rise to non-luminescent or "dark" transitions between the ^3E and the $^3A_2$ for the

$m_s = \pm1$. The dark state transition allows read-out of the ground state spin in electron spin resonance (ESR) measurements.

Spin-Orbit interaction splits the spin degeneracy (zero-field splitting) in the ground and excited states between the m_s=0 and $m_s = \pm1$ manifolds. The ground state zero-field splitting is 2.89 GHz and the excited state splitting is 1.42 GHz. Non-axial strain further splits the ground state $m_s = \pm1$ manifolds by 17 MHz.

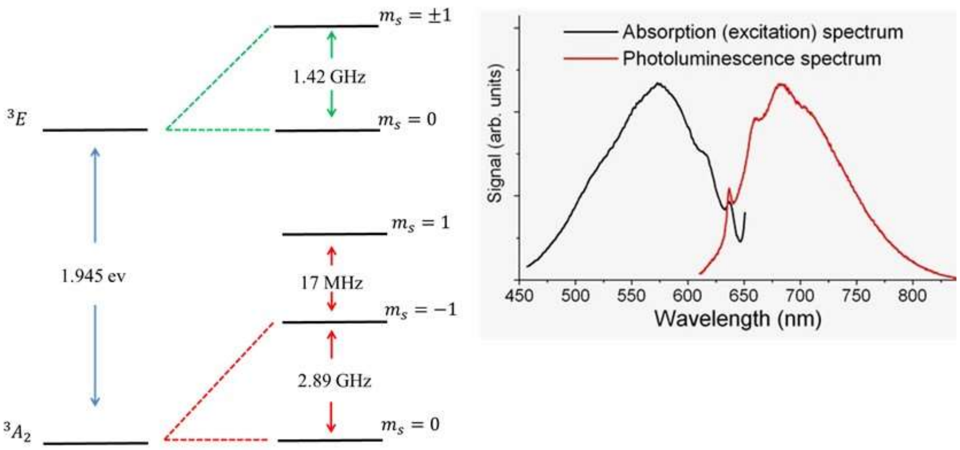

Figure 36. Basic energy level diagram for the NV$^-$ and the room temperature absorption and emission spectra. (a)The triplet ground and excited states are split by 1.945 e.v. with zero perturbation. Spin-orbit coupling lifts the degeneracy between the $m_s = 0$ and the $m_s = \pm1$ spin states, causing an energy difference of 2.89 GHz in the ground state and 1.42 GHz in the excited state. Non-axial strain further splits the $m_s = \pm1$ ground state spin manifold by 17 MHz. (b) The room temperature absorption and emission spectra.

Figure 37 depicts the typical dynamics of the NV center upon photon excitation. Typical confocal systems used to probe the NV use green light (532 nm) to cause the $A_2^3 \rightarrow E^3$ excitation (green arrow labeled as ω_p). There are two main channels for the NV to decay back into the ground state: spin-conserving stimulated emission (red dashed arrow labeled Γ), which will occur on the time scale of 13 ns with a ZPL of 1.945 e.v. (637 nm). The second decay channel is associated with the $m_s = \pm 1$ manifolds. The excited state $m_s = \pm 1$ manifold will also decay into a meta-stable A_1 singlet state with a life-time on the order of 300ns (green dashed arrow labeled Γ). The singlet state will then decay into the $m_s = 0$ ground state with 70% probability (purple dashed arrow labeled γ). The fluorescence associated with this process is not detected, thus allowing inference of the spin state of the NV from the fluorescence intensity. Accordingly the $m_s = 0$ ground state is known as the "bright state" and the $m_s = \pm 1$ ground states are known as the "dark states". This process also allows the NV^- to be polarized into the $m_s = 0$ state after a few optical cycles. The effect of an applied microwave field is depicted by the double headed red arrow, which gives rise to transitions between the spin manifolds in the ground state, i.e. Rabi oscillations.

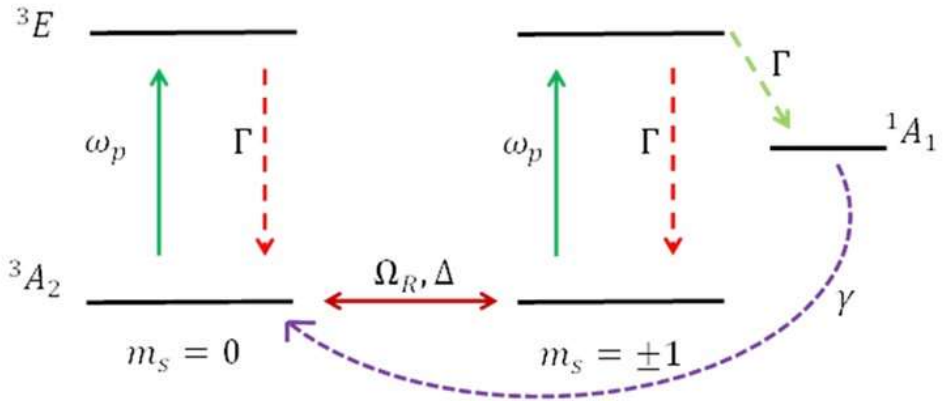

Figure 37. Energy level diagram of the electronic dynamics of the NV$^-$. Green light, ω_p, will cause a ground to excited state transition, $^3A_2 \rightarrow {}^3E$, for both spin manifolds. The lifetime of the $m_s = 0$ spin manifold in the excited state is 13 ns due to stimulated emission, and the decay will give off red light with a ZPL of 637 nm, denoted as Γ with the dashed red line. For the $m_s = \pm 1$ spin manifolds there are two types of decay processes: The first is due to spontaneoud emission with the same ZPL as for the $m_s = 0$ spin sub-level. The second decay process will cause a $m_s = \pm 1 \rightarrow 0$ transition and is associated with the decay into the metastable singlet-state $^1A_1$ (dashed green arrow). The lifetime for the $^3E \rightarrow {}^1A_1$ transition is 13 ns, and the lifetime for the $^1A_1 \rightarrow {}^3A_2$ tranition is 300 ns (γ and dashed purple line in the figure). Transitions between the $m_s = 0$ and the $m_s = \pm 1$ spin manifolds in the ground state are carried out by applying a microwave magnetic field (Ω_R and the double headed arrow).

APPENDIX 2

HPHT OF HYDROCARBONS IN RH EXPERIMENTS

The HPHT behavior of hydrocarbons has been studied previously both in a low pressure regime [56] (~5 GPa and ~200-600 ºC), and a high pressure regime [57] (>10 GPa and > 700 ºC). In both experiments the decomposition of the hydrocarbons was reported for pressures greater than ~1 GPa. For the lower pressure studies the final product was measured by XRD and found to consist of mostly amorphous carbon. Whereas the analysis of the high-pressure studies found the final product to be consistent with diamond as the ratio of hydrogen to carbon (H:C) increased above unity [6]. Notably in [57] the HPHT behavior was calculated to be diamond or amorphous carbon and H_2, and in [56] bubbles were optically observed exiting the SC when the DAC was opened to the atmosphere, similar to what was observed in RH7, and was concluded to be due to the H_2 leaking out of the SC.

The contention of the HPHT hydrocarbon experiments is that under HPHT hydrocarbons will decompose into C radicals and H_2 (the phase of which depends of the HPHT conditions). The melting of the hydrocarbons was only reported in [56] for pressures lower than considered here[7], and the temperatures for melting were fairly high (~ 300 ºC). Given that the melting temperature typically increases with pressure[58], and

---

[6] The best fit for diamond at high pressures was for polyethylene, polypropylene and poly(4-methyl-1-pentene). All pof which have a H:C = 2. Which is similar to the H:C = 8/5 for adamantane.

[7] For benzene the liquid phase was estimated to occur around 300 ºC and 2-3 GPa.

the relatively high melting temperatures reported in[56], it seems plausible that at the pressures investigated the melting temperature of adamantane is higher than the temperatures investigated for the RH experiments. Therefore, the behavior in the Raman spectra reported in RH1 and RH3 is most likely due to the partial decomposition of the adamantane into carbon radicals and H_2. Furthermore the bubbles and liquid substance optically observed in RH7 is considered to be liquid H_2.

Whereas in experiment RH6 the Raman spectra did blue shift which is indicative of volume expansion and could be associated with the melting of the sample, when considering the data and equations from [56] and [58] the ambient pressure melting temperature, T_m, of adamantane (270 ^{o}C) implies that in the 20 GPa range T_m should be higher than when the blue shifting began to occur.

The pressure behavior of RH1 around the blue-shifting region may be explained in terms of H_2 formation. The increase in temperature brings the adamantane molecules into closer vicinity until around 30 GPa and 600 ^{o}C the intra-molecular distance is short enough to allow the formation of H_2. The formation would increase the free volume in the crystal lattice allowing the Raman spectra to blue shift, and simultaneously increase the pressure due to the free hydrogen. However, the H_2 will eventually leak out of the SC either into the gasket, anvils or atmosphere allowing a decrease in the pressure, which is seen in the final HPHT Raman spectrum.